Effect of heat treatment on the migration behaviour of selenium implanted into polycrystalline SiC

by

Zaki Adam Yousif Abdalla

Submitted in partial fulfilment of the requirements for the degree of

DOCTOR OF PHILOSOPHY (PhD) IN PHYSICS

In the Faculty of Natural and Agricultural Sciences at University of Pretoria

December …… 2020

Supervisor/Promoter: Prof. T. T. Hlatshwayo

Co- supervisor: Prof. J. B. Malherbe

DECLARATION

I, Zaki Adam Yousif Abdalla, declare that the dissertation, which I hereby submit for the degree of PhD in University of Pretoria, is my own work and has not been submitted by for a degree at this or any other tertiary institution.

Signature: ……………………….

Date: …………………………….

SUMMARY

Effect of heat treatment on the migration behaviour of selenium implanted into polycrystalline SiC

by

Zaki Adam Yousif Abdalla

Submitted in partial fulfilment of the requirements for the degree of (PhD) in Physics in the Faculty of Natural and Agricultural Science, University of Pretoria

Supervisor/Promoter: Prof. T. T. Hlatshwayo

Co- supervisor: Prof. J. B. Malherbe

The success of a very high temperature gas cooled reactors (VHTGRs) like a pebble bed modular reactor (PBMR) depends greatly on the retainment of fission products. In PBMR the retainment is achieved by coating the fuel kernel with layers of chemical vapour deposited carbon and silicon carbide (SiC). Of these coating layers, SiC is the main barrier of fission products. Hence, the migration behaviour of radioactive fission products in SiC is vital. The migration behaviour of fission products such as strontium, iodine, cesium and silver in SiC at temperatures above 1000 ºC have been studied extensively. There is no reported information on the migration behaviour of selenium in SiC, which needs to be studied due to the risks posed by its emission and presence in the environment.
In this study, Se ions of 200 keV were implanted into polycrystalline SiC wafers to a fluence of 1×10^{16} cm^{-2} at room temperature (RT), 350 ºC and 600 ºC. RT implanted samples were sequential annealed at temperatures ranging from 1000 to 1500 ºC in steps of 100 ºC for 10 h and at 1300 ºC, 1350 ºC and 1450 ºC for 20 h while the hot implanted samples were only sequential annealed at temperatures ranging from 1000 to 1500 ºC in steps of 100 ºC for 10 h. Another set of implanted samples were isothermal annealed at 1300 ºC, 1350 ºC and 1400 ºC for 10 h cycles of up to 80 h. The migration of implanted Se was monitored by Rutherford

backscattering spectrometry (RBS) while structural and morphological changes were monitored by Raman spectroscopy and scanning electron microscopy (SEM).

Implantation of Se at room temperature amorphized the near-surface region of the SiC substrate while implantation at 350 ºC and at 600 ºC retained the crystallinity with defects. More defects were observed in the 350 ºC implanted samples compared to 600 °C.

Annealing the RT implanted samples at 1000 ºC resulted in the recrystallization of the amorphous SiC. No diffusion was observed for annealing up to 1200 ºC. Slight peak broadening indicating diffusion was observed after annealing at 1300 ºC. This broadening increased with increase in annealing temperature. Annealing at temperatures above 1200 ºC resulted in the Se profile shifting towards the surface resulting in the loss of about 10 %, 20 % and 40 % of Se at 1300 ºC, 1400 °C and 1500 ºC, respectively. The diffusion coefficients at 1300 and 1350 °C were estimated to be 6.3×10^{-21} and 2.0×10^{-20} m^2 s^{-1}, respectively. Isothermal annealing the RT implanted samples at 1300 ºC, 1350 ºC and 1400 ºC for 10 h cycles of up to 80 h caused the broadening of selenium profile during the first and second annealing cycle and no further a broadening was observed in subsequent annealing cycles up to 80 h. These indicated the migration of Se in damaged SiC region. The diffusion coefficients at 1300 ºC, 1350 ºC and 1400 ºC were estimated to be 1.4×10^{-20} m^2s^{-1}, 2×10^{-20} m^2s^{-1} and 2.5×10^{-20} m^2s^{-1}, respectively which yielded to an activation and pre-exponential factor were found to be 2×10^{-22} J and 1.7×10^{-16} m^2s^{-1}, respectively.

Both sequential annealing and isothermal annealing of hot (350 ºC and 600 ºC) resulted in no measurable diffusion of implanted Se further pointing to radiation enhanced migration of Se as suggested by RT implanted results.

Acknowledgements

I would like to acknowledge the following people, without whom I would not have been able to complete this work.

- My academic promoter, Prof. T. T. Hlatshwayo, my co-promoter Prof. J. B. Malherbe. Without their active guidance, help, cooperation and encouragements for all time, I would not have made headway in the project.
- The heard of department, Prof. C.C Theron for arranging some part-time work in the department, which helped me financially during this study.
- Dr. E. G Njoroge and Dr. M Mlambo for providing guidance and feedback throughout this project.
- Mrs. Elfrieda Meyburgh for all her assistance in the physics department.
- My friends in the nuclear material and ion- solid interactions research group, for all their help, encouragement and moral support.
- My parents (Adam and Aisha), my brothers and sisters for their trust in me, support and encouragement.
- The National Research Foundation (NRF) and The World Academy of Sciences (TWAS), for providing me with a bursary that enabled my studies.
- I thank Allah who made all these possible.

LIST OF ABBREVIATIONS

BSE – Backscattered electrons

CCD – Charged coupled devices

FE-SEM- Field emission scanning electron microscope

FPs – Fission products

FWHM – Full width at half maximum

MCA – multi-channel analyser

PBMR – Pebble bed modular reactor

RBS – Rutherford backscattering spectrometry

SE – Secondary electrons

SEM – Scanning electron microscopy

SRIM – Stopping and range of ions in matter

TRIM – Transport of ions in matter

TRISO particles – Tristructural-isotropic

VHTR – Very-high-temperature reactor

TABLE OF CONTENTS

SUMMARY ii

CHAPTER 1 1

INTRODUCTION 1

1.1 Very High Temperature Gas-cooled Reactor (HTGR) 1

1.2 Crystal Structure of Silicon Carbide 3

1.3 Properties of Silicon Carbide 5

1.4 Radiation damage in SiC 6

1.5 Diffusion behaviour of fission products in silicon carbide 7

1.6 Research aims and objectives 8

1.7 The outlay of the thesis 8

References 9

CHAPTER 2 13

DIFFUSION 13

2.1 Steady State and Time Dependent Diffusion 13

2.1.1 Steady state diffusion 13

2.1.2 Time dependent diffusion 15

2.2 Arrhenius' law 16

2.3 Defects 17

2.3.1 Point defects 17

2.3.2 Line defects 18

2.3.3 Planar defects 19

2.4 Diffusion mechanisms 20

References 22

CHAPTER 3 24

ION IMPLANTATION 24

3.1 The Stopping Power and Range 24

3.1.1 Nuclear Stopping 27

3.1.2 Electronic Stopping 29

3.1.3 Energy Loss in Compounds 31

3.1.4 Energy Straggling 31

3.2 Mathematical model of ion implantation 32

3.3 Simulation of ion implantation 33

3.4 Radiation damage formation and annealing in SiC 35

References 36

CHAPTER 4 38
ANALYTICAL TECHNIQUES 38
4.1 Rutherford Backscattering Spectrometry 38
4.1.1 Rutherford Backscattering Spectrometry Components 38
4.1.2 The Detector and Data Acquisition Systems 41
4.1.3 RBS as Materials Analysis Method and its Basic Physical Concepts 43
4.1.3.1 Kinematic Factor (K) 43
4.1.4 Depth Profiling 45
4.1.5 Differential Cross section 47
4.2 Raman Spectroscopy 47
4.2.1 The main components of the Raman spectrometer 48
4.2.2 Fundamental Principles of Raman Spectroscopy 49
4.2.3 Theory of Raman Scattering 50
4.3 Scanning Electron Microscopy 51
4.3.1 Main Components and Operational Systems of SEM 51
4.3.2 Electron-Specimen Interactions 53
References 57
CHAPTER 5 59
EXPERIMENTAL PROCEDURES 59
5.1 Sample preparation 59
5.2 Implantation procedures 60
5.3 Annealing process 60
5.4 The basic conditions of measurement 62
5.4.1 Raman measurement 62
5.4.2 SEM measurement 63
5.4.3 RBS measurements 63
References 64
CHAPTER 6 65
RESULTS AND DUSCUSSION 65
6.1 Room temperature implantation 65
6.1.1 Raman Results 65
6.1.2 SEM Results 70
6.1.3 RBS Results 75
6.2 Hot implantation 85
6.2.1 Raman Results 85
6.2.2 SEM Results 92

6.2.3 RBS Results 98
References 107
CHAPTER 7 110
CONCLUSIONS AND FUTURE STUDIES 110
7.1 Room temperature implantation 110
7.1 Hot implantation 112
7.1 Future studies 113
CHAPTER 8 114
APPENDIX 114
8.1 Publications in peer-reviewed/refereed journals 114
8.2 Conference Presentations 114
8.2.1 National Conferences 114
8.2.2 International Conferences 115

LIST OF FIGURES

Fig. 1.1: Primary energy consumption by energy source, 2019. Note: Sum of components may not equal 100% due to independent rounding. Raw data taken from [www1]. 2
Fig. 1.2: Graphical representation of the pebble bed TRISO fuel sphere cross section. Taken from [Wel01]. 3
Fig. 1.3: Some of the main polytypes stacking sequence of SiC. 4
Fig. 1.4: Schematic diagram showing SiC crystals: tetrahedron consisting of (a) one C and four Si and (b) one Si and four C atoms; the bond distance a = 0.308 nm, d = 0.189 nm. θ =190º. Taken from [Riu18]. 5
Fig. 2.1: A schematic change in concentration as a function of distance in a one-dimensional space. 14
Fig. 2.2: A schematic change in flux in and out a volume element with a uniform cross-sectional area. 15
Fig. 2.3: Arrhenius plot of the linear relationship between ln D and 1/T. 17
Fig. 2.4: Schematic diagram of a crystalline structure:(a) perfect crystal (b) crystal with the three basic types of point defects. 18
Fig. 2.5: Schematic diagram of line defects: (a) edge dislocation and (b) screw dislocation in an atomic lattice. 19
Fig. 2.6: Schematic illustration of grain boundaries. 20
Fig. 2.7: An illustration of diffusion mechanisms and point defects: (a) Vacancy, (b) Interstitial and (c) interstitialcy diffusion. 21
Fig. 3.1: The nuclear and electronic stopping power as a function of energy of implanted ion. 25
Fig. 3.2: Ion beam and cross section of one microscopic target. 26
Fig. 3.3: A schematic diagram showing a scattering of an energetic ion by a target 28
Fig. 3.4: The schematic diagram of implanted ions (a) the parameters of normal distribution, (b) the projected range and total path length. 33
Fig. 3.5: A TRIM simulation of 200 keV Se ions implanted into SiC showing distribution of (a) ion range (b) vacancies (c) ionization. 34
Fig. 4.1: Schematic diagram of a Van der Graaff accelerator (a) and a radio-frequency ion source ion source (b). Taken from [Chu78] 39
Fig. 4.2: Schematic diagram showing of RBS set-up at the University of Pretoria 40
Fig. 4.3: Schematic diagram showing the scattering chamber and its components. 41
Fig. 4.4: Schematic diagram of a gold-surface barrier nuclear particle detector. Taken from [Got64]. 42
Fig. 4.5: Schematic view of a the detector and data acquisition systems 42
Fig. 4.6: Schematic diagram showing the scattering process between energetic ion and target atom. Taken from [Alf07]. 44
Fig. 4.7: A schematic diagram representing the backscattering events and energy loss at a depth x from the target surface. Redrawn from [Chu78]. 46
Fig. 4.8: A schematic diagram representing the components of Raman spectroscopy. Redrawn from [Aga95] 48
Fig. 4.9: Schematic diagram showing the Rayleigh scatter, Stokes Raman scatter and Anti- 49
Fig. 4.10: A schematic representation of the main components of a typical SEM. Taken from 53
Fig. 4.11: A schematic diagram showing the signals which are emitted when an electron beam 54
Fig. 4.12: A schematic diagram showing that the signals generated by the electron beam- 55

Fig. 5.1: Schematic diagram describing the experimental procedures. 59

Fig. 5.2: Computer-controlled Webb 77 graphite furnace used in this research. Taken from 62

*Fig. 5.3: Diagram showing the annealing process for a sample annealed at 1000 °*C *for 10 hours.* 62

Fig. 6.1: Raman spectra of the pristine -SiC after implantation and sequential annealing from 1000 to 1500 °C for 10 h. 66

Fig. 6.2: The FWHM and Raman shift of the LO mode as function of temperature (a) after sequential annealing from 1000 to 1500 °C for 10 h, (b) after annealing at 1300 °C, 1350 °C and 1450 °C for 20 h. 67

Fig. 6.3: LO modes of SiC Raman spectra of samples implanted with Se at room temperature as a function of time during isothermal annealing at temperatures of (a) 1300 °C, (b) 1350 °C and (c) 1400 °C. 68

Fig. 6.4: The intensity of LO mode of SiC implanted with Se at room temperature as a function of time during isothermal annealing at different temperatures. 69

Fig. 6.5: The FWHM of LO mode of SiC implanted with Se at room temperature as a function of time during isothermal annealing at different temperatures. 69

Fig. 6.6: The Raman shift of LO mode of SiC implanted with Se at room temperature as a function of time during isothermal annealing at different temperatures. 70

Fig. 6.7: Surface SEM micrographs of (a) Pristine poly-SiC; (b) after implantation with Se at RT; compared with surfaces after vacuum annealing at (c)1000 °C, (d) 1300 °C, (e) 1400 °C and (f) 1500°C for 10 h. 72

Fig. 6.8: Surface SEM micrographs of as-implanted SiC after vacuum annealing at (a) 1300 °C, (b) 1350 °C and (c) 1450 °C for 20 h. 73

Fig. 6.9: SEM micrographs of room temperature selenium implanted SiC surfaces after vacuum annealing at 1300 °C for (a) 10 h and (b) 80 h. 74

Fig. 6.10: SEM micrographs of room temperature selenium implanted SiC surfaces after vacuum annealing at 1350 °C for (a) 10 h and (b) 80 h. 74

Fig. 6.11: SEM micrographs of room temperature selenium implanted SiC surfaces after vacuum annealing at 1400 °C for (a) 10 h and (b) 80 h. 75

Fig. 6.12: The depth profile of Se implanted into SiC from RBS, SRIM 2012 simulated Se depth profile and damage in displacement per atom (dpa). 77

Fig. 6.13: Depth profiles of selenium implanted in SiC at room temperature and after sequential annealing from 1000 to 1500 °C for 10 h. 78

Fig. 6.14: The full width at half maximum, the peak position of implanted Se, and retained ratio (calculated as the ratio of the total integrated counts of Se after annealing to that of as-implanted) of the Se profile as a function of annealing temperature. 79

Fig. 6.15: RBS spectra of selenium implanted in SiC at room temperature and after sequential annealing from 1000 to 1500 °C for 10 h. Arrows indicate the surface positions of elements. 79

Fig. 6.16: Depth profiles of selenium implanted in SiC at room temperature and after sequential annealing at1300, 1350 and 1450 °C for 20 h. 80

Fig. 6.17: The full width at half maximum, the peak position of implanted Se, and retained ratio (calculated as the ratio of the total integrated counts of Se after annealing to that of as-implanted) of the Se profile as a function of annealing temperature 80

Fig. 6.18: Example of the fitting of the diffusion equation solution to the depth profiles of the sample (a) as-implanted, (b) annealed at 1300 ^{o}C for 10 h. 81
Fig. 6.19: Isothermal annealing curves of room temperature implanted samples at 1300 °C, 1350 °C and 1400 °C. 82
Fig. 6.20: The retained ratio of Se implanted into polycrystalline SiC at room temperature after isothermal annealing. 83
Fig. 6.21: The plot of $\ln D$ *versus 1/T for annealing temperatures of 1300, 1350 and 1400 °C for Se implanted into polycrystalline SiC at RT.* 84
Fig. 6.22: The Raman spectra of the pristine poly-SiC and SiC implanted with Se at RT, 350 °C and 600 °C. 85
Fig. 6.23: Comparative Raman spectra from selenium implanted into poly-SiC at (a) 350 °C and (b) 600 after sequential annealing at 1000 and 1500 °C for 10 h. 86
Fig. 6.24: The residual stress in the poly-SiC samples implanted with Se at 350 °C and 600 °C as a function of annealing temperature. 87
Fig. 6.25: LO modes of SiC Raman spectra of samples implanted with Se at 350 °C as a function of time during isothermal annealing at temperatures of (a) 1300 °C, (b) 1350 °C and (c) 1400 °C. 88
Fig. 6.26: LO modes of SiC Raman spectra of samples implanted with Se at 600 °C as a function of time during isothermal annealing at temperatures of (a) 1300 °C, (b) 1350 °C and (c) 1400 °C. 89
Fig. 6.27: The intensity of LO mode of SiC implanted with Se at (a) 350 °C and (b) 600 °C as a function of time during isothermal annealing at different temperatures. 90
Fig. 6.28: The FWHM of LO mode of SiC implanted with Se at (a) 350 °C and (b) 600 °C as a function of time during isothermal annealing at different temperatures. 90
Fig. 6.29: The Raman shift of LO mode of SiC implanted with Se at (a) 350 °C and (b) 600 °C as a function of time during isothermal annealing at different temperatures. 91
Fig. 6.30: SEM micrographs of poly-SiC after implantation with Se at (a) 350 °C and (b) 600 °C; compared with surfaces after vacuum annealing at 1000 °C for samples implanted at (c) 350 °C and (d) 600°C for 10 h. 92
Fig. 6.31: SEM micrographs after vacuum annealing at 1100 °C for samples implanted at (a) 350 °C and (b) 600°C for 10 h. 93
Fig. 6.32: SEM micrographs of the 350 °C implanted sample after vacuum annealing at (a) 1300 °C, (b) 1400 °C, the 600 °C implanted sample after vacuum annealing at (c) 1300 °C and (d) 1400 °C for 10 h. 94
Fig. 6.33: SEM micrographs of the 350 °C implanted samples in the first annealing cycle (10 h) at (a) 1300 °C, (b) 1350 °C and (c) 1400 °C. 95
Fig. 6.34: SEM micrographs of the 600 °C implanted samples in the first annealing cycle (10 h) at (a) 1300 °C, (b) 1350 °C and (c) 1400 °C. 96
Fig. 6.35: SEM micrographs of the 350 °C implanted samples after annealing at (a) 1300 °C, (b) 1350 °C and (c) 1400 °C for 40 h. 97
Fig. 6.36: SEM micrographs s of the 600 °C implanted samples after in annealing at (a) 1300 °C, (b) 1350 °C and (c) 1400 °C for 40 h. 98
Fig. 6.37: The depth profiles of 200 keV Se implanted into SiC at room temperature, 350 °C and 600 °C from RBS, compared to SRIM 2012 simulated Se depth profile. 99

Fig. 6.38: Depth profiles of selenium implanted in SiC at (a) 350 °C and (b) 600 °C after sequential annealing from 1000 to 1500 °C for 10 h. 100

Fig. 6.39: The peak position of implanted Se profile as a function of annealing temperature. 101

Fig. 6.40: The retained ratio of Se implanted into polycrystalline SiC profiles as a function of annealing temperature. 102

Fig. 6.41: The square of the full width at half maximum of implanted Se profiles as a function of annealing temperature. 103

Fig. 6.42: Isothermal annealing curves of (a) 350 °C and (b) 600 °C implanted samples at 1300 °C, 1350 °C and 1400 °C. 104

Fig. 6.43: The retained ratio of Se implanted into polycrystalline SiC at (b) 350 °C and (b) 600 °C after isothermal annealing. 105

LIST OF TABLES

Table 6.1: A comparison of the first four moments of the experimental and SRIM simulated profiles. The selenium experimental profiles of RT, 350 °C and 600 °C were fitted to the Edgeworth function....99

CHAPTER 1

INTRODUCTION

One of the challenges arising from increased energy demand is reducing carbon dioxide emissions. These emissions are the result of high energy consumption of a strong global economy, as well as due to changes in weather conditions in some parts of the world, which have led to an increase in energy demand for heating and cooling.

Population growth and industrialization also require more electricity production, subsequently causing even greater environmental problems by increasing carbon emissions. Currently, almost 80% of the world's energy consumption is provided by fossil fuel as shown in Fig.1.1 [www1]. The Kyoto Protocol is an international treaty, named for the Japanese city that was adopted in December 1997. The aim of this protocol was to manage and reduce emissions of carbon dioxide and greenhouse gases [www2]. The essential tenet of the treaty is that industrialized countries needed to lessen the amount of their CO_2 emissions [www2].

The lack of fossil fuel supplies, as well as the environmental problems associated with burning coal, under the Kyoto protocol, are a direct motivation for the development of alternative energy sources. This certainly requires a major shift in production, delivery and energy consumption techniques/strategies. Nuclear power reactors are part of the energy solution as they are reliable clean energy producers. However, there is a negative general perception that must be considered. This negativity is based on the possible leakage of radioactive fission products into the environment during conditions of normal operation or accident such as those that occurred at Chernobyl and Fukushima. Moreover, the leakage of high level radioactive from waste storages into the environment due to long term storage raise some doubts on their safety.

1.1 Very High Temperature Gas-cooled Reactor (HTGR)

A very-high-temperature reactor (VHTR), is a Generation IV reactor that uses natural or slightly enriched uranium as a fuel, graphite as a moderator (to slow the neutrons to enhance fission) and gases such as helium and carbon dioxide for cooling [Pio19]. Goals of the Generation IV systems, are: (1) sustainability, (2) economics, (3) safety and reliability, and (4) proliferation resistance and physical protection [Pio19]. A typical VHTR is a pebble bed

modular reactor (PBMR). In PBMR, safety is improved by coating the fuel with layers in the form of tristructural isotropic (TRISO)-coated particle [www3] [Mal08]. The success of the PBMR is highly dependent on the performance of the TRISO particles and the quality of its components [Ske16]. The function of these layers is to retain the radioactive fission products within the fuel particles under normal operation and even under accident conditions [Mal13] [Van10].

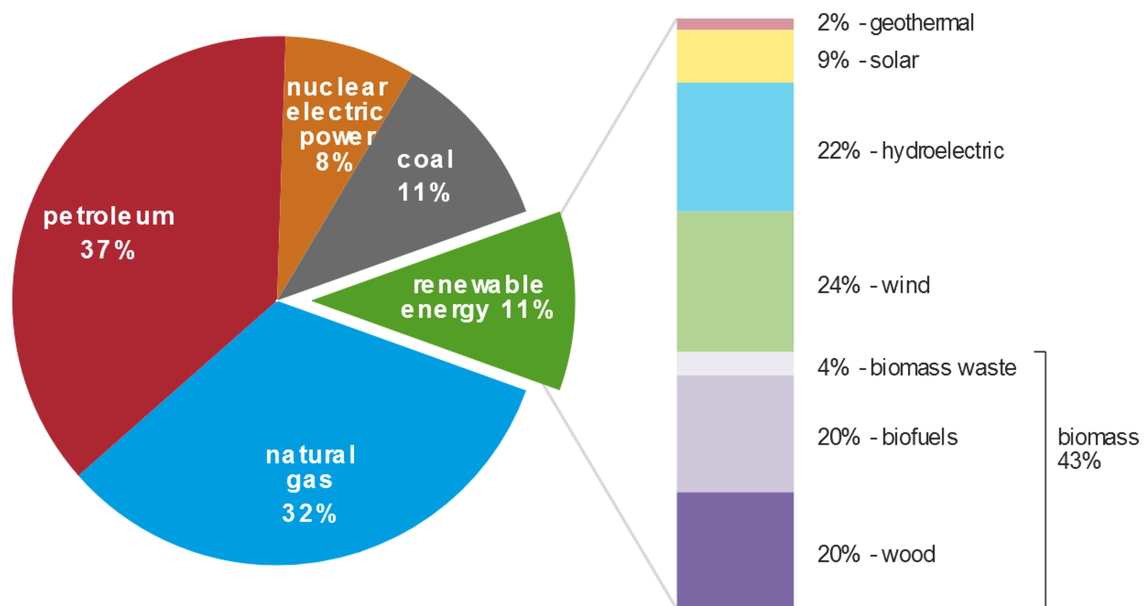

Fig. 1.1: Primary energy consumption by energy source, 2019. Note: Sum of components may not equal 100% due to independent rounding. Raw data taken from [www1].

The fuel kernel, which contains the nuclear fuel (UO_2) in a TRISO particle, is coated with a porous carbon buffer layer. This is then followed by three layers of isotropic coating materials: (1) an inner pyrolytic carbon (IPyC) layer, (2) a silicon carbide (SiC) layer, and (3) an outer pyrolytic carbon (OPyC) layer as shown in Fig.1.2 [Gül08] [Ske16]. Each of these layers has a specific function. Porous carbon/ buffer layer is to provide the necessary protection for the inner pyrolytic carbon layer from damage caused by the recoil of fission fragments. The inner pyrolytic carbon layer is a high-density carbon layer. It protects the kernel from the reactive chlorine produced during the SiC coating process [Gül08]. Based on the outstanding properties of silicon carbide as reported in ref [Sne07], the SiC layer is considered to be the most important structure in the TRISO fuel particles [Hos13]. It must also be able to withstand high temperatures. The outlet temperature of some of the VHTGRs is about 900 °C [Mal08].

Moreover, the temperature inside the TRISO fuel particles is higher than the outlet temperature [Mal13]. The silicon carbide has the ability to maintain most of its properties at high temperature and thermally in a vacuum at about 1700 °C [Mal13] [Van12]. So, its function is not only a diffusion barrier for fission products, but also provides mechanical support and protects the coated particle. This requires a good bonding between the SiC layers and the pyrolytic carbon layers as indicated previously. Finally, the outer pyrolytic carbon (OPyC) layer isolates the SiC layer from the matrix that binds the TRISO particles together and also provides a compressive force on the SiC. In general, the SiC coating layer of TRISO particles is a structural element that ensures the fission products are contained, and thus forms the safety rationale for the nuclear reactor.

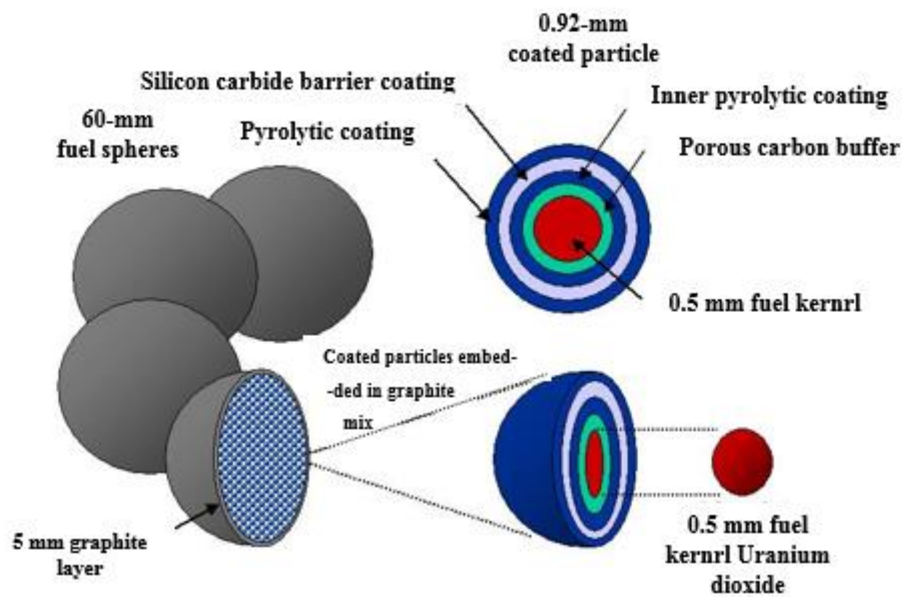

Fig. 1.2: Graphical representation of the pebble bed TRISO fuel sphere cross section. Taken from [Wel01].

1.2 Crystal Structure of Silicon Carbide

To date, more than 200 varieties of silicon carbide have been found. Common types are 3C, 2H, 4H and 6H. In these types, silicon carbide crystallizes in the zinc-blende (3C) structure and wurtzite structure (2H, 4H and 6H) as depicted in Fig. 1.3. The numbers (3, 2, 4, and 6) indicate the number of layers required for periodicity. While, the letters C and H refer to the cubic and hexagonal symmetry, respectively. The basic structural unit of SiC polytypes is the

covalently-bonded tetrahedron. Its either Si bonded with four carbons or C bonded with four Si [Sne07] see Fig. 1.4. For all polytypes, the chemical bond between Si and C atoms consists of the sp^3 hybrid orbital with a bond distance of 0.189 nm [Mut03]. Whereas the distance between (two similar atoms) neighbouring Si or C atoms is 0.308 nm [Riu18], see Fig.1.4. The Si-C tetrahedral basic unit is periodically repeated in hexagonal bilayers, with C and Si single bonds pointing up and down, in a perpendicular direction relative to the basal plane. The stacking sequence of the various polytypes can be described in terms of the A, B and C notations. 3C-SiC, (also called β-SiC) is the only cubic polytope and has ABC stacking sequence. While the 2H, 4H, and 6H-SiC polytypes have hexagonal bonds with an AB, ABCB, and ABCACB stacking sequence, respectively as depicted in Fig. 1.3. SiC polytype structure has a (111) stacking direction, where one bond from a tetrahedrally-bonded Si atom is directed along the c-axis (<111>), and is called the Si face. Whereas the $(\bar{1}\bar{1}\bar{1})$, where one bond from a tetrahedrally-bonded C atom is directed along the c-axis (<111>), and is called the C face [Kim14] [Cho13]. The other polytypes have only one stacking direction (0001), where one bond from a tetrahedrally-bonded Si atom is directed along the c-axis (<0001>), and is called the Si face. Whereas the (0001), where one bond from a tetrahedrally-bonded C atom is directed along the c-axis ($<000\bar{1}>$), and is called the C face [Kim14] [Cho13].

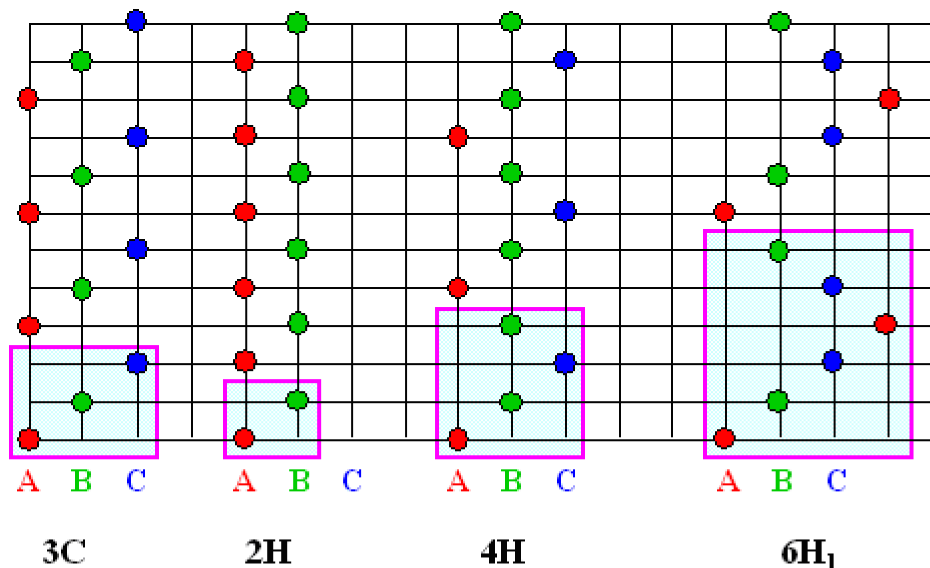

Fig. 1.3: Some of the main polytypes stacking sequence of SiC.

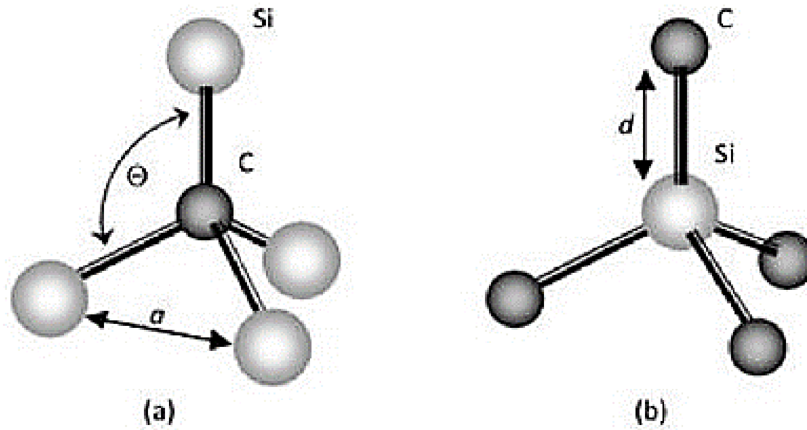

Fig. 1.4: Schematic diagram showing SiC crystals: tetrahedron consisting of (a) one C and four Si and (b) one Si and four C atoms; the bond distance a = 0.308 nm, d = 0.189 nm. θ =190°. Taken from [Riu18].

1.3 Properties of Silicon Carbide

Silicon carbide is a good material for high-heat-flux applications due to its excellent properties, such as high hardness and mechanical stability at high temperatures, high thermal conductivity, low thermal expansion, high resistant to radiation damage, corrosion and oxidation [Bor17] [Yvo16]. The high resistance to irradiation makes the SiC a first-choice for various nuclear applications, such as a structural material in high-temperature nuclear reactors. In addition to this extraordinary mechanical property, SiC also decomposes in vacuum at about 1700 °C [Van12]. This gives it the ability to retain most of these properties at high temperatures. The hardness comes from its high bond strength due to the short bond length between Si and C which is 0.189 nm [Van12] [Riu18]. The high resistance to corrosion and chemical attack is due to its strong chemical bond energy resulting from the high cohesive energy, i.e. the cohesive energy per atom of SiC is 6.34 eV [Mal13] [Fan16]. The peak in the thermal conductivity of silicon carbide is about 100 K, which is relatively higher than for most other materials [Zha17]. Because of both silicon and carbon have low neutron cross section, in addition to the attractive properties of SiC at high-temperatures, above mentioned, it is proposed as a candidate structural material for in future nuclear power reactors [Mal13].

1.4 Radiation damage in SiC

Radiation damage in SiC has been investigated by many researchers over the last few decades. Zinkle *et al*. [Zin96], have reported that SiC easily amorphized after damage levels of 0.4 dpa at room temperature. The amorphization behaviour of ß-SiC and α-SiC specimens was found to be similar [Zin96]. McHargue *et al*. [McH93], demonstrated that amorphization of silicon can readily be obtained by ion implantation of low energy ions of a few hundred keV at room temperature regardless of the ions implanted. This amorphization is temperature-sensitive and tends to become much harder at higher temperatures [Pag16]. A comprehensive study of the amorphization of silicon carbide using Al and Si ions was performed by Slotte *et al* [Slo05]. The effects of ion fluence, ion flux, and implantation temperature on the projected ion range region, and thus on defect production were demonstrated. Grimaldi *et al*. [Gri97] studied the effect of the ion mass and substrate temperature on the damaging process. This was a study based on the damage produced by ion implantation in SiC. The investigation included in a more comprehensive study of the damage produced by ion implantation in SiC, focusing on the effect of the ion masses in the range of 4 to 131 amu, and the substrate temperature of 77 and 300 K. The evaluations showed that damage accumulation was approximately linear with fluence until amorphization occurs when the elastic energy density deposited by the ions overcomes a critical value.

The effect of swift heavy irradiation (SHI) and heat treatment on recovering of structural damage caused by ion implantation in SiC were investigated by Hlatshwayo *et al*. [Hla16]. They found that individual implantations of 360 keV to a fluence of 1×10^{16} cm^{-2} and of Kr to a fluence of 2×10^{16} cm^{-2} in polycrystalline SiC at room temperature resulted in fully amorphised SiC from the surface up to a depth of 196 and 230 nm, respectively. Both annealing at 500 °C and SHI irradiation with 167 MeV Xe to a fluence of 5×10^{13} cm^{-2} at 500 °C of the implanted samples resulted in the shrinking of the amorphous layer. A. Audren *et al*. [Aud07] implanted 300 keV Cs ions at RT with different fluences (from 2 x 10^{13} cm^{-2} to 6×10^{14} cm^{-2}) into SiC. The authors found that the atomic disorder created in the crystal structure increases significantly with the ion fluence. Rutherford Backscattering combined with channelling (RBC/C) used in the study showed that the damage peak reached the random level at a fluence of about 10^{14} cm^{-2}, indicating the presence of a buried amorphous layer. At a fluence of 6×10^{14} cm^{-2}, the amorphous layer extended to a depth of about 150 nm below the surface. The RBS/C also showed that the annealing of damage began at around 600 ºC, starting from the interface between the damaged region and the crystalline bulk. Some appreciable crystallization up to

the surface was only observed at temperatures above or equal to 960 ^{o}C. Further annealing led to more recrystallization and the structure became nearly half disordered at 1300 ^{o}C.
McHargue *et al*. [McH93] extensively studied ion implantation effects in α and ß Silicon carbide by Rutherford backscattering spectrometry/channelling. They reported that the amorphization takes place for damage energies of about 20 eV/atom, which corresponds to 0.2 to 0.3 displacements per atom, at room temperature (dpa). However, implantation does not result in an amorphous region for damage levels of up to 17 dpa, at higher temperatures equal to or greater than 500 °C. The study also showed that when the damage level in the surface region is less than that necessary to produce amorphization, the annealing of damage requires in one stage a low-temperature range of 200°C to 1000°C. While, the annealing behaviour of amorphous layer caused by high damage is less clear, and regrowth occurs at temperatures ranging from 750 to 1700 °C.

1.5 Diffusion behaviour of fission products in silicon carbide

In recent years, the diffusion of fission products in different polytypes of SiC has been extensively studied using ion implantation. In this process, ions are accelerated and made to penetrate a solid target, which leads to a change in the surface physical and chemical properties of the material. A great number of research studies were performed by our group at the University of Pretoria. These studies resulted in numerous publications that have reviewed the diffusion of important fission products in SiC such as silver, cesium, xenon, krypton, iodine, and strontium [Mal13] [Fri12] [Fri14] [Fri12] [Fri13] [Hla15]. No work has been done on the migration behaviour of selenium in SiC.
Se is a non-metallic element that has many radioactive and stable isotopes. Se radioactive isotope, ^{79}Se, is present in the nuclear fission products of uranium [Pet07]. ^{80}Se is one of the stable isotopes, the most prevalent, comprising about half of natural selenium [Pet07]. It is both naturally occurring and produced by fission [www4]. Moreover, Se is found in high-level radioactive wastes resulting from processing spent fuel associated with the operation of nuclear reactors and fuel reprocessing plants [Pet07]. Although the low percentage yield of selenium formed by uranium fission in a nuclear reactor, the risk comes from leaking this amount into the environment for a long term [Abd20]. The radiological hazard of selenium comes from the emitted beta particle during its radioactive decay, which is associated with an increased likelihood of cancer [Pet07]. The aim of this study is to investigate the effect of heat treatment at temperatures ≥1000 °C on the migration behaviour of Selenium (Se) implanted into

polycrystalline SiC to a fluence of 1×10^{16} cm^{-2} at room temperature, 350 °C and 600 °C. All important aspects will be discussed in greater detail later in chapter 6.

1.6 Research aims and objectives

In this thesis, the migration behaviour of Se in polycrystalline SiC (SiC) was investigated. After implantation, different heat treatments were performed on the samples, as discussed in more detail in Chapter 5. Then, several techniques were used to characterize samples before and after heat treatment. Rutherford backscattering spectrometry (RBS) was used to monitor the Se in the SiC before and after heat treatment. Scanning electron microscopy (SEM) was used to monitor the morphological evolution of the surfaces. While Raman spectroscopy was used to identify chemical/structural changes.

1.7 The outlay of the thesis

This thesis is structured as follows. Chapter 1 gives a general introduction to the very-high-temperature reactor, crystal structure of silicon carbide and its properties, radiation damage in SiC as well as migration behaviour of fission products in silicon carbide. Chapter 2 discusses the diffusion mechanisms and the mathematical theory of diffusion. Chapters 3 discusses the basic principles of the ion implantation in solids. In Chapter 4, the analytical techniques used in this thesis will be discussed. Chapter 5 provides a brief overview of some of the experimental procedures and annealing processes. The results of this study are presented and discussed in Chapter 6. Chapter 7 contains a summary of the research, conclusions. The closing chapter, Chapter 8 presents the research outputs from this work.

References

[Abd20] Z.A.Y. Abdalla, M.Y.A. Ismail, E.G. Njoroge, T.T. Hlatshwayo, E. Wendler, J.B. Malherbe, Migration behaviour of selenium implanted into polycrystalline SiC, Vacuum **175** (2020) 109235.

[Aud07] A. Audren, A. Benyagoub, L. Thomé, and F. Garrido. "Ion implantation of Cs into silicon carbide: Damage production and diffusion behaviour." Nuclear Instruments and Methods in Physics Research Section B: Beam Interactions with Materials and Atoms **257** (2007) 227-230.

[Bor17] I. P. Borovinskaya, A. A. Gromov, E. A. Levashov, Y. M. Maksimov, A. S. Mukasyan, and A. S. Rogachev, Concise encyclopedia of self-propagating high-temperature synthesis: History, theory, technology, and products. Elsevier, Amsterdam, Netherlands, (2017).

[Cho13] W. J. Choyke, H. Matsunami, and G. Pensl, Silicon carbide: recent major advances. Springer Science & Business Media, USA, (2013).

[Fan16] Q. Fan, C. Chai, Q. Wei, and Y. Yang. The mechanical and electronic properties of carbon-rich silicon carbide, Materials 9, **5** (2016) 333.

[Fri12] E. Friedland, N. G. van der Berg, J. B. Malherbe, E. Wendler, and W. Wesch. Influence of radiation damage on strontium and iodine diffusion in silicon carbide, J. nucl. Mat. **425** (2012) 205-210.

[Fri12] E. Friedland, N. G. Van Der Berg, T. T Hlatshwayo, R. J. Kuhudzai, J. B. Malherbe, E. Wendler, and W. Wesch. "Diffusion behavior of cesium in silicon carbide at T> 1000° C, Nucl. Instrum. and Meth. Phy. Res. Section B: Beam Interactions with Materials and Atoms **286** (2012) 102-107.

[Fri13] E. Friedland, T. T Hlatshwayo, and N. G. Van der Berg. Influence of radiation damage on diffusion of fission products in silicon carbide, physica status solidi c **10** (2013) 208-215.

[Fri14] E. Friedland, K. Gärtner, T. T. Hlatshwayo, N. G. Van Der Berg, and T. T. Thabethe. Influence of radiation damage on xenon diffusion in silicon carbide. Nuclear Instruments and Methods in Physics Research Section B: Beam Interactions with Materials and Atoms **332** (2014) 415-420.

[Gri97] M. G. Grimaldi, L. Calcagno, P. Musumeci, N. Frangis, and J. Van Landuyt. Amorphization and defect recombination in ion implanted silicon carbide. Journal of applied physics **81** (1997) 7181-7185.

[Gül08] O.Ö Gülol, Ü. Çolak, and B. Yıldırım. "Performance analysis of TRISO coated fuel particles with kernel migration. Journal of nuclear materials **374** (2008) 168-177.

[Hla15] T. T. Hlatshwayo, J. H. O'Connell, V. A. Skuratov, M. Msimanga, R. J. Kuhudzai E. G. Njoroge, and J. B. Malherbe. Effect of Xe ion (167 MeV) irradiation on polycrystalline SiC implanted with Kr and Xe at room temperature, J. Phy. D: Appl. Phy. **48** (2015) 465306.

[Hla16] T. T. Hlatshwayo, J. H. O'Connell, V. A. Skuratov, E. Wendler, E. G. Njoroge, M. Mlambo, and J. B. Malherbe. "Comparative study of the effect of swift heavy ion irradiation at 500 °C and annealing at 500° C on implanted silicon carbide. RSC advances **6** (2016) 68593-68598.

[Hos13] P. Hosemanna, J.N. Martos, D. Frazer, G. Vasudevamurthy, T.S. Byun, J.D. Hunn, B.C. Jolly, K. Terrani, M. Okuniewski Mechanical characteristics of SiC coating layer in TRISO fuel particles, J. Nucl. Mat. (2013) 133-142.

[Kim14] T. Kimoto, J. A. Cooper. Fundamentals of silicon carbide technology: growth, characterization, devices and applications. John Wiley & Sons, Singapore (2014).

[Mal08] J. B. Malherbe, E. Friedland, N. G. Van Der Berg, Ion beam analysis of materials in the PBMR reactor. Nuclear Instruments and Methods in Physics Research Section B: Beam Interactions with Materials and Atoms **266** (2008) 1373-1377.

[Mal13] J. B. Malherbe, Diffusion of fission products and radiation damage in SiC, J. Phys. D. Appl. Phys. **46** (2013) 1-52.

[McH93] C. J. McHargue and J. M. Williams, Ion implantation effects in silicon carbide, Nucl. Instrum. and Meth. in Phy. Res. Section B: Beam Interactions with Materials and Atoms **80** (1993) 889-894.

[Mut03] S. Muto, T. Tanabe, Local structures and damage processes of electron irradiated α-SiC studied with transmission electron microscopy and electron energy-loss spectroscopy, Journal of applied physics **93** (2003) 3765-3775.

[Pag16] T. F. Page and S. J. Bull. Ion Implantation in Ceramics. Encyclopedia of Materials: Science and Technology, 2nd Edition, UK, (2016).

[Pet07] J. Peterson, M. MacDonell, L. Haroun, F. Monette, Selenium, Radiol. Chem. Fact Sheets To Support Heal. Risk Anal. Contam, Areas (2007) 46-47.

[Pio19] I. Pioro, R. Duffey, Current and future nuclear power reactors and plants, Academic Press, Canada, (2019).

[Riu18] G. Rius and P Godignon, Epitaxial Graphene on Silicon Carbide: Modeling, Characterization, and Applications. CRC Press, Singapore, (2018).

[Ske16] W. F. Skerjanc, J. T. Maki, B. P. Collin, D. A. Petti Evaluation of design parameters for TRISO-coated fuel particles to establish manufacturing critical limits using PARFUME. Journal of Nuclear Materials **469** (2016) 99-105.

[Slo05] J. Slotte, K. Saarinen, M. S. Janson, A. Hallén, A. Y. Kuznetsov, B. G. Svensson, J. Wong-Leung, and C. Jagadish. "Fluence, flux, and implantation temperature dependence of ion-implantation-induced defect production in 4H–SiC, J. Appl. Phy. **97** (2005): 033513.

[Sne07] L. L Snead, T. Nozawa, Y. Katoh, T. S. Byun, S. Kondo and D. A. Petti, Handbook of SiC properties for fuel performance modeling, J. of nucl. Mat. **371** (2007) 329-377.

[Van10] N.G. van der Berg, J.B. Malherbe, A.J. Botha, E. Friedland, SEM Analysis of the Microstructure of the Layers in Triple Coated Isotropic (TRISO) Particles. Surf. Interface Anal **42** (2010) 1156 -1159.

[Van12] N.G. van der Berg, J.B. Malherbe, A.J. Botha and E. Friedland, Thermal etching of SiC, Appl. Surf. Sci **258** (2012) 5561-5566.

[Wel01] J. Weil, Pebble-bed design returns, IEEE Spectrum **38** (2001) 37-40.

[www1] www.oecd.org/greengrowth, OECD Green Growth Studies, Energy (accessed July 30, 2020).

[www2] www.world-nuclear.org, Nuclear fission and types of nuclear reactor (accessed July 30, 2020).

[www3] www.pub.iaea.org, Pebble Bed Modular Reactor, International Atomic Energy Agency, Vienna, Austria, report 70, (August 2011).

[www4] www.americanelements.com, American Elements, Selenium (accessed July 31, 2020).

[Yvo16] P. Yvon, Structural materials for Generation IV nuclear Reactors, Woodhead Publishing, Amsterdam, Netherlands, (2016).

[Zha17] H. Zhang, X. Wang, Z. Chen, F. Sun, Z. Zhang, and D. Tang. An experimental study on thermal conductivity of silicon carbide via the TDTR method under low temperatures. Kung cheng je wu li hsueh pao **38** (2017) 1415-1421.

[Zin96] S. J. Zinkle and L. L. Snead. Influence of irradiation spectrum and implanted ions on the amorphization of ceramics, Nucl. Instrum. and Meth. Phy. Res. Section B: Beam Interactions with Materials and Atoms **116** (1996) 92-101.

CHAPTER 2

DIFFUSION

It is well known in crystallography that the atoms in a crystal are arranged in a certain periodic pattern. In the solid-state, these atoms vibrate around their fixed positions. As a substance is heated, the average kinetic energy increases, causing the atoms to oscillate faster and increase the amplitude of the vibrations. If the average kinetic energy is great enough to break the bonds between neighbouring atoms, atoms can move from its original lattice site to another position in the crystal lattice.

In inhomogeneous materials, assuming that heat is delivered to materials, when the thermal energy is higher than the intermolecular potential energy, the atoms move from a region with a higher concentration to a region with a lower concentration. The random motion of atoms, ions or molecules from a higher concentration region to another with lower concentration as a result of their kinetic energy is called diffusion. Diffusion plays a key role in many processes, such as doping of silicon and other semiconductor materials used in the manufacture of semiconductor devices, as well as in homogeneous and heterogeneous catalytic reactions [Meh07]. Diffusion processes are relevant to many microstructural changes that take place during the preparation and heat treatment of materials [Meh07]. It is very important to understand these processes well. The rates of important chemical reactions depend on how fast the diffusion can bring the reactants together [Meh07]. This information can be defined in the term diffusion coefficient, which expresses the number of atoms passing through an area per unit time.

2.1 Steady State and Time Dependent Diffusion

Diffusion can be classified into two major types as steady state and time dependent diffusion.

2.1.1 Steady state diffusion

Steady state diffusion occurs when the number of atoms crossing a certain interface is constant over time. If the concentration (c) indicates the number of diffusing particles per unit volume as in our case (atom/m^3), the flux (J) in one dimension is the number of particles that crossing unit area per unit time (atom/m^2. sec) [Zhi10]. In steady state diffusion, the concentration gradient or the change in concentration due to a change in position gives a constant value as

illustrated in Fig. 2.1, while the change in concentration with time (dc/dt) equals zero. This type of diffusion are described by Fick's first law given by the following equation [She63]:

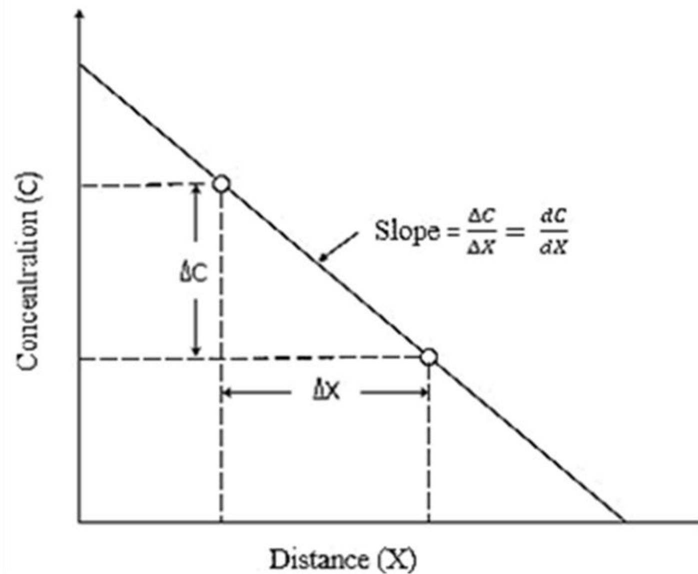

Fig. 2.1: A schematic change in concentration as a function of distance in a one-dimensional space.

$$J = -D\,\frac{\partial c}{\partial x} \qquad (2.1)$$

where J is flux of atoms (atoms/ (m^2 s)), D is diffusivity or diffusion coefficient (m^2s^{-1}) and $\frac{\partial c}{\partial x}$ is concentration gradient (atoms/m^4). The negative sign indicates that diffusion occurs against the concentration gradient.

From equation (2.1), we can see that the particle flux is proportional to the concentration gradient and constant of this proportionality is the diffusion coefficient (D).

Equation (2.1) can be reformulated to obtain the flux in three-dimensional space as follows:

$$J_x = -D\,\frac{\partial c}{\partial x}\,, \quad J_y = -D\,\frac{\partial c}{\partial y}\,, \quad J_z = -D\,\frac{\partial c}{\partial z} \qquad (2.2)$$

It can be rewritten by combining them together and using vectorial notation:

$$\vec{J} = -D\left(\frac{\partial y}{\partial x},\quad \frac{\partial y}{\partial x},\quad \frac{\partial y}{\partial x}\right) \qquad (2.3)$$

$$\vec{J} = -D\ \vec{\nabla} C$$

where $\vec{\nabla}$ is gradient operator of three-dimensional space.

2.1.2 Time dependent diffusion

In this type of diffusion, the change in particles concentration over time, i.e. (δc /δt) is not equal to zero, and the change in concentration with distance (δc/δx) does not give a constant value. Consider a bar with a uniform rectangular cross-section area (A) and a small volume with length (dx) as illustrated in Fig. 2.2. J_1 and J_2 denote the fluxes of impurities entering and leaving the volume element, respectively. If the concentration of the diffusing impurity changes along the volume, the flux changes. Thus J_1 and J_2 are no longer the same.

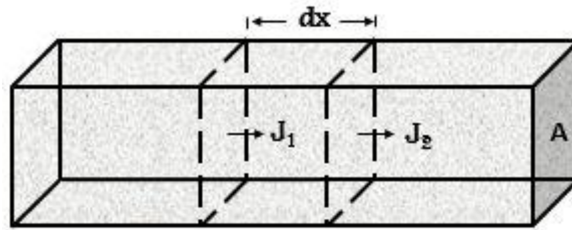

Fig. 2.2: A schematic change in flux in and out a volume element with a uniform cross-sectional area.

Since the number of impurity particles in the volume element is a product of the concentration and differential volume element in the rectangular coordinate system (A.dx), the continuity equation can be written as:

$$Adx\frac{\delta c}{\delta t} = -A(J_2 - J_1) \qquad (2.4)$$

$$\frac{\delta c(x,t)}{\delta t} = -\frac{\partial \mathrm{J}}{\partial \mathrm{x}} \qquad (2.5)$$

From Fick's first law Eq. (2.1), the above equation can be rewritten as:

$$\frac{\delta c(x,t)}{\delta t} = \frac{\partial}{\partial \mathrm{x}}\left(D\frac{\partial \mathrm{c}}{\partial \mathrm{x}}\right) \qquad (2.6)$$

If D is not a function of position (x), then Eq. (2.6) is reduced to:

$$\frac{\delta c(x,t)}{\delta t} = D\ \frac{\delta^2 c(x,t)}{\delta^2 x} \tag{2.7}$$

This is Fick's second law in one -dimensional space [Sha73].
For three -dimensional space, it can be written as:

$$\frac{\delta c}{\delta t} = D\ .\nabla^2 C \tag{2.8}$$

where

$$\nabla^2 = \frac{\delta^2}{\delta^2 x} + \frac{\delta^2}{\delta^2 y} + \frac{\delta^2}{\delta^2 z} \tag{2.9}$$

2.2 Arrhenius' law

Arrhenius suggested that for the molecules to interact, they must possess a certain amount of energy [Bro94]. The minimum amount of energy required to activate atoms or molecules to be conducive to chemical transformation or physical transportation is called the activation energy [Deb14]. Therefore, a chemical reaction can only occur once molecules possess enough kinetic energy to overcome the activation energy barrier. Increasing the temperature generally speeds up the process, viz, the rate of diffusion increases. This is due to the ability of atoms to move faster on average as a result of their increased kinetic energy. The diffusion coefficient generally obeys the exponential Arrhenius' law, which depends on the temperature Eq. (2.10) [Ash14].

$$D = D_o\ exp\left(\frac{-E_A}{k_B T}\right) \tag{2.10}$$

$$\ln D = -\frac{E_A}{k_B}\left(\frac{1}{T}\right) + \ln D_o \tag{2.11}$$

Where D is the diffusion coefficient, D_o is a pre-exponential factor, E_A is the activation energy, k_B is Boltzmann's constant and T is the absolute temperature (in kelvin). The activation energy can be determined from the slope of the linear relation between the logarithm of D and the inverse temperature Eq. (2.10) as shown in Fig. 2.3.

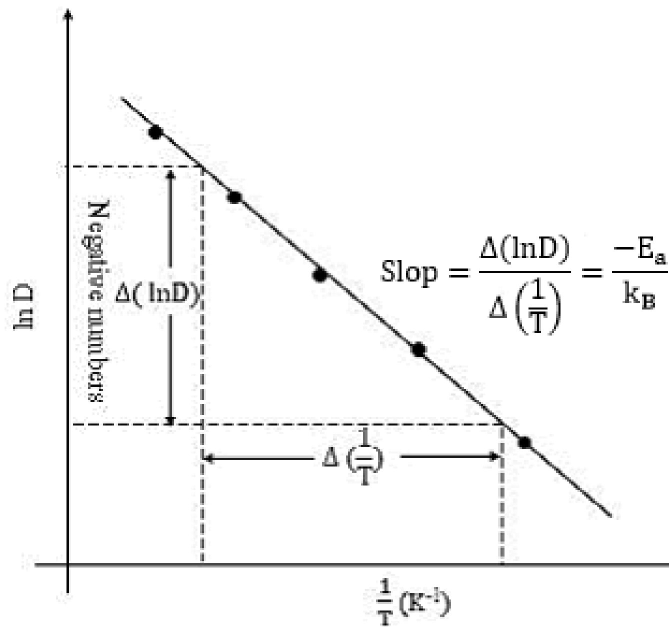

Fig. 2.3: *Arrhenius plot of the linear relationship between ln D and 1/T.*

2.3 Defects

In solid crystalline materials, diffusion is mainly related to defects in the crystal structure. Defects in crystals can be classified into three types: point, line and surface defects. They are discussed below.

2.3.1 Point defects

Point defects occur where an atom is lost or is in an irregular place in the lattice structure. They can be sorted into three main types: vacancies, interstitial defects and substitutional defects [Mou12] as depicted in Fig. 2.4. Point defects are classified according to their dimension as zero-dimensional (0-D) defects [Got04].

A vacancy defect is created when an atom is missing from its original lattice site in a crystal structure. An interstitial defect occurs when an atom is positioned in interstitial site viz., the open space between the original lattice sites in a crystal structure. Interstitial defect can be classified into two types:

1. A self-interstitial defect is where an atom of the same crystal occupies an interstitial position.
2. An interstitial impurity defect is created due to the occupation of an interstitial site in the crystal structure by a foreign atom.

A substitutional impurity defect is created when a foreign atom takes up the lattice position of an atom in a crystal structure.

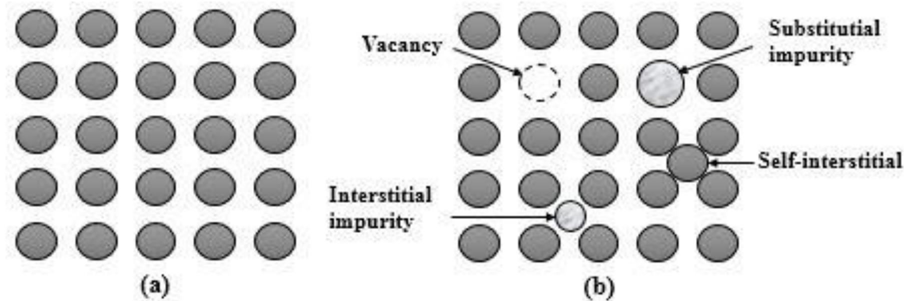

Fig. 2.4: *Schematic diagram of a crystalline structure:(a) perfect crystal (b) crystal with the three basic types of point defects.*

2.3.2 Line defects

Line defects, also known as dislocations or one-dimensional (1-D) defects, are anomalous changes in the regular ordering of atoms, which leads to irregular spacing along a line in the solid [Kai11]. These defects have a strong influence on the mechanical properties of solids [Kai11]. There are two basic types of dislocations, edge dislocation and screw dislocation, as shown in Fig. 2.5 (a) and (b).

An edge dislocation occurs either due to the addition or loss of half of a plane of atoms in the crystal lattice. The presence of a half plane of atoms in the crystal lattice creates a compression and tension in the region above and below, respectively. A screw dislocation occurs when part of the plane moves to the opposite direction of other planes of atoms in the crystal lattice [Bab08].

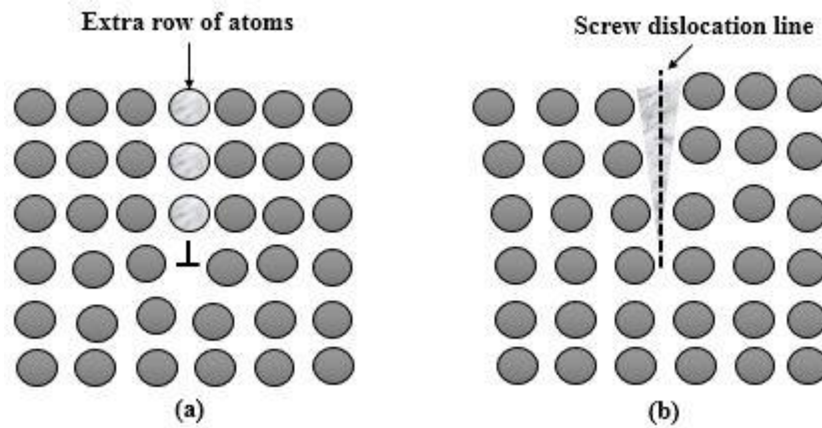

Fig. 2.5: *Schematic diagram of line defects: (a) edge dislocation and (b) screw dislocation in an atomic lattice.*

2.3.3 Planar defects

Planar defects are interruptions of the perfect crystal structure across a plane. Fig. 2.6 shows the different forms of planar defects include grain boundaries, twin boundaries and stacking faults defects. They are classified based on their dimensionality into two-dimensional (2-D) defects.

The grain boundaries are more interesting in this study as the samples are polycrystalline. Grain boundaries are interfaces that separating crystal grains with different orientations in polycrystalline materials [Ste14]. The difference in crystalline orientations between two neighbouring crystals relative to each other is called the misorientation angle [Mor04]. Some physical properties, such as crystal morphology and surface topography are strongly correlated with changes in the crystal orientation. Within these boundaries, the atomic density is low and the atomic arrangement is irregular, and the energy increases with increasing misorientation angle [Ste14]. The grain boundaries can accommodate impurities, subsequently providing easy pathways for diffusion under suitable conditions.

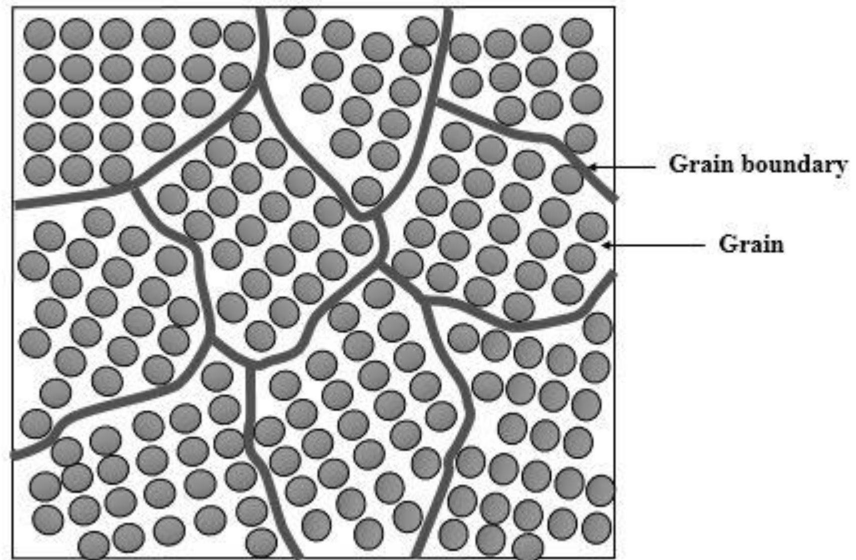

Fig. 2.6: *Schematic illustration of grain boundaries.*

2.4 Diffusion mechanisms

In solid state materials, the diffusion mechanism is highly dependent on the crystal structure and temperature. Atoms in crystalline solids oscillate around their equilibrium positions and the mean amplitude of the oscillations increases with increasing temperature. There are two main conditions required for a diffusion process:

1. There must be an empty adjacent site, and
2. The atom must have sufficient energy to break bonds with its neighbouring atoms.

The diffusion mechanism is mostly associated with crystal defects. It can be happen via different modes such as lattice and along high diffusivity paths.

Lattice diffusion (is also termed volume or bulk diffusion) indicates the atomic diffusion within a crystalline lattice, which occurs by either vacancy, interstitial or substitutional mechanisms. The vacancy mechanism occurs when a substitutional atom moves to an adjacent vacancy in the host crystal. In other words, there is an exchange between an atom and neighbouring vacancy in this mechanism as illustrated in Fig. 2.7 (a). Sufficient energy and time are needed for an atom-vacancy exchange to occur [Pel16]. In interstitial diffusion, the impurity atom moves from one interstitial site to another as shown in Fig. 2.7 (b). This mechanism usually occurs when the impurity is smaller in size than the host crystal atoms, because the lattice distortion energy for smaller impurity is less than that of a larger atomic sized impurity. Therefore, smaller impurity atoms diffuse more easily with a relatively small diffusion activation. In the interstitialcy mechanism, an interstitial atom occupies the nearest position of

an atom on a normal lattice site by pushing it into another interstitial position. In this case, it is called a self-diffusion mechanism. Whereas the impurity-diffusion mechanism occurs when the self-interstitial atom replaces a substitutional impurity atom, and the replaced atom moves

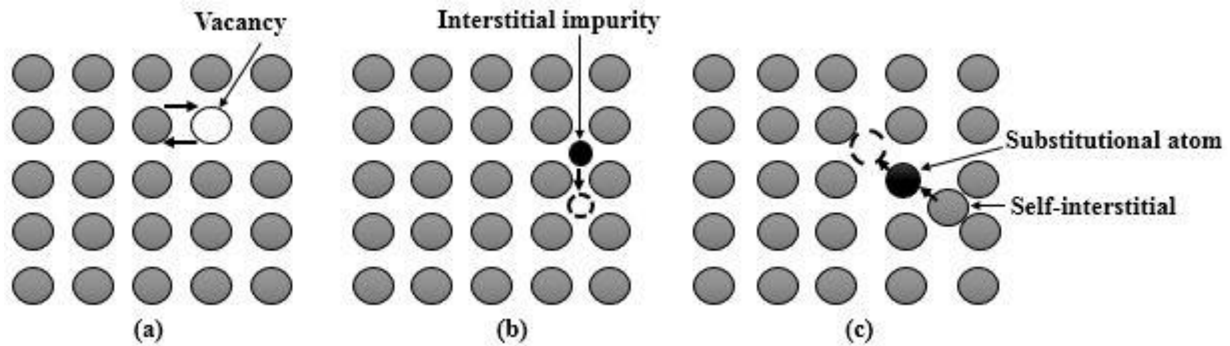

Fig. 2.7: *An illustration of diffusion mechanisms and point defects: (a) Vacancy, (b) Interstitial and (c) interstitialcy diffusion.*

to an interstitial position as shown in Fig. 2.7 (c).

High diffusivity paths indicate diffusion through grain boundaries, dislocations, free surfaces, etc. in crystalline solid material. These paths can act as short circuits for diffusing atoms because their mobility along such defects is usually much faster than in the lattice. In polycrystalline solids, diffusion of atoms is so complicated, because of the possibility of two mechanisms, lattice diffusion and diffusion through high diffusivity paths simultaneously. The last one dominates at low temperatures due to the high disorder along the boundaries. In most cases, an increase in temperature leads to reducing the level of damage along these boundaries, consequently dominating the lattice diffusion. This dominance might be due to the migration of impurities from grain or dislocation boundaries into lattices.

In this study, since our material is a polycrystalline SiC implanted at different temperatures, all kinds of defects play a role in the diffusion rate during heat treatment. Some of these defects are created either during the formation of the crystalline materials or during the ion implantation process. The creation of defects during ion implantation depends on many factors, such as the temperature of the substrate. In this study, more defects are retained in the sample implanted at room temperature compared to those implanted at high temperatures (350 °C and 600 °C). Moreover, at high temperatures, the defect of samples implanted at 350 °C is higher than those implanted at 600 °C. This is due to the fact that atoms have a greater average kinetic energy to move around and recombine with their original lattice sites at higher temperatures.

References

[Ash14] S. A. Ashter, Thermoforming of Single and Multilayer Laminates: Plastic Films Technologies, Testing, and Applications, 1st Edition, William Andrew publishing, Elsevier, Amsterdam, Netherlands, (2014).

[Atk89] A. Atkinson, C. Monty, Grain boundary diffusion in ceramics, Springer, Dordrecht, (1989).

[Bab08] B. Babu, Physically based model for plasticity and creep of Ti–6Al–4V, Licentiate Thesis, Lulea University of Technology, Lulea, Sweden, (2008).

[Bro94] T. L. Brown, H. E. LeMay, B. E. Bursten and B. E. Bursten, Chemistry: the central science, 3rd Edition, Englewood Cliffs, NJ: Prentice Hall, (1994).

[Deb14] P. Deb, Kinetics of heterogeneous solid state processes, New Delhi, India Springer, (2014).

[Got04] G. Gottstein, Physical foundations of materials science, Springer, Berlin, Heidelberg, (2004).

[Kai11] S. V. Kailas, Materials Science, Indian Institute of Science, Bangalore, India, (2011).

[Meh07] H. Mehrer, Diffusion in Solids: fundamentals, methods, materials, diffusion-controlled processes, Springer, Berlin, (2007).

[Mor04] A. Morawiec, Misorientation Angle and Axis Distributions, Springer, Berlin, Heidelberg, (2004).

[Mou12] A. P. Mouritz, Introduction to Aerospace Materials, 1st Edition, Woodhead publishing in Material, Elsevier, Royal Melbourne Institute, Australia, (2012).

[Pel16] J. Pelleg, Mechanism of Diffusion, Springer International Publishing, Switzerland, (2016).

[Pet82] N. L. Peterson, Diffusion mechanisms in grain boundaries in solids, Argonne National Lab., USA, (1982).

[Sha73] D. Shaw, Atomic diffusion in semiconductors, Plenum, London, (1973).

[She63] P.G. Shewmon, Diffusion in solids, McGraw-Hill, New York, (1963).

[Ste14] W. Steurer, Crystal structures of metallic elements and compounds, Physical Metallurgy, Elsevier, Amsterdam, Netherlands, (2014).

[Zhi10] L. Zhigilei, Introduction to the Science and Engineering of Materials, University of Virginia, Department of Materials Science and Engineering, United States, (2010).

CHAPTER 3

ION IMPLANTATION

Ion implantation is a process used to change the chemical, electrical and physical properties of solids. In this process, the desired elements/ impurities are subject to ionization first, which is the process by which an atom or a molecule gains a negative or positive charge by gaining or losing electrons, resulting in ions accompanied by chemical changes. The ions are then accelerated toward the target with a particular energy, usually, less than one megavolt (MeV). When accelerated ion penetrates a target material it loses its energy via collisions with the atoms until it stops moving at a certain depth from the surface. It is worth noting that collisions with target atoms can be classified as elastic and inelastic which are considered independent of each other.

An energetic ion travelling through a target material loses a large part of its energy to electronic excitations, except for the last part of its range where nuclear stopping is significant [Arn94]. This chapter points to matters which predict the final distribution of the ions in the target material.

3.1 The Stopping Power and Range

When a solid target is bombarded by an energetic ion beam, loses its energy due to a series of collisions with the host atoms until it settles to a certain depth. The stopping power or energy loss (dE/dx) is the quantity by which the final distribution of ions and defects is determined, given by the following equation:

$$S = \frac{dE}{dx} \qquad (3.1)$$

The stopping power is classified into nuclear stopping and electronic stopping. They are considered as processes independent from each other. Consequently, the total stopping power can be calculated by the sum of the nuclear and electronic stopping as follows:

$$S_t = S_n + S_e \qquad (3.2a)$$

$$\left.\frac{dE}{dx}\right|_t = \left.\frac{dE}{dx}\right|_n + \left.\frac{dE}{dx}\right|_e \quad (3.2b)$$

where subscripts t, n and e indicate the total stopping power, nuclear stopping and electronic stopping, respectively.

As shown in Fig. 3.1, at low energy, the nuclear stopping is large compared to the electronic stopping. The electronic stopping begins takeover above the critical energy and reaches its maximum value at $v_i = v_o z^{2/3}$, then decreases at Bethe-Bloch region ($v_i >> v_o z^{2/3}$), where v_i is the velocity of the ion, v_o is the velocity of Bohr and z is the atomic number of the ion. We will discuss these in more detail in the following subsections.

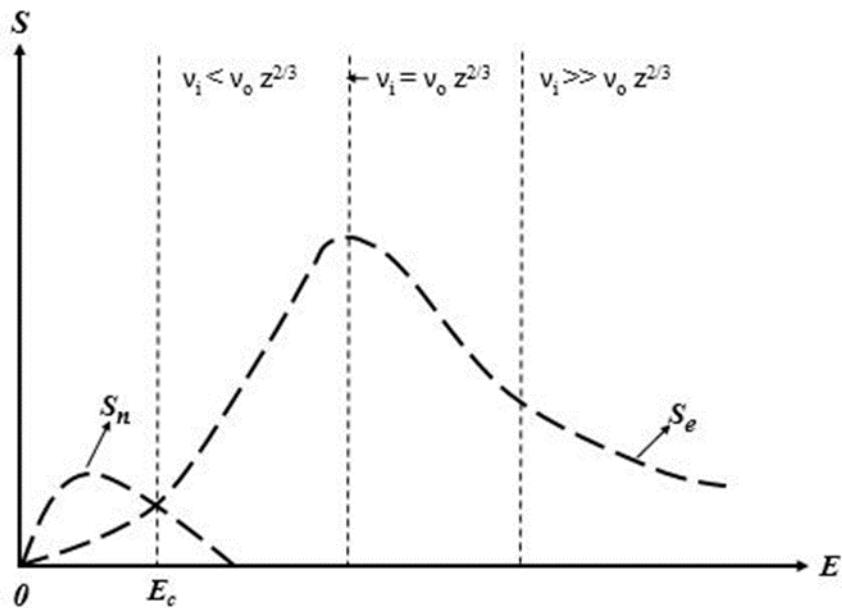

Fig. 3.1: The nuclear and electronic stopping power as a function of energy of implanted ion.

Microscopically, the cross-section of the target is the area within which it can be struck by some projectiles (see Fig. 3.2 The cross-section is also an effective area that describes the probability of a projectile particle hitting or interacting with the target's atoms. The greater the cross-section area of the target atom, the higher the probability.

The stopping cross section is defined as the total stopping power divided by the host target density, which is written as:

$$\varepsilon = -\frac{1}{N}\frac{dE}{dx}\bigg|_t \tag{3.3a}$$

$$\varepsilon = -\frac{1}{N}\left(\frac{dE}{dx}\bigg|_n + \frac{dE}{dx}\bigg|_e\right) \tag{3.3b}$$

where ε is the stopping cross section and N is the target density. Here a negative sign means that the energy of the particle decreases during penetration of the target.

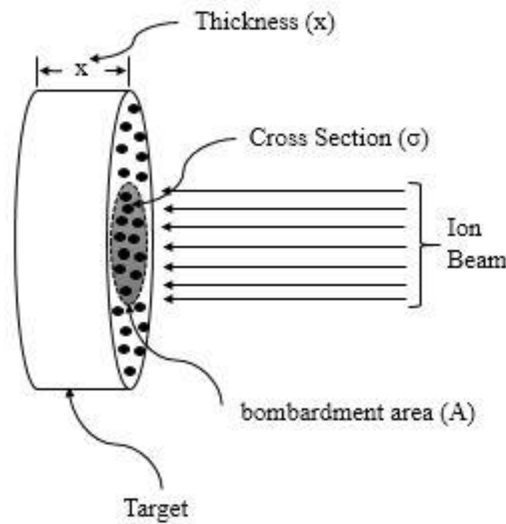

Fig. 3.2: Ion beam and cross section of one microscopic target.

From equation (3.3a), the total path length (L_t) can be found by integrating both sides of the differential equation:

$$\int_0^x dx = -\frac{1}{N}\int_0^{E_0} \frac{1}{\varepsilon(E)}\, dE \tag{3.4a}$$

$$\int_0^x dx = R = -\frac{1}{N}\int_0^{E_0} \frac{1}{\varepsilon(E)}\, dE \tag{3.4b}$$

where R is the penetration length and E_o is the initial incident energy of ions.

3.1.1 Nuclear Stopping

Nuclear stopping power is a process that leads to the transfer of energy from the implanted ion into the target atoms. This process involves a series of two-body elastic collisions between the ion and the target atoms. In these collisions, the energy transferred from the ion may be sufficient to displace an atom from its lattice position, viz. it causes displacement damage in its atomic structure. Ion-target atom interaction potential effects have been investigated using various models including interatomic screening, solid state potential, and statistical atomic models. It has been found that nuclear scattering can be described by the Coulomb potential multiplied by a screening function as follows:

$$V(r) = \frac{Z_1 Z_2 e^2}{4\pi\varepsilon_o r} \emptyset\left(\frac{r}{a}\right) \qquad (3.5)$$

Where Z_1 and Z_2 are the atomic numbers of the incident ion and target atom respectively, e is the electron charge, ε_o is the permittivity of free space, r is the separation distance, a is the screening length and $\emptyset\left(\frac{r}{a}\right)$ is a screening function of the reduced radius r/a that depends on the charges of the involved atoms [Tes95].

When the target is bombarded by energetic ion, a sufficient kinetic energy and momentum may be imparted to the target atom. This is due to elastic coulomb interactions between the nuclei of the ion and target atom. The laws of conservation of momentum and energy can be used to determine kinetic energy T, and it's given by:

$$T_{max} = \frac{4M_1 M_2}{(M_1 + M_2)^2} E_o sin^2\left(\frac{\theta}{2}\right) \qquad (3.6)$$

here M_1 and M_2 are the atomic masses of the incident ion and target atom, respectively. As a result of collision, the ion of mass is deflected by the target atom at an angle with respect to the M1 original trajectory as shown in Fig. 3.3.

When the scattering angle of the incident ion equals 180° ($\theta = \pi$), the transferred kinetic energy reaches its maximum value. $T_{max} = \frac{4M_1 M_2}{(M_1+M_2)^2} E_o$. Thus, equation 3.6 can be rewritten as:

$$T = T_{max}\, sin^2\left(\frac{\theta}{2}\right) \qquad (3.7)$$

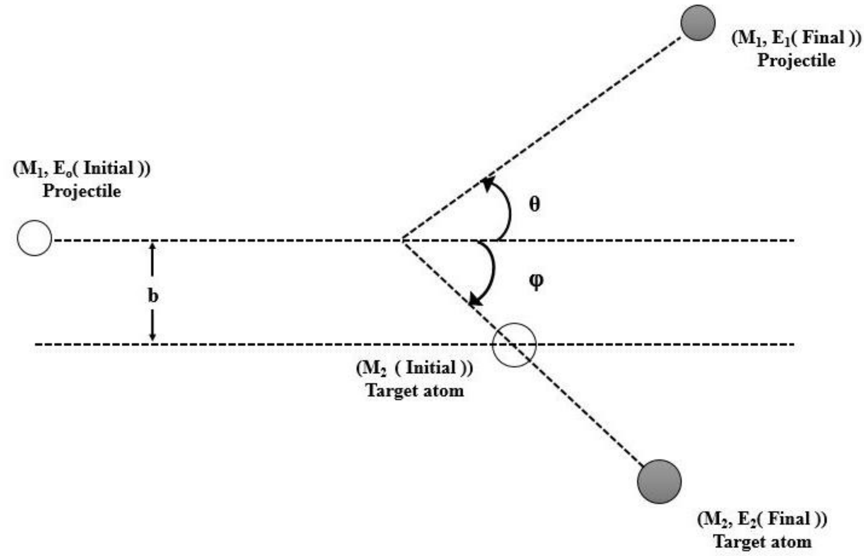

Fig. 3.3: A schematic diagram showing a scattering of an energetic ion by a target atom in the laboratory.

If maximum possible amount of kinetic energy transferred from an incident ion to a target having a density of N atoms per unit volume, the average nuclear stopping (S_n (E)) is determined using the probability of a collision by the scattering cross-section reaction (σ), and is expressed as follows [Zie88].

$$S_n(E) = N \int_0^{T_{max}} T d\sigma, \qquad d\sigma = 2\pi b db \qquad (3.8)$$

Thus, the energy transferred to the target atoms over all collision parameters is given by

$$S_n(E) = 2\pi \int_0^{b_{max}} T\,(E,\theta)\, bdb \qquad (3.9)$$

By substituting equation 3.6 in the above expression, we obtain:

$$S_n(E) = 2\pi \frac{4M_1M_2}{(M_1+M_2)^2} E_o \int_0^{b_{max}} sin^2\left(\frac{\theta}{2}\right) bdb \qquad (3.10)$$

3.1.2 Electronic Stopping

In electronic stopping, energetic ion penetrating a substrate loses its energy through inelastic interactions with target electrons. The mechanism is complicated compared to nuclear stopping, which is previously discussed. This is due to the several processes that facilitate convey of kinetic energy from the incident ion to the target electrons. The processes include electron-electron interactions via two-body collision, excitation, ionization or electron capture of the incident ion and excitation or ionization of target atoms [Tow94].

The electronic energy loss is described by a model based on the ion velocity. By comparing the velocity of the ion (ν_i) with the Bohr velocity ($\nu_o = e^2/\hbar$ *where* e is the electron charge and ħ is the Planck's constant), it is categorized into three different ion energy regimes: low, intermediate and high energies as shown in Fig.3.1.

In this theory, the hydrogen atom at 25 keV moves with a velocity equal to the velocity of its orbital electron, while a helium atom at 252 keV moves with a velocity equal to the velocity of its orbital electrons. Thus, the initial energy of an ion move with the same velocity as its orbital electron can be written as a function of the atomic number (Z_i) and mass number (A_i) of the ion as follows:

$$E = {Z_i}^{4/3} A_i \, 25 \quad keV \qquad (3.11)$$

In the first region, the model deals with the low energy regime where the ion's velocity is lower than $\nu_o z^{2/3}$. Z here represents the atomic number of the energetic ion.

In the first region, the model deals with the low energy regime where the ion's velocity is lower than $\nu_o z^{2/3}$. Z here represents the atomic number of the energetic ion.

Selenium implanted at 200 kV has an initial velocity (ν_i) of 2.2 x 10^4 m / s, which is much lower than the Bohr velocity of the electrons ($\nu_o = 2.2 \times 10^6$ m/s) [Nas14]. This energy is not enough to be transferred to electrons that are much lower in energy than the Fermi level. Therefore, only electrons in energy levels close to the Fermi level are considered in the energy loss. The electronic stopping in this low energy regime can be estimated by The Lindhard's particle-plasma interaction theory. Assuming the presence of a free-electron gas with a density ρ, the electronic stopping cross section (ε_o) of an ion with Z_1 is given by [Lin53] [Zie88].

$$\varepsilon_o = \int I(\nu, \rho) \, (Z_1(\nu))^2 \, \rho dV \qquad (3.12)$$

Where I is the stopping interaction of an ion of unit charge, v is the ion velocity, ρ the free electron gas density and dV is a volume element of the target.

In the second region, the intermediate energy regime, the ion's velocity is approximately ($v_i \approx v_o Z^{2/3}$) as illustrated in Fig.3.1. In this energy regime, the ion is partially ionized and the electronic stopping reaches its maximum value.

In the third region, also known as the Bethe-Bloch region, the model deals with the high energy regime where the ion's velocity is much greater than $v_o z^{2/3}$. The incident ion is fully stripped of all its electrons. The energy loss in this regime is calculated by the Bethe-Bloch equation:

$$\varepsilon_e = \frac{4\pi Z_1 Z_2 e^4}{m_e v_1^2}\left[\ln\frac{2m_e v_1^2}{I} - \ln(1-\beta^2) - \beta^2 - \frac{C}{Z_2} - \frac{\delta}{2}\right] \qquad (3.13)$$

where Z_1 and Z_2 are the incident ion and the target atomic numbers respectively, m_e is the mass of the electron, v_i is the velocity of the incident ion, I is the average excitation energy, $\beta = v/c$ where c is the speed of light, C/Z_2 is the shell correction., $\delta/2$ is the correction of density effect taking into account the decrease in stopping power as a result of the dielectric polarization of the medium at very high kinetic energies.

The average excitation energy in the above equation is given by [Kam84].

$$\ln I = \sum_n f_n \ln(E_n - E_o) \qquad (3.14)$$

Where f_n is the corresponding oscillator strength for transitions from the ground state (E_o) to the possible energy (E_n) transitions. The average excitation energy of the electrons of the target can be estimated by Block's rule [Blo33].

$$I = I_o Z_2, \qquad I_o = 10\ eV \qquad (3.15)$$

This study reviews selenium ions implanted into silicon carbide with an energy of 200 keV. This energy is within the low energy regime. Rutherford backscattering spectrometry (RBS) analysis was carried out using helium particles with an energy of 1600 keV which is within the intermediate energy regime.

3.1.3 Energy Loss in Compounds

The compound here is a target consisting of more than one component. Since the target material in this work is silicon carbide, it is very important to discuss energy loss in the compound materials.

If the target atom is made up of two elements A and B as in our case, the total stopping of an ion moving through it can be calculated using a simple additional rule. It is assumed that to be independent encounters taking place one at a time. Based on this assumption, the total stopping cross-section $\varepsilon^{A_m B_n}$ is written as:

$$\varepsilon^{A_m B_n} = m\varepsilon^A + n\varepsilon^B \qquad (3.16)$$

where $\varepsilon^A$and ε^B are the stopping cross sections and m and n are the relative molar fractions of the elements in the compound (A and B), respectively [Bra05]. This equation is known as the Bragg rule. Experimentally, it has been found that the energy loss slightly deviates from Bragg's rule. This is due to the fact that the rule assumptions that the projectile ion-target atom interaction is independent of the environment [Tes95]. Therefore, a new model is needed to correct the chemical and physical state of the medium, influence the energy loss. In the Cores and Bonds (CAB) model developed by Ziegler *et al* [Zie88], the effects state of the non-bonding core electrons and the bonding valence electrons are involved. Determination of correction in this method is based on knowledge of the bond structures of the compound.

3.1.4 Energy Straggling

An energetic incident ion penetrating a target material loses its energy via many interactions with the target atoms. This result in statistical fluctuations, which means identical ions with the same initial energy will not have the same energy after passing through a thickness (x). This phenomenon is called energy straggling [Chu78].
Theoretically, the energy staggering phenomenon can be described by Bohr's theory (3.16), which is derived from the Bethe-Bloch equation (3.12) [May77]. This theory assumes that the target atoms are randomly distributed, and the incident ion velocity is higher than the orbital velocities of the target electrons and only a slight change in ion energy during penetration [Bon71].

$$\Omega_B^2 = 4\Pi Z_1^2 Z_2 e^4 N \Delta X \quad (3.17)$$

Where Ω^2_B is Bohr's energy straggling, Z_1 and Z_2 are the projectile and target atomic numbers, respectively, N is the atomic density and ΔX is the thickness of the target. The full width at half maximum (FWHM) of the ion energy distribution, typically described by a Gaussian distribution in most cases, can be expressed as:

$$FWHM = 2\,\Omega_B\sqrt{2\ln 2} \quad (3.18)$$

To accommodate the energy corrections where the assumptions are not valid, Bohr's theory of straggling has been modified by Lindhard *et al.* [Lin53]. They have been extended this theory to include corrections for energies where the assumptions may not be valid particularly at low and medium energies.

3.2 Mathematical model of ion implantation

As previously reported, when an incident ion enters the target surface it collides with the atoms and their electrons as well, which reduces the ion's energy until it finally comes to rest within the target. This interaction is a statistical process and the simplest approximation of the ion implantation profile is Gaussian distribution, which can be expressed mathematically as in the equation (3.19) below. The parameters that are usually used to describe the Gaussian distribution of implanted ion are the projected range R_p and the range straggling (see Fig. 3.4(a)) [Jah81]. The projected range (R_p) is the parameter that determines the average range of distance traveled by particles before stopping [Wil86]. This projected range is usually less than the total path length, due to the effect of nuclear and electronic stopping on the ion path during it penetrates the target as shown in Fig. 3.4(b). The range straggling (ΔR_p) is standard deviation of the distribution of implanted ions, providing a measure of the profile spreading. There are two other important parameters to get an adequate characterization for ion implantation profile: skewness (γ) and kurtosis (β), which measure the asymmetry and peak sharpness of profile, respectively.

$$N(x) = N_p exp\left[-\frac{(x-R_p)^2}{2\Delta R_p^2}\right] \quad (3.19)$$

where N(x) is the concentration of ions as a function of the depth from the surface and N_p is the concentration of ions at a depth equal to the projected range ($x = R_p$).

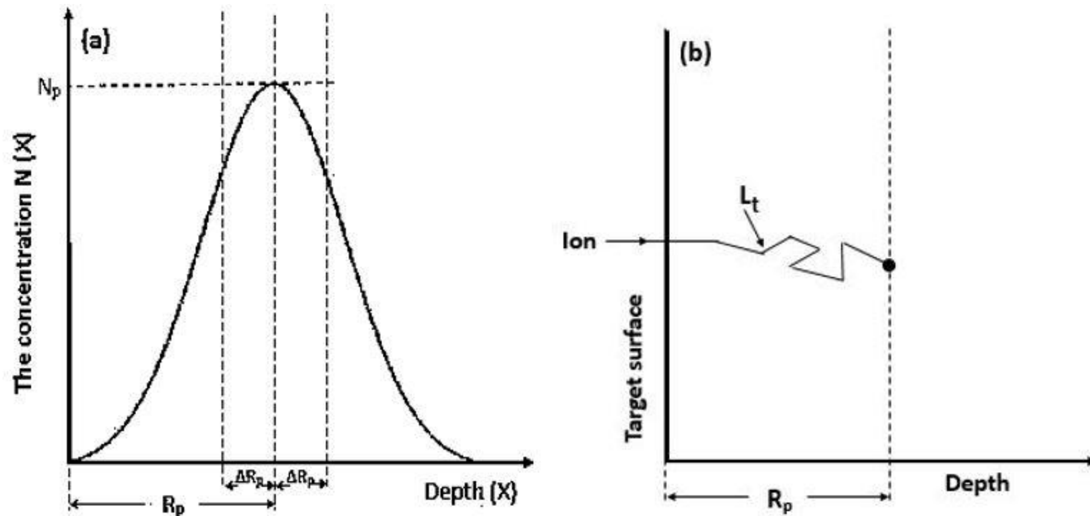

Fig. 3.4: The schematic diagram of implanted ions (a) the parameters of normal distribution, (b) the projected range and total path length.

3.3 Simulation of ion implantation

Although the simulation is not accurate compared to the experiment, it can bring you closer to reality. This provides a good idea of the expected experimental results. In this work, the **S**topping and **R**ange of **I**ons in **M**atter (SRIM) program was used to calculate interaction of selenium ions with silicon carbide. This program uses on a Monte Carlo simulation method, called the binary collision approximation [Sri12]. If the ion type and energy (in the range 0.1 keV – several MeV) and the material target layer are determined, then four moments of as implanted profile can be extracted, which are projected range Rp, projected range straggling ΔRp, the skewness (γ) and the kurtosis (β) [Zie85b].

When performing the calculations, TRIM program assumes the following:

- The interaction of incident ion and a target atom is a binary collision, thus the influence of neighbouring atoms is neglected.
- The process of recombination of interstitial atoms with the vacancies is ignored.
- The ion is assumed to change direction due to binary collisions and the projected range is affected only by these collisions.
- The target is an amorphous material, and consequently hence crystal orientation effects are neglected.
- The thermal effects in the solid are not taken into account i.e. redistribution of the implanted ions in target due to thermal annealing is neglected.

- The electronic stopping power is an averaging fit of data from a large number of experiments.

Despite these assumptions, the accuracy of TRIM calculations is about 5-10% error. This accuracy of TRIM is also done by the fact that it does not take into consideration changes in the crystal structure and dynamic composition of the target material during implantation. Fig. 3.5. Shows the TRIM simulation of a 200 keV Se ions implanted in the SiC. These results will be discussed and compared with experimental results obtained from Rutherford Backscattering spectrometry (RBS) in the results and discussions chapter.

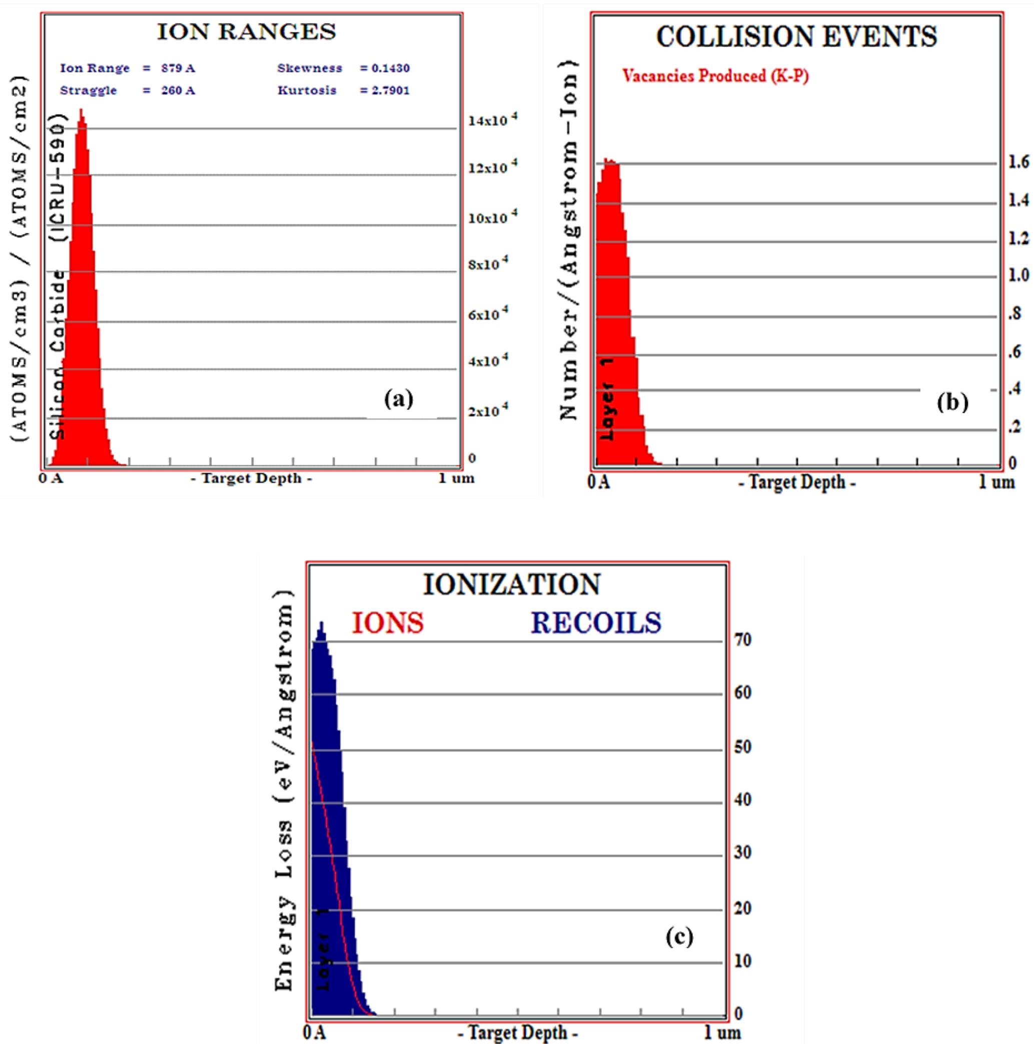

Fig. 3.5: A TRIM simulation of 200 keV Se ions implanted into SiC showing distribution of (a) ion range (b) vacancies (c) ionization.

3.4 Radiation damage formation and annealing in SiC

It has been recognized for many years that bombardment by a flux of energetic ions leads to changes in the physical and properties of a solid target. Most of these changes are attributed to radiation damage processes. A proper understanding of this phenomenon and how to control it is necessary in the study of ion implantation. The radiation damage caused by implantation depends on several parameters including the implant species, the incident energy, fluence and substrate material and substrate temperature [Car82].

Silicon carbide (SiC) is readily amorphized by ion implantation at room temperature. Amorphization width, as measured by Rutherford backscattering spectrometry (RBS) take place for damage energy of about 20 eV/atom. This is corresponding to 0.2 to 0.3 displacements per atom (dpa) at room temperature [McH93]. A comprehensive review by Malherbe [Mal13] showed that the ion implantation at 300 °C does not amorphous crystalline SiC although damage is present. The thermal annealing of radiation damage in SiC has been reported in several publications [Mal13] [Fri09] [Fri11] [Fri13]. These studies concluded that recovery of damage at the amorphous damage level is achieved by annealing at and above 900°C. This is the temperature required to change disordered Si-C bonds into the ordered SiC structure [Wes96].

In this work, we investigated the influence of heat treatment on the structure of silicon carbide after bombarded with Se ions at different temperatures (RT, 350°C and 600°C). All samples were annealed under vacuum at different temperatures ranging from 1000 to 1500 ˚C. The results are discussed in detail in the result chapter.

References

[Arn94] A. Arnau, Charge states and energy loss of ions in solids, Nuclear Instruments and Methods in Physics Research Section B: Beam Interactions with Materials and Atoms, **93** (1994) 195-202.

[Blo33] F. Bloch, Zur Bremsung rasch bewegter Teilchen beim Durchgang durch Materie. Ann. Phys. Leipzig **16** (1933) 285.

[Bon71] E. Bonderup, P. Hvelplund, Stopping power and energy straggling for swift protons, Physical Review **A 4** (1971) 562-569.

[Bra05] W. H. Bragg and R. Kleeman, XXXIX. On the α particles of radium, and their loss of range in passing through various atoms and molecules, The London, Edinburgh, and Dublin Philosophical Magazine and Journal of Science , **10** (1905) 318-340.

[Car82] G. Carter, and W. A. Grant, Amorphisation of solids by ion implantation, Nuclear Instruments and Methods in Physics Research **199** (1982) 17-35.

[Chu78] W.K. Chu, J.W. Mayer, M. A. Nicolet, Backscattering spectroscopy, Academic Press, New York, (1978).

[Fri09] E. Friedland, J. B. Malherbe, N. G. van der Berg, T. Hlatshwayo, A. J. Botha, E. Wendler and W. Wesch, Study of silver diffusion in silicon carbide. J. Nucl. Mater. **389** (2009) 326-331.

[Fri11] E. Friedland, N. G. van der Berg, J. B. Malherbe, J. J. Hancke, J. R. N. Barry, E. Wendler and W. Wesch, Investigation of silver and iodine transport through silicon carbide layers prepared for nuclear fuel element cladding. J. Nucl. Mater. **410** (2011) 24-31.

[Fri13] E. Friedland, T. Hlatshwayo and N van der Berg, Influence of radiation damage on diffusion of fission products in silicon carbide. Phys. Stat. Solidi **C 10** (2013) 208-215.

[Jah81] F. Jahnel F, H. Ryssel H, G. Prinke G, K. Hoffmann K, K. Müller K, J. Biersack J, R. Henkelmann, Description of arsenic and boron profiles implanted in SiO2, Si3N4 and Si using Pearson distributions with four moments, Nuclear Instruments and Methods **182** (1981) 223-229.

[Kam84] E. Kamaratos, The mean excitation energy for stopping power I, the Bragg rule, and chemical and phase effects. Application of a statistical treatment to the determination of I for chemically bound particles. Chem. Rev. 84 (1984) 561-576.

[Lin53] J. Lindhard, M. Scharff and K. Dan. Vidensk. Selsk. Mat. Fys. Medd. **33** (1953).

[Mal13] J.B. Malherbe, Topical Review: Diffusion of fission products and radiation damage in SiC, J. Phys. D Appl. Phys. **46** (2013) 473001.

[May77] J.W. Mayer, E. Rimini, Ion beam handbook for material analysis, Academic Press, New York, (1977).

[McH93] C. J. McHargue and J. M. Williams, Ion implantation effects in silicon carbide, Nuclear Instruments and Methods in Physics Research Section B: Beam Interactions with Materials and Atoms, 80 (1993) 889-894.

[Nas14] M. Nastasi, J. Mayer, and Y. Wang, Ion Beam Analysis, Fundamentals and Applications, CRC Press, London, (2014).

[Sig14] P. Sigmund, Particle penetration and radiation effects, Springer series in solid-state sciences, vol. 179. Springer Berlin, (2014).

[Sri12] J. Ziegler, SRIM 2012 computer code, (2012). www.srim.org.

[Tes95] J. R. Tesmen and M. Nastasi, Handbook of modern ion beam materials analysis. MRS, Pittsburgh, USA, (1995).

[Tow94] P.D. Townsend, P.J. Chandler, L. Zhang, Optical effects of ion implantation, Cambridge University Press, New York, (1994).

[Wes96] W. Wesch, Silicon carbide: synthesis and processing. Nucl. Instr. Methods. Phys. Res. **B 116** (1996) 305-321.

[Wil86] J. S. Williams, Materials modification with ion beams, Reports on Progress in Physics, **49** (1986) 491.

[Zie85b] J. F. Ziegler, J. P. Biersack and Y. Littmark, The Stopping and Range of Ions in Solids, Pergamum Press, (1985).

[Zie88] J. Ziegler, Ion implantation science and technology. 2nd edition Academic press, New York, (1988).

CHAPTER 4

ANALYTICAL TECHNIQUES

In this study, the migration behaviour of Se ions implanted into polycrystalline SiC was investigated using Rutherford backscattering spectrometry (RBS), scanning electron microscopy (SEM) and Raman spectroscopy. This chapter discusses analytical techniques to show how they combine in characterizing samples.

4.1 Rutherford Backscattering Spectrometry

Rutherford backscattering spectrometry (RBS) is a well-established and conceptually simple analytical tool, based on an analysis of the energy of backscattered charged particles, it can provide direct quantitative information about the formation of thin films. RBS relies on detecting particles (helium ions (He^+) in this study) that are elastically backscattered by solid target atoms. A mono- energy beam of ions in the MeV range (1.4 and 1.6 MeV using a Van de Graaff accelerator in our case) is generated by an accelerator and then directed to the target sample in the scattering chamber. The energy of the backscattered ions from the target atoms are measured by a surface barrier detector placed at a scattering angle of usually 165°. The backscattered energy is uniquely associated with the mass of the target atom that has collided with, through the classical principles of energy and conservation of momentum, viz., the target atom can be identified from the backscattered energy of ions if the incident energy and the scattering angle are accurately known [Kui90].

4.1.1 Rutherford Backscattering Spectrometry Components

Rutherford backscattering spectrometry generally includes three basic components: An ion source, an accelerator to accelerate ions to high energy and an energy sensitive detector, typically a solid-state detector to record the energy of the backscattered ions.

In this study, radio-frequency source (RF) was used to produce the alpha particles (He^+ ions) produced and then accelerated to high energies by a large potential difference towards an accelerator. These processes are performed by a Van de Graaff accelerator, which uses principles that were developed at the beginning of the 20th century [Gra31].

This work was done using the Van de Graaff accelerator at the University of Pretoria. In this accelerator, a high potential difference is created and maintained on a smooth conducting surface. The ion beam was produced by the ion source, which is stationed in the high-voltage terminal via applying a dipole magnet deflection as mass and charge state. It was then deflected into the beamline and forwarded directly to the target chamber. The maximum voltage of accelerator is 2.7 MeV, but 1.4 MeV and 1.6 MeV were used in this work. A schematic diagrams of Van de Graaff accelerator and radio-frequency ion source are illustrated in Fig.4.1 (a) and (b), respectively.

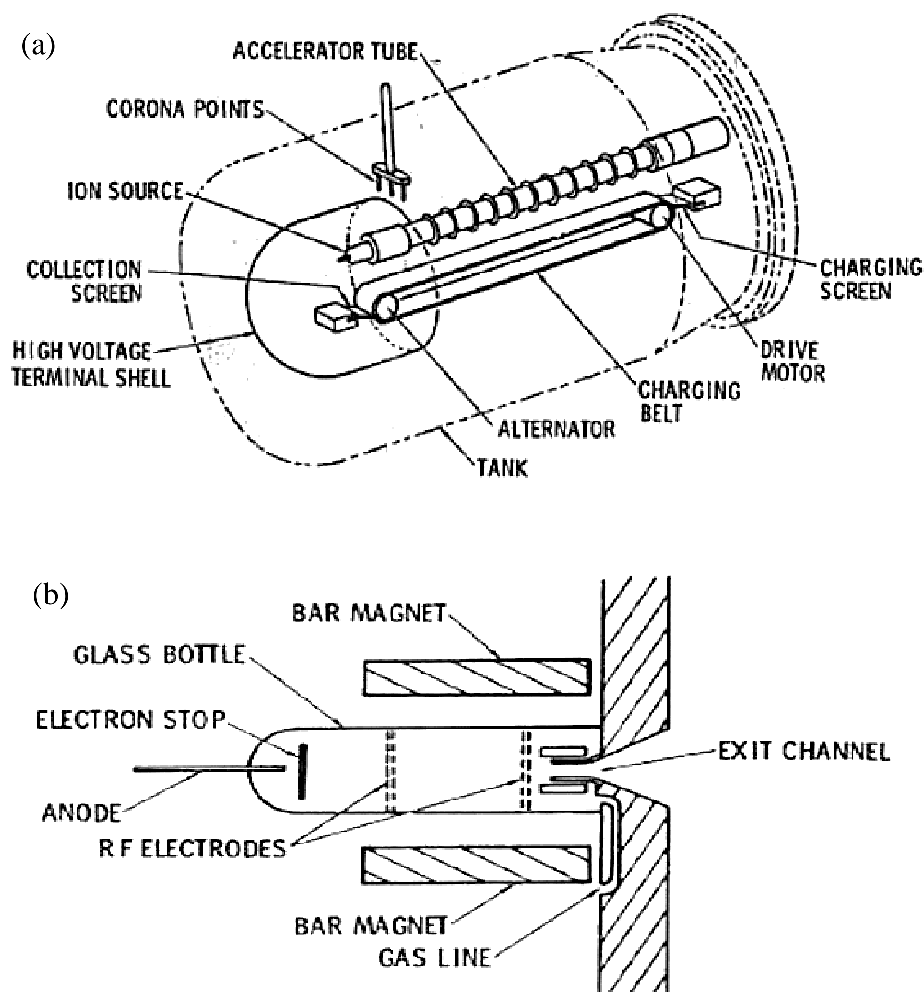

Fig. 4.1: Schematic diagram of a Van der Graaff accelerator (a) and a radio-frequency ion source ion source (b). Taken from [Chu78]

In normal operation, the accelerator tube is highly evacuated to pressures of 10^{-8} mbar to reduce collisions between the accelerated ions and the molecules. The high voltage terminal shell and the accelerating tube are covered by a tank. Fig. 4.2 shows the RBS set-up at the University of Pretoria, which consists of accelerator tank, analysing magnet, beamlines and the scattering chamber. The tank is first evacuated and filled with a mixture of N_2 and CO_2 gases to prevent sparking of the high voltage to the terminal that is at ground potential [Chu78] [Gei13]. The dipole magnet (deflecting magnet) is an energy and mass separator, and its function is to deflect the beam into either line 1 or line 2. Line 1 contains a chamber designed to operate below room temperature, while line 2 operate at room temperature. The latter was used in this research. A set of horizontal and vertical slits in line 2 guides the beam into the analyzing chamber. These slits also product a mono-ion beam by allowing ions at particular energy to pass through as already determined. Helium ion beams were used in our investigations.

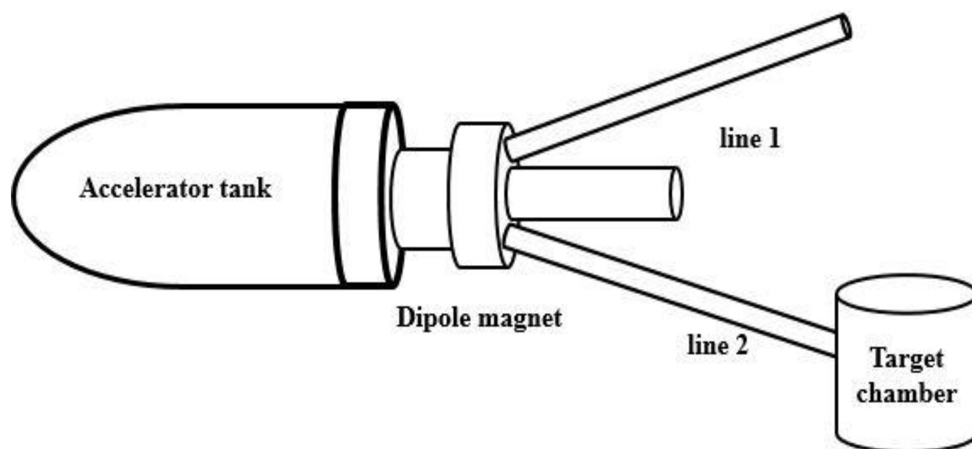

Fig. 4.2: Schematic diagram showing of RBS set-up at the University of Pretoria

Scattering chamber consists of: A stage where the target is positioned. This stage is connected to a three-axis goniometer for controlled rotating of the target. A collimator is used to form the beam into a specific size before interaction with the target as are shown in Fig.4.3. A mechanical pump is used to evacuate the chamber to lower pressures of 10^{-2} mbar, which is the starting pressure for the turbo-molecular pump. A turbo pump is then used to reduce the pressure of about 10^{-6} mbar. The secondary electrons, which lead to counterfeit the measurements, are suppressed by applying a negative voltage of approximately 200 V connected to electrode in the form of a ring in front of the target sample.

During analyses, the beam current is kept below 15 nA to avoid heating of the sample and other the most important factors as dead time, pile-up and ballistic deficit. These factors influence the RBS measurement during detecting backscattered ions. Pile-up is the distortion in the measured distribution, which occurs when there is a significant probability that more than one ion will arrive within the detector response time. In such a case, two events may be recorded as one event, which leads to falsification of measurements. The dead time is the interval of time after each event during which the counting system is unable to record another event. The charge collection times and the rise time of the output pulse are controlled to be constant to avoid the ballistic deficit effect.

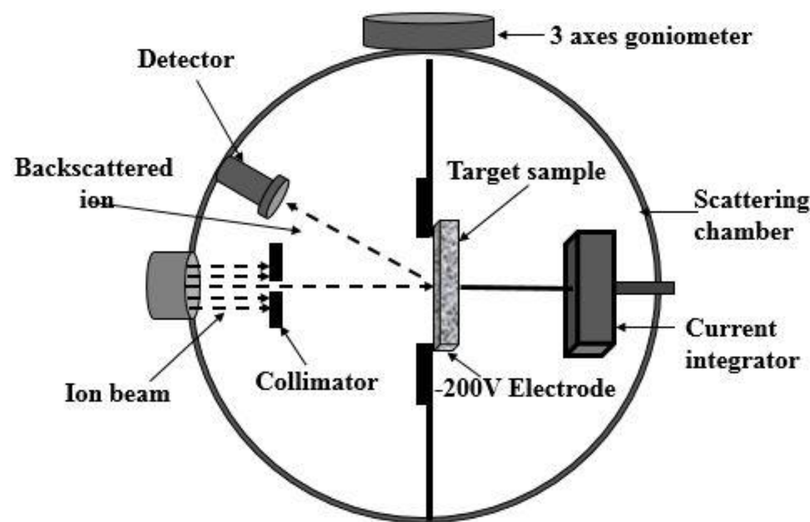

Fig. 4.3: Schematic diagram showing the scattering chamber and its components.

4.1.2 The Detector and Data Acquisition Systems

The backscattered particles from the target are analyzed by energy sensitive detector at a given angle, typically a solid-state detector at an angle of 100-170° depending on the specific analysis as shown in Fig.4.4. The Si-surface-barrier-solid state detector operating with a reverse bias of 40 V is used at the University of Pretoria. The detector is positioned at a backscattered angle of 165°with respect to the incident ion beam.

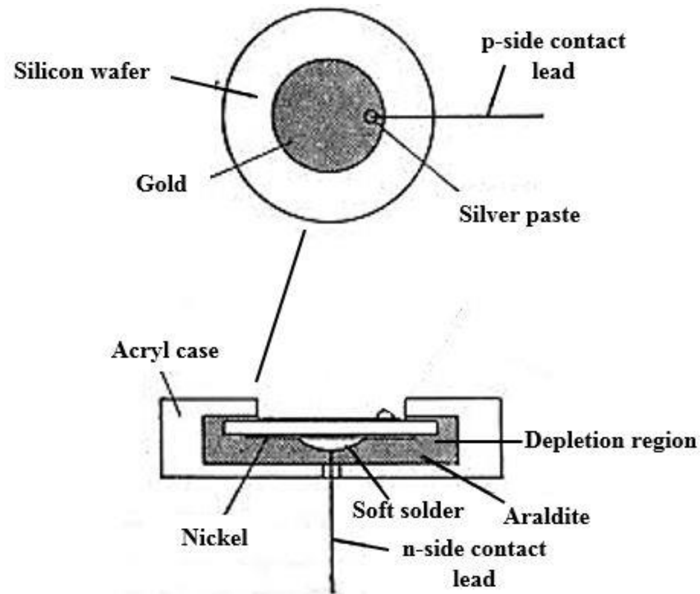

Fig. 4.4: Schematic diagram of a gold-surface barrier nuclear particle detector. Taken from [Got64].

When a backscattered ion passes through the depletion layer along the detector surface, electron-hole pairs will be created. A 40 V reverse voltage is applied to detect these electron-hole pairs. The detector output is then connected directly to the charge sensitive preamplifier as illustrated in Fig. 4.5. The primary function of a preamplifier is to extract the voltage signal from the detector, which is proportional to the backscattered ion energy. The multi-channel analyzer (MCA) is then used to digitize the amplitude of the incoming voltage signal by an analogue to digital converter (ADC). The digitized data is then stored and presented on in the computer screen in XY plane, based on channel number and counts, which correspond to the backscattered energy and concentration of ions, respectively.

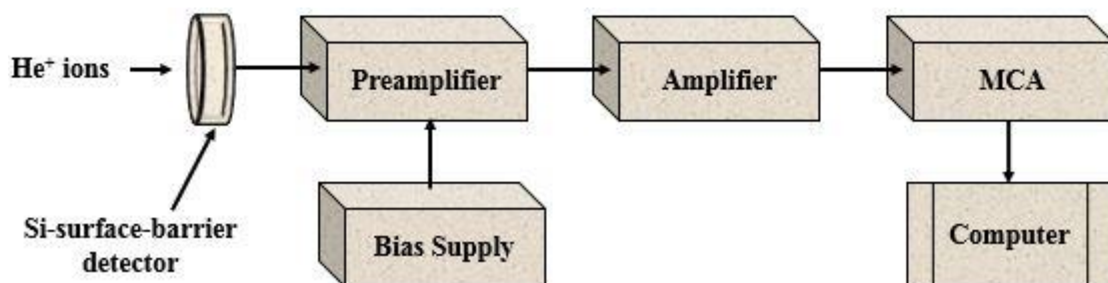

Fig. 4.5: Schematic view of a the detector and data acquisition systems

4.1.3 RBS as Materials Analysis Method and its Basic Physical Concepts

Rutherford Backscattering Spectrometry (RBS) is one of the most used nuclear methods for analyzing the near-surface layer of solids. RBS determines the quantity of the composition of a material and depth profiling of thin films, as well as individual profiles, which are specific elements. It's a non-destructive analysis with a good depth resolution of several nm and extremely sensitive to heavy elements of the order of parts-per-million (ppm) [May03]. This analysis is based on the measure of an energy of backscattered ion beam impinging on a target. In RBS, during the penetration of ions into a given material, lose their energy, if energy loss per unit distance is known, the spectrum can be converted a depth profile. It is important to understand the following basic concepts [Chu12].

- Transferring energy from an energetic ion to a target nucleus via an elastic two-body collision. This process introduces the concept of kinematic factor and to the possibility of mass perception.
- The probability of occurrence of a two-body collision is quantified by scattering cross-section.
- Average energy loss of an energetic ion travelling through a material target. This process introduces the concept of stopping cross-section
- Statistical fluctuations in energy loss of an energetic ion travelling through a material target. This process introduces the concept of energy straggling.

4.1.3.1 Kinematic Factor (K)

The kinematic factor (k) is the ratio of the backscattered and incident ion energies, which can be derived from the conservation of energy and momentum, assuming an elastic collision [Chu78]. The energy after scattering is measured only by the masses of the incident particle, target atom and the scattering angle [Alf07].

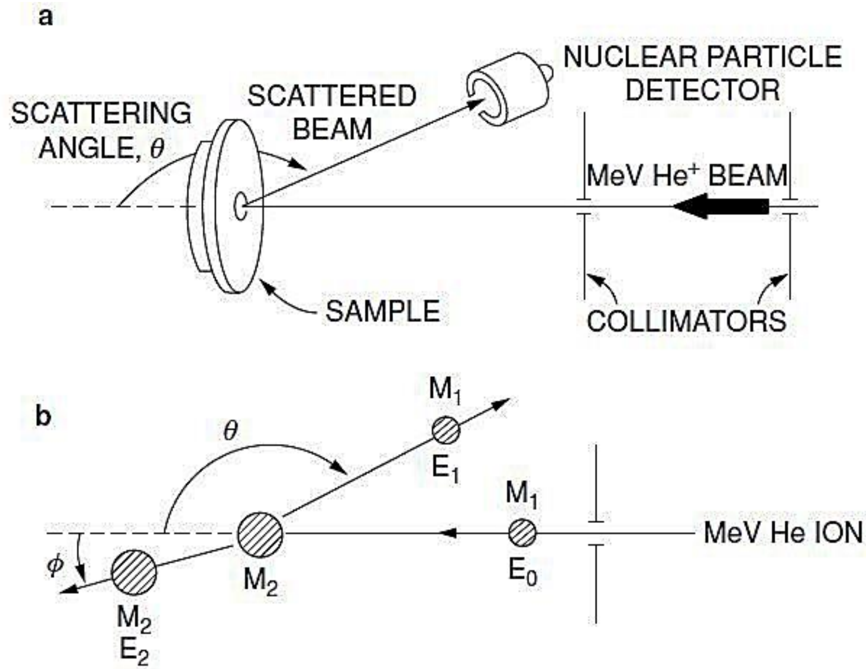

Fig. 4.6: Schematic diagram showing the scattering process between energetic ion and target atom. Taken from [Alf07].

When a target is bombarded with projectiles (M_1) of a given incidence energy (E_o) and an initial velocity v_o. As a projectile collides with a stationary target atom (M_2), the projectile backscatters with an energy E_1 and a velocity v_1 and the stationary target atom recoils with an energy E_2 and a velocity v_2 as shown in Fig 4.6. The kinematic factor (K) can be calculated using the conservation of energy and momentum as [Chu78][Tes95]:

$$K = \frac{E_1}{E_0} = \left[\frac{M_1 \cos\theta \pm (M_2^2 - M_1^2 \sin^2\theta)^{\frac{1}{2}}}{M_1 + M_2}\right]^2 \quad (4.1)$$

where θ is the scattering angle. For a fixed θ, K depends only on the mass ratio M1/M2. When $M_1 < M_2$ only the positive sign is valid in the equation above, while for $M_1 > M_2$ the equation has two solutions, and the maximum possible scattering angle is expressed as follows:

$$\theta_{max} = arc \sin\left(\frac{M_2}{M_1}\right) \quad (4.2)$$

Overall, the RBS is widely used to determine the sample components, as the incident ions with the same energy and angle will backscatter from different masses of the sample atoms with

different energies. If the energy of the incident beam is known, then the backscattered particle's energy can be identified using the kinematic factor. The kinematic factor also allows us to calibrate the RBS spectrum. It can also be used to identify the mass of an unknown target atom from measured the energy of the backscattered particle [Chu78]. The kinematic factor increases with an increase in the mass of the scattering atom, but it reaches constant values for very heavy elements, making their identification more difficult [Duc16].

4.1.4 Depth Profiling

When accelerated ions hit a solid target material, some ions backscatter from the surface, and others penetrate the sample and lose their energy due to the interaction with the target atoms, as implied by Fig. 4.7. It is necessary to point out that energy loss occurs during penetration of the target and on their way back to the surface. Fig. 4.7 shows α-particles bombardment of the target atom with an incident energy E_o. The ion that backscattered at the surface has an energy of KE_o while the one that at depth x from the surface before backscattering has an energy E (which is less than E_o because it lost energy during penetration) and has energy KE after backscattering. Thus, the energy loss is calculated from the energy difference between alpha particles scattered at the surface and those scattered at depth *x*, as follows [Chu78][Tes95]:

$$\Delta E = KE_0 - E_1 = [S]x \qquad (4.3)$$

where $[S]$ is the energy loss factor, it can be derived by assuming that the energy loss (dE/dx) is constant along the inward and outward paths as is shown in the equation below:

$$[S] = \left[\left(\frac{K}{\cos\theta_1} \frac{dE}{dx} \right)_{in} + \left(\frac{1}{\cos\theta_2} \frac{dE}{dx} \right)_{out} \right] \qquad (4.4)$$

where in and out indicate the constant values of energy loss along the inward and outward paths, respectively.

Equation (4.3) can be rewritten as:

$$\Delta E = \left[\left(\frac{K}{\cos\theta_1} \frac{dE}{dx} \right)_{in} + \left(\frac{1}{\cos\theta_2} \frac{dE}{dx} \right)_{out} \right] x \qquad (4.5)$$

The energy loss for the compound material can be calculated using Bragg's rule of the linear additivity of the stopping cross sections. For a compound target consisting of two elements A_mB_n as in our case (SiC), the total energy loss of a particle at depth x is obtained by:

$$\Delta E = [S]^{A_mB_n} x = \frac{m}{m+n}[S]A^{A_mB_n}\, x + \frac{n}{n+m}[S]B^{A_mB_n}\, x \tag{4.6}$$

From the above equation, the energy loss for element A:

$$\Delta E_A = [S]A^{A_mB_n}\, x = \left[\left(\frac{K_A}{\cos\theta_1}\frac{dE}{dx}\right)_{in} + \left(\frac{1}{\cos\theta_2}\frac{dE}{dx}\right)_{out}\right] x \tag{4.7}$$

And the energy loss for element B:

$$\Delta E_B = [S]B^{A_mB_n}\, x = \left[\left(\frac{K_B}{\cos\theta_1}\frac{dE}{dx}\right)_{in} + \left(\frac{1}{\cos\theta_2}\frac{dE}{dx}\right)_{out}\right] x \tag{4.8}$$

where K_A and K_B are the kinematic factors of elements A and B, and m and n are the relative molar fractions of A and B, respectively.

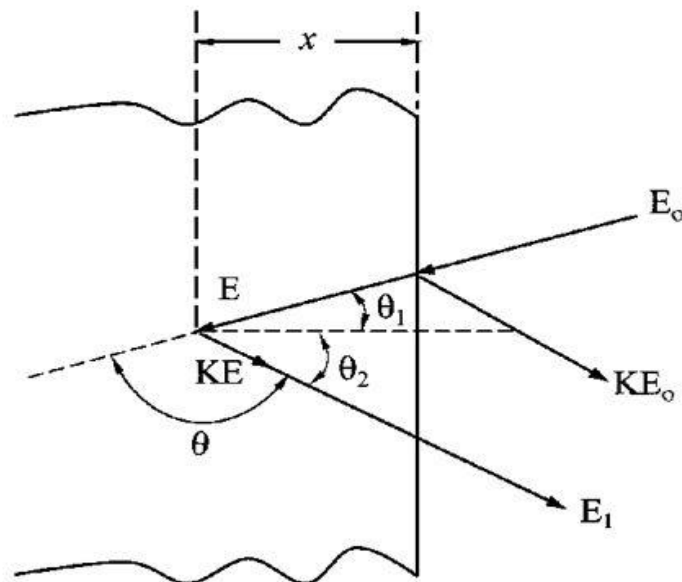

Fig. 4.7: A schematic diagram representing the backscattering events and energy loss at a depth x from the target surface. Redrawn from [Chu78].

4.1.5 Differential Cross section

The probability of a backscattering event can be described by the differential scattering cross-section $(d\sigma/d\Omega)$ of backscattering an incoming particle scattered into a particular solid angle $(d\Omega)$ as shown in equation (4.9) [Chu78] [Gro84]. The cross-section is the number of particles scattered through a unit solid angle per number of incoming particles per unit area

$$\frac{d\sigma}{d\Omega} = \left(\frac{Z_1 Z_2 e^2}{4E_o}\right) \frac{4\left(\sqrt{M_2^2 - M_1^2 \sin^2\theta} + M_2 \cos\theta\right)^2}{M_2 \sin^4\theta \sqrt{M_2^2 - M_1^2 \sin^2\theta}} \qquad (4.9)$$

Where Z_1 and Z_2 are the atomic numbers of the energetic ion and target, M_1 and M_2 are atomic mass of the energetic ion and target respectively, E_o is the energy of incident ion, e is the electron charge and θ is the backscattering angle.

From the above equation, the differential scattering cross-section is proportional to the atomic masses, which indicates backscattering spectrometry is more sensitive to elements with a greater mass than those with a smaller mass. We also conclude that the backscattering yield is higher for low energy ions compared to high energy ions, because $(d\sigma/d\Omega)$ is inversely proportional to the energy of the projectile before scattering (E_o). The total number of detected particles is defined by:

$$Y = \sigma \Omega Q N \qquad (4.10)$$

where σ is the differential cross section, Ω is the solid angle of the detector, Q is the total number of incident particles in the beam and N is the number of target atom per unit area. If σ, Ω, and Q are known, the number of atoms per unit area of the target atom can be calculated, and so the results can be well-determined.

4.2 Raman Spectroscopy

Raman spectroscopy is a form of vibrational technique based on the inelastic scattering of monochromatic light beam. Inelastic scattering occurs due to the interaction of monochromatic light with a sample, which causes a change in the photon frequencies. When the photons of the laser light hit the sample, the atoms absorb them and are then reemitted at different frequencies. These frequencies shift up or down compared to the original ones, which is termed vibrational Raman spectroscopy. The Raman shifts are usually in wavenumbers that deal with inverse centimeters (cm^{-1}). The vibrational Raman spectrum is used as chemical fingerprints to identify

molecules. In this study, Raman spectroscopy was used to monitor the SiC structure before and after ion implantation and as well as after each step of heat treatment.

4.2.1 The main components of the Raman spectrometer

A typical Raman spectroscopy consists of the following basic components as shown in Fig. 4.8 [Aga95]: (1) A source of monochromatic light an excitation source, usually a laser in visible wavenumber (2) An optical system to illuminate the sample and collect the scattered light (3) a monochromatic and 4) a signal processing unit consisting of a detector and a data processing system.

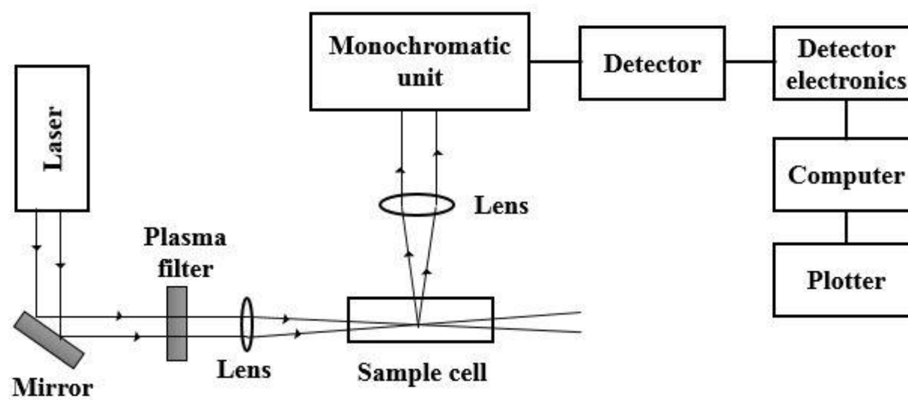

Fig. 4.8: A schematic diagram representing the components of Raman spectroscopy. Redrawn from [Aga95]

Laser light is focused on the sample with help of a mirror and lens as illustrated in Fig. 4.8. The light interacts with the sample and produces scattered light that conveys information on the vibrational mode energies of molecules [Rao14]. The scattered light is focused with a lens and sent through the monochromatic. The monochromatic is used to selectively reject Rayleigh scattering whilst allowing Raman scattering [Aga95]. Sometimes more than one monochromatic is required to obtain high resolution and/or better rejection of the Rayleigh line. The light exiting the monochromator is focused on the photosensitive surface of the detector. The detector converts the optical signal to an electrical signal and then is directed to detector electronics for further processing. The electrical signal is sent to the scanning monochromator, which measures the light intensity at various frequencies. Finally, data is stored in a computer system in a format that can be viewed and manipulated on a plotter.

4.2.2 Fundamental Principles of Raman Spectroscopy

There are three different scenarios for how a photon can be re-emitted after its energy has been absorbed by the molecule's electron as shown in Fig. 4.9: (1) Rayleigh scatter, (2) Stokes Raman scatter, and (3) Anti-Stokes Raman scatter [Loh17].

- If the electron falls down to the original ground state, which indicates no change in energy, so the emitted photon has the same original wavelength. This is known as Rayleigh or elastic scattering.
- If the excited electron falls down to a vibrational level, not at the ground level, which indicates energy loss (since some energy is absorbed by the molecule), therefore the emitted photon has a higher wavelength than the incident photon. This is one of two types of Raman scattering called Stokes scattered photon.
- When a vibrational level electron is excited to a virtual level with higher energy, it falls down to the ground level, emitting a photon with lower energy than the incident photon energy before the interaction. This type of Raman scattering called Anti-Stokes scattered photon.

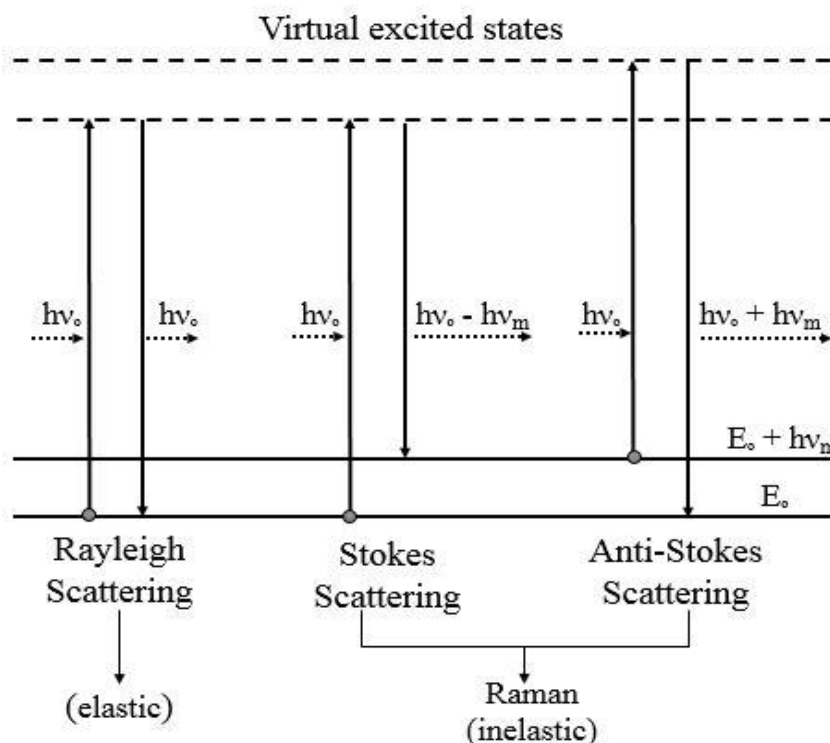

Fig. 4.9: Schematic diagram showing the Rayleigh scatter, Stokes Raman scatter and Anti-Stokes Raman scatter.

4.2.3 Theory of Raman Scattering

In the Raman scattering process, when incident photons interact with target molecules, each molecule faces a varying electric field. Hence, the electron cloud and nuclei become polarized leading to an induced dipole moment. The polarization induced (P) is directly proportional to the applied electric field (E) as [Aru08].

$$P = \alpha E \qquad (4.11)$$

where α is the polarizability of the molecule. When photons of frequency ν_o are incident on the molecules, the magnitude of the electric field can be written as [Nak97]:

$$E = E_o \cos(2\pi\nu_o t) \qquad (4.12)$$

where $E_o$the maximum amplitude of the electric field and t is the time.
Therefore, the induced dipole moment P in equation (4.11) can be rewritten as [Nak97]:

$$P = \alpha E_o \cos(2\pi\nu_o t) \qquad (4.13)$$

In the vibrational motion of the molecule, the normal coordinate Q associated with a particular vibrational mode, Q is given by follows [Aru08]:

$$Q = Q_o \cos(2\pi\nu_m t) \qquad (4.14)$$

where Q_o is the amplitude of vibration and ν_m is the vibrational mode frequency.
The polarizability may be found using the Taylor series in the normal coordinate, as follows [Aru08]:

$$\alpha = \alpha_o + \left(\frac{\partial\alpha}{\partial Q}\right)_0 Q + \cdots \qquad (4.15)$$

Neglecting higher-order terms of the series and substituting equations (4.14) and (4.15) in equation (4.13), equation 4.14 is obtained [Aru08].

$$P = \alpha_o + \left[\left(\frac{\partial\alpha}{\partial Q}\right)_0 Q_o \cos 2\pi\nu_m t\right] E_o \cos 2\pi\nu_o t \qquad (4.16)$$

$$P = \alpha_o E_o \cos 2\pi\nu_o t + \left(\frac{\partial\alpha}{\partial Q}\right)_0 Q_o\, E_o \cos 2\pi\nu_m t\ \cos 2\pi\nu_o t$$

Using the trigonometric identity $2\cos\omega\ \cos\varphi = \cos(\omega+\varphi) + \cos(\omega-\varphi)$

The above equation can be rewritten as [Aru08]:

$$P = \alpha_o E_o \cos 2\pi\nu_o t + \frac{1}{2}\left(\frac{\partial\alpha}{\partial Q}\right)_0 Q_o E_o [\cos 2\pi(\nu_o + \nu_m)t + \cos 2\pi(\nu_o - \nu_m)t] \qquad (4.17)$$

According to this equation, the induced polarization can have three distinct frequency componentsν_o, $(\nu_o + \nu_m)$ and$(\nu_o - \nu_m)$, which represent Rayleigh scattering, Raman anti-Stokes and Raman Stokes, respectively [Aru05]. When the change in polarizability $\left(\frac{\partial\alpha}{\partial Q}\right)_0$ is zero, no Raman scattering will be not generated. This means that molecular vibration will not be Raman- active unless it leads to a change in the polarization component [Aru08].

4.3 Scanning Electron Microscopy

Scanning Electron Microscope (SEM) is a powerful magnification tool focused beam of high-energy electrons on a solid surface to obtain information about the surface topography, morphology and composition [Cho17]. This information is collected as the electron beam is scanned in a raster pattern across the sample surface to create a map of the measured property relative to the X-Y position [Awr15]. In 1935, Knoll built a first scanning microscope. But, the resolution limit was about 100 mm due to the diameter of the beam focused on the sample and the inability to use lenses to produce a precise probe [Bog07]. In 1938, von Arden introduced the underlying theoretical principles of the scanning microscope, as it currently stands. In 1942, Zworykin developed the first real SEM and he showed that secondary electrons present a topographic contrast by biasing the collector positively relative to the sample surface [Bog07]. In 1960, the secondary electron detection was significantly improved by Everhart and Thornley, who created a new detector with a positively biased grid to collect electrons [Bog07].Then the electrons are converted to light using a scintillator, and a light-pipe to transfer the light directly to a photomultiplier tube to improve the signal.

4.3.1 Main Components and Operational Systems of SEM

The main components of a typical SEM are shown in the diagram of Fig 4.10. These components consist of several operational systems [Cha13] [Haw19]:

i. Vacuum system: The SEM operates in a vacuum, which is required when using an electron beam, otherwise electrons will easily disperse or scatter via collisions with other molecules.
ii. Electron beam generation system. The function of this system is to generate the primary beam of electrons. The system is placed at the top of the microscope column as illustrated in Fig. 4.10.
iii. Electron beam processing system. The system composed of a series of electromagnetic lenses and coils positioned in the microscope column. The main function of this manipulation system is to precisely control the diameter (size), shape and position of the electron beam on the surface of the specimen.
iv. Beam specimen interaction system. This system includes the interaction of the electron beam with the sample and the types of signals that can be detected. They are usually the backscattered electrons (BSE) and the secondary electrons (SE).
v. Detection system. This system consists of several sensitive detectors, each of which is sensitive to the specific energy/particle emissions that occur on the specimen. Charge collection efficiency of a detector depends on its performance and detection geometry.
vi. Signal processing system: After generating the signal using the detection system as mentioned previously, additional electronic manipulation of the image is needed. This is done by means of the signal processing system.
vii. Display and recording system: This system is used to visualize the electronic signal through the cathode ray tube that allows the recording of results using a photographic or magnetic medium.

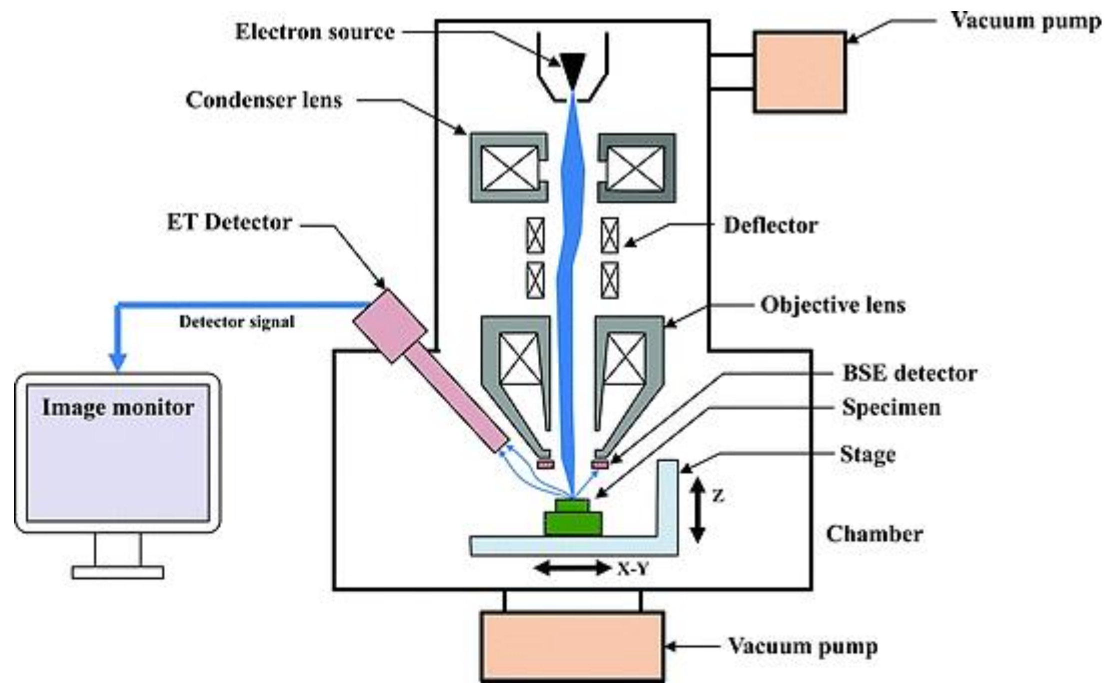

Fig. 4.10: A schematic representation of the main components of a typical SEM. Taken from [Oka18].

4.3.2 Electron-Specimen Interactions

When the sample is bombarded by the electron beam, the electrons either pass through the sample without interaction or interact with the atoms via elastic and inelastic scattering. Elastic scattering take place when there is no loss of energy of the incident electron, and vice versa in the case of inelastic scattering. Elastically scattered electrons can change directions but their wavelengths remain the same. Energetic electrons that are interacted with sample molecules can produce various signal events such as scattered electrons and secondary electrons, Auger electrons and x-rays. Fig. 4. 11 shows the signals that can be produced when the electrons beam interact with the sample, while Fig. 4. 12 illustrates the depths from which different signals are detected.

Backscattered electrons (BSE) are high energy electrons which are scattered by atoms in a specimen without losing their energy (elastically scattered) through an angle of more than 90°. Secondary electrons (SE) occur when an incoming electron passes near an atom in the sample, transfer some of its energy into a lower energy electron. This resulted in a slight energy loss and direction change in the incoming electron and the ionization of the electron in the sample atom. When the electron is ionized, leaves its atom with a kinetic energy of less than 50 eV

[Gol03]. Also, each incident electron can produce multiple secondary electrons. Thus, backscattered electrons and secondary electrons give useful signals for sample surface formation [Zho06]. Auger electrons (AE) produce as a result of the filling of the outer shell's electrons (higher energy level) inner shell holes (lower energy level) created during the emission of the secondary electrons. Auger electrons possess unique energy for each element that they emit. Also, because of their low kinetic energies, these electrons are only emitted from near the surface of the sample. Accordingly, they are used for the analysis of the chemical composition of surfaces [Zha08]. X-rays are emitted when the outer shell's electrons fall into the inner shell. These electrons fill the vacancies that arise from the emission of secondary electrons. As a result, photons - x-rays - are emitted to balance the total energy of the atom. This signal is a technique widely used to identify the type and concentration of elements in the SEM [Deh12], which is called energy dispersive x-rays spectroscopy (EDS).

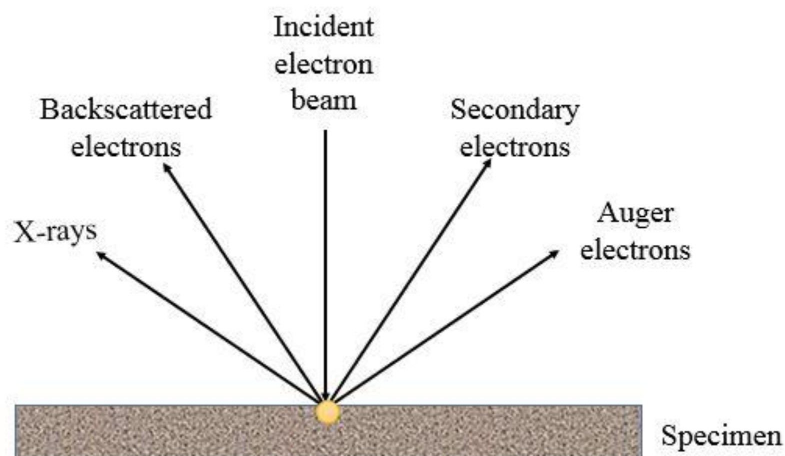

Fig. 4.11: A schematic diagram showing the signals which are emitted when an electron beam hits the specimen.

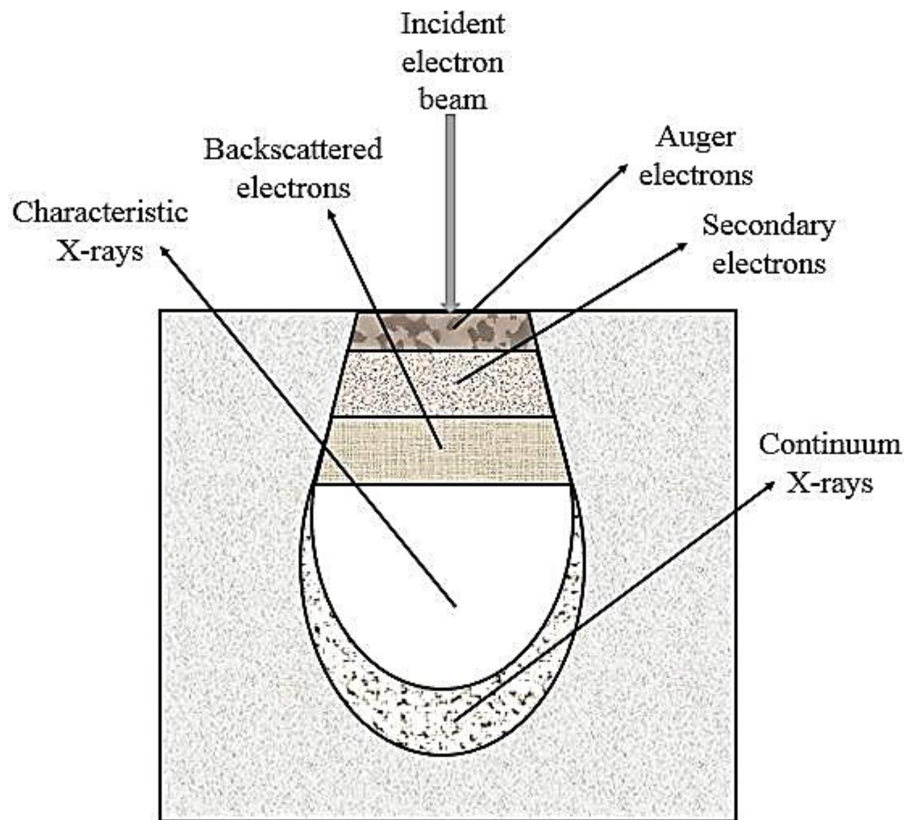

Fig. 4.12: A schematic diagram showing that the signals generated by the electron beam-specimen interaction at different depths. Redrawn from [Zho06].

The interaction volume at which all signals generated, as shown in Fig. 10, depends strongly on the following three factors:

i. The atomic number of the material being analysed: The higher atomic number material absorbs or stops more electrons, and therefore has a smaller interaction volume. By comparing different elements on the same substrate, e.g. silicon carbide as in our case, electrons absorbed or stopped by silicon are more compared to carbon.
ii. Electron energy being used: The higher energy electrons, that is, with a higher acceleration voltage penetrate further into the specimen and generate larger interaction volumes. This because the elastic scattering is inversely proportional to the square of the electron beam energy [Deh12]. Moreover, the average energy loss per distance travelled by the electron is inversely proportional to its energy [Deh12]. Therefore, electrons with a higher energy can penetrate for a greater depth before being inelastically scattered, and where are facing multiple scattering before being absorbed by the sample.

iii. Angle of incidence: Interaction volume is strongly affected by the angle of incidence the electron beam, usually 1°. The higher the angle, the smaller the interaction volume. Also, the position of the detector relative to the surface normal has a significant effect in recording the resulting signal in the reaction volume. As the detector tilts towards the surface normal, a higher signal will be recorded [Deh12].

References

[Aga95] U. P. Agarwal, R. H. Attalla, and J. S. Bond, Raman spectroscopy, Surface analysis of paper (1995) 152-181.

[Alf07] T. L. Alford, C. L. Feldman and J. W. Mayer. Fundamentals of nanoscale film analysis, Springer Science & Business Media, USA, 2007.

[Aru05] G. Aruldhas and P. Rajagopal, Modern physics, PHI Learning Pvt. Ltd., New Delhi, India, 2005.

[Aru08] G. Aruldhas, "Molecular structure and spectroscopy, Second edition, PHI Learning Pvt. Ltd., New Delhi, India, 2008.

[Awr15] J. Awrejcewicz, Dynamical Systems: Theoretical and Experimental Analysis, Springer, Poland, 2015.

[Bog07] A. Bogner, P. H. Jouneau, G. Thollet, D. Basset and C. Gauthier, A history of scanning electron microscopy developments: towards wet-STEM imaging, Micron **38** (2007) 390-401.

[Cha13] Ni. Chaoying, Scanning Electron Microscopy (SEM), Encyclopedia of Tribology, Springer, Boston MA, USA, 2013.

[Cho17] G O. P Choudhary and Priyanka, Scanning electron microscope: advantages and disadvantages in imaging components, International Journal of Current Microbiology and Applied Sciences **6** (2017) 1877-1882.

[Chu12] W.K. Chu, J. W. Mayer, M. A. Nicolet, Backscattering spectrometry, Academic Press, USA, 2012.

[Chu78] W. Chu. J. Meyer and M. Nicolet, Backscattering Spectrometry, Academic Press, NewYork, 1978.

[Deh12] G. Dehm, J. M. Howe, and J. Zweck, In-situ electron microscopy: applications in physics, chemistry and materials science, John Wiley & Sons, New Jersey, USA, 2012.

[Duc16] V. D. Duc, A. P. Kobzev, and M. Kulik, Analytical Possibilities of Rutherford Backscattering Spectrometry and Elastic Recoil Detection Analysis Methods, Communications in Physics **26** (2016) 83-92.

[Gei13] H. Geiger and E. Marsden, Phil. Mag. **25** (1913) 606.

[Gol03] J. Goldstein, D. Newbury, D. Joy, C. Lyman, P. Echlin, E. Lifshin, L. Sawyer and J. Michael, Scanning Electron Microscopy and X-Ray Microanalysis, 3rd edition, Springer, USA 2003.

[Got64] S. Gotoh, and Z. Takagi, Silicon Surface Barrier Detector, Journal of Nuclear Science and Technology **1** (1964) 311-315.

[Gra31] R.J. Van De Graaff, A 1,500,000 volt electrostatic generator, Physical Review **38** (1931) 1919-1920.

[Gro84] J. J. Grob, P. Siffert, Rutherford backscattering spectroscopy (RBS), Progress in Crystal Growth and Characterization **8** (1984) 59-106.

[Haw19] P. W. Hawkes and C. S. John, Springer Handbook of Microscopy, Springer Nature, Switzerland AG, Switzerland, 2019.

[Kui90] A. E. T. Kuiper, RBS and ERD analysis of semiconductor device materials, Surface and Interface Analysis **16** (1990) 29-35.

[Loh17] S. Lohumi, M. S. Kim, J. Qin, and B. K. Cho, Raman imaging from microscopy to macroscopy: Quality and safety control of biological materials, TrAC Trends in Analytical Chemistry **93** (2017) 183-198.

[May03] M. Mayer, Rutherford backscattering spectrometry (RBS), Nuclear Data for Science and Technology: Materials Analysis, vol. 34, 2003.

[Nak97] K. Nakamoto, Infrared and Raman Spectra of Inorganic and Coordination Compounds, 5th edition, John Wiley & Sons, New York, USA, 1997.

[Oka18] Y. Okano, Compendium of Surface and Interface Analysis, Springer, Singapore, 2018.

[Rao14] S. Rao, and K. D. Costa, Atomic Force Microscopy (AFM) in biomedical research, In Biomedical Imaging, Woodhead Publishing, 2014, USA.

[Tes95] J. R. Tesmer and M. Nastasi, Handbook of Modern Ion Beam Materials Analysis, MRS, Pittsburgh, USA, 1995.

[Zha08] S. Zhang, L. Li and A. Kumar, Materials characterization techniques, 1st edition, CRC press, Florida, USA, 2008.

[Zho06] W. Zhou, R. Apkarian, Z. L. Wang, and D Joy. Fundamentals of scanning electron microscopy (SEM), Springer, New York, NY, 2006.

CHAPTER 5

EXPERIMENTAL PROCEDURES

Polycrystalline CVD-SiC wafers from Valley Design Corporation were used in this study. These wafers were composed of mainly 3C–SiC with some traces of 6H–SiC. The as-received wafers were implanted with Se ions at RT, 350 °C and 600 °C. Then the as-implanted samples heat treated at various temperatures. The migration of implanted Se was monitored by RBS while morphological and structural evolutions were monitored by SEM and Raman spectroscopy respectively. Fig. 5.1 shows a schematic diagram of the experimental procedures in this study.

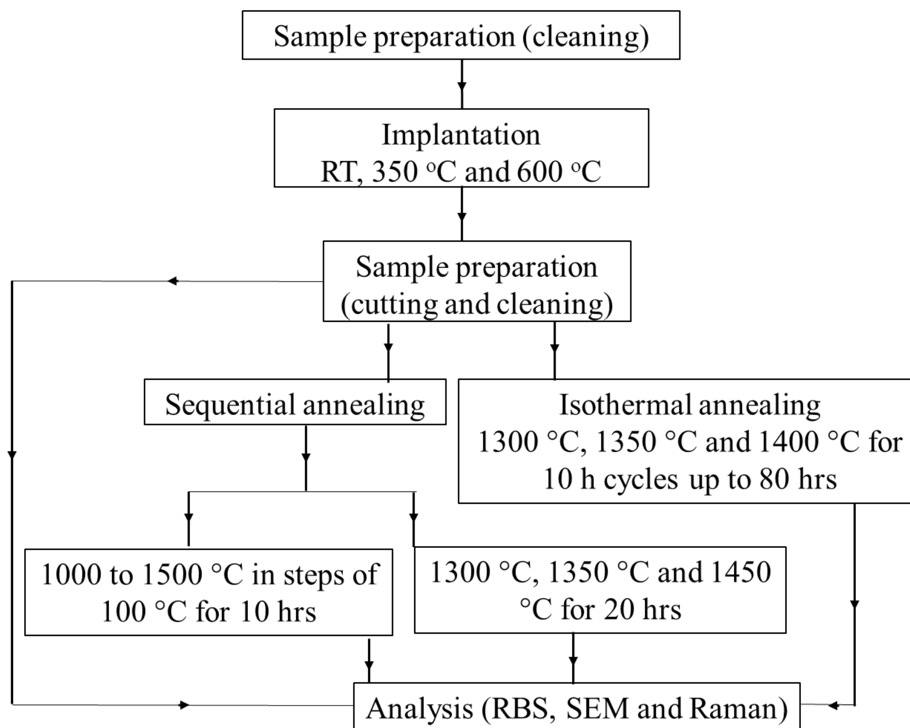

Fig. 5.1: Schematic diagram describing the experimental procedures.

5.1 Sample preparation

Before implantation, wafers were cleaned in an ultrasonic bath with alkaline soap, followed by a de-ionized water. The de-ionized water was used to remove alkaline soap. This step was repeated twice for 10 minutes. The wafers were then cleaned with methanol for five minutes to remove de-ionized water. Finally, the wafers were dried with nitrogen gas for a few minutes,

and then transferred in an oven at 50 °C for one hour to remove volatile impurities on the surfaces.

5.2 Implantation procedures

The cleaned wafers were sent to the Institut für Festkörperphysik, Friedrich-Schiller-University Jena, Germany for implantations. The implantations were carried out with ^{80}Se ions of 200 keV to a fluence of 1×10^{16} cm^{-2}. The flux was kept below 10^{13} cm^{-2}s^{-1} to minimize radiation induced heating. Implantations were performed at room temperature (RT), 350 °C and 600 °C under vacuum of about 10^{-4} Pa. To avoid channelling, implantation was performed at an angle of 7 ° relative to normal incidence. Ion beam homogeneity over the samples surfaces was achieved by the use of 2dimensional beam scanning.

After implantation, the wafers were cut into 5 mm × 5 mm using a rotary diamond saw. This size was chosen because it fits well with RBS and SEM sample holders. The samples were then cleaned with deionized water followed by methanol to remove contamination on the sample' surfaces due to the cutting process.

5.3 Annealing process

The cleaned samples were subjected to thermal annealing in vacuum using a computer-controlled Webb 77 graphite furnace - see Fig 5.2. The samples were carefully loaded onto a graphite crucible with implanted side facing up, and then placed in the oven. This was done to avoid contamination of samples during annealing. In this study, the radiation damage after implantation and their recovery were investigated using two types of annealing: sequential and isothermal annealing. To investigate the migration behaviour of Se in polycrystalline SiC, the implanted samples were subjected to sequential annealing. Then, isothermal annealing was performed at temperatures at which a change in the selenium depth profile obtained from RBS was observed. This allows us to determine the activation energy,E_a and pre-exponential factor, D_o of selenium diffusion in amorphous silicon carbide. In the sequential type, two temperature regimes were used: In the first regime, the samples were annealed at temperatures ranging from 1000 to 1500 °C in steps of 100 ° C for 10 hours cycle. Whereas in the second regime, samples were annealed at 1300 °C, 1350 °C and 1450 °C for 20 hours. After each annealing step, the oven was allowed to cool down natural to room temperature. The samples were then

extracted and analyzed using Rutherford backscattering spectrometry (RBS), Raman spectroscopy and scanning electron microscopy (SEM). In the isothermal annealing, the samples were heated at the same temperature for accumulated annealing cycle. the annealing time was incremented as follows: 10 hours, analysis 10 hours+10 hours = 20 hours, analysis, 20 hours+20 hours = 40 hours, analysis, 40 hours + 40 hours = 80 hours, analysis, etc. Samples were isothermally annealed at different temperatures 1300 °C, 1350 °C and 1400 °C.

The temperature was controlled by a Eurotherm 2704 controller. This controller is connected to a thermocouple and a pyrometer that are used as temperature sensors. The thermocouple is for measuring temperatures below 1475 °C, while the pyrometer is used above 1525 °C. The average temperature value between the thermocouple and the pyrometer was considered with an accuracy of ± 15 °C in our measurements.

In the beginning of the annealing process, the oven was evacuated to a vacuum of about 10^{-7} mbar. To reduce total pumping time and keep vacuum pressure in the range of 10^{-6} mbar. The heating rate was kept at 20 °C /min for all experiments. The oven was then degassed at 200 °C for an hour before heating up to the desired temperature (i.e. 1000 ºC as seen in Fig. 5.2 and then remained there for the set annealing time, i.e. 10 hours).In this step, the temperature overshoot of about 130 °C (200 °C to 330 °C) have been observed. This behaviour was due to the setting-up by the manufacturer, which leads to significant fluctuations in the initial current. It has also been observed that the current reaches a maximum value of about 28 A at the beginning of the heating process, and then decrease to 0 A to reduce overshooting above the set temperature (200 °C). Then, the heating element heats up to the required temperature and time duration. The current started to increase again during heating up to reach 18 A, and then dropped to 8 A during the annealing-time at the required temperature. Finally, the heating element cools down to room temperature as shown in Fig. 5.3

In cooling down, the oven was programmed to decreases to room temperature. After that, the vacuum pump was switched off. Then the vacuum was completely brought down by switching off the fore pump.

To remove the samples from the oven, the argon gas was opened into the chamber to bring the pressure to the atmospheric pressure. The samples were then extracted.

Fig. 5.2: Computer-controlled Webb 77 graphite furnace used in this research. Taken from [www1]

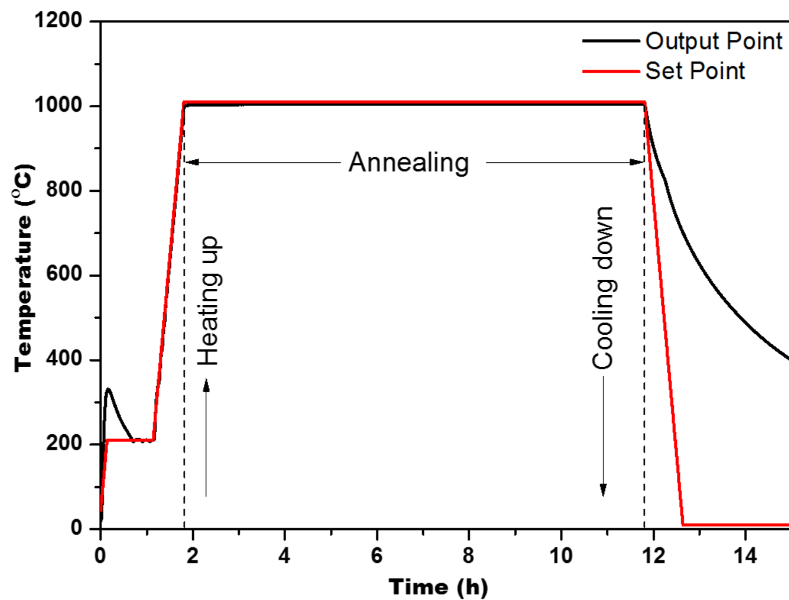

Fig. 5.3: Diagram showing the annealing process for a sample annealed at 1000 °C for 10 hours.

5.4 The basic conditions of measurement

5.4.1 Raman measurement

The microstructural changes in SiC due to the implantation and annealing were monitored by using a Jobin Yvon, Horiba$^{(C)}$ TX64000 triple Raman spectrometer. The investigations were performed in the visible region with a 514.5 nm of Ar/Kr laser lines as exciting radiation. The spot of ~2 μm^2 was used to focus the laser beam and collected by a 50 X objective. A maximum

power of 0.17 mW was kept during the measurements to avoid heating of the samples. The scanning range was 200 – 1800 cm^{-1} with a resolution of 2 cm^{-1}.

5.4.2 SEM measurement

The morphological evolution were monitored by a Zeiss Ultra 55 field emission gun scanning electron microscopy (FEG-SEM) with an in-lens detector. An accelerating voltage of 2 kV was used. The working distance was maintained in the range of 2.5 to 3.5 mm and different magnifications were used.

5.4.3 RBS measurements

The distribution of the implanted Se was monitored after each annealing step using Rutherford backscattering spectroscopy (RBS).RBS was performed at room temperature using He^+ particles at 1.6 MeV. The silicon (Si) surface barrier detector with a solid angle of 3.41 msr was used to detect the backscattered particles. The detector was positioned at a scattering angle of 165˚ while the sample tilt angle was kept at 10 ˚. The beam current was approximately 15 nA and 24 μC was collected per measurement.

The RBS spectra were converted to depth in nm using the energy loss data and density of pristine SiC (3.21 gcm^{-3}). The depth profiles were fitted to a Gaussian function to extract the projected ranges (Rp) and stragglings (ΔRp) for each sample. They were also fitted to the solution of the Fick diffusion equation for a Gaussian as-implanted profile to extract the diffusion coefficients [Mah17].

References

[www1] https://www.rdwebb.com, 14 June 2020.

[Mah17] J. B. Malherbe, P. A. Selyshchev, O. S. Odutemowo, C. C. Theron, E. G. Njoroge, D. F. Langa and T. T. Hlatshwayo, "Diffusion of a mono-energetic implanted species with a Gaussian profile, Nucl. Instruments Methods Phys. Res. Sect. B Beam Interact. with Mater. Atoms **406** (2017) 708-713.

CHAPTER 6

RESULTS AND DUSCUSSION

The effects of heat treatment on the migration behaviour of selenium implanted into polycrystalline SiC was investigated. Se ions of 200 keV were implanted into polycrystalline SiC to a fluence of 1×10^{16} cm^{-2} at room temperature (RT), 350 °C and 600 °C. The implanted samples were then subjected to both sequential and isothermal heat treatment. The migration of implanted Se was monitored by Rutherford backscattering spectrometry (RBS) while structural and morphological evolutions were monitored by Raman spectroscopy and scanning electron microscopy (SEM).

6.1 Room temperature implantation

6.1.1 Raman Results

Fig. 6.1 (a) shows the Raman spectra of pristine SiC, RT implanted and RT implanted then annealed at temperatures from 1000 to 1500°C in steps of 100°C for 10 h. The spectrum obtained from the pristine sample showed a number of Raman lines of silicon carbide, which include–the transverse optical (TO) mode splitting into two peaks at 771 and 797 cm^{-1}, the longitudinal optical (LO) mode at 966.5 cm^{-1}, a TO overtone peak at 1520 cm^{-1} and another overtone at 1714 cm^{-1}. These values are very close to those reported in references [Des16] [Nak97] [Fel68].

From spectra of the as-implanted, it is clear that the characteristic SiC Raman peaks (between 750 and 1000 cm^{-1}) disappeared (see Fig. 6.1 (b)), and three broad Raman bands appeared around 519, 880 and 1424 cm^{-1}. These broad bands are caused by the vibrations of Si-Si, Si-C and C-C bonds, respectively [Cha02]. This change in the spectrum indicates that the SiC layer is amorphized as a result of the implantation. After annealing at 1000°C, the main Raman peaks of silicon carbide reappeared-indicating the recovery of the crystal SiC structure.

The detection of defects can be monitored using the longitudinal optical (LO) Raman mode [Lit17]. In this study, the characterization of the recovery process is based on the measurements of the shift and the full width at half maximum (FWHM) of the LO mode as a function of temperature. Annealing at 1000 °C resulted in the appearance of the LO peak at 965.3 cm^{-1}, which is 1.2 cm^{-1} lower than the one of the virgin sample as can be seen in Fig. 6.2 (a). This indicates the presence of the tensile stress in bonds between atoms as a result of a change in

atomic distances [Wen12]. Further annealing shows that the LO peak shifts toward the lower wavenumbers with increasing temperature, indicating higher tensile stress. Fig. 6.2 (a) also shows that the FWHM of LO mode obtained from the sample annealed at 1000 °C (12.4 cm^{-1}) is broader in comparison with the virgin sample (9.6 cm^{-1}). The broadness of the Raman band indicates the presence of defects and a poor crystallinity [Fen16]. With increased annealing temperature, the FWHM decreased gradually and became 10.6 cm^{-1}, which is still broader than the virgin indicating that defects are still present.

For the second sequential regime, new sample implanted at room temperature was used. From the Raman spectra of the samples annealed at 1300 °C, 1350 °C and 1450 °C for 20 h (not shown), the LO mode appeared at approximately 963 cm^{-1} after annealing at 1300 °C. It can be clearly observed to shift towards a lower wavenumber with increasing temperature to approximately 962.5cm^{-1} after annealing at 1350 °C and 1450 °C as shown in Fig. 6.2 (b), which implies the presence of tensile stress in the sample. Fig. 6.2 (b) also shows that the FWHM decreased from 11.4 cm^{-1} after annealing at 1300 °C to 11.3 cm^{-1} after annealing at 1350 ºC. After annealing at 1450 °C, the FWHM became 10.5 cm^{-1}, suggesting that the sample has approximately the same degree of crystallization as the one annealed at 1500 ° C for 10 h.

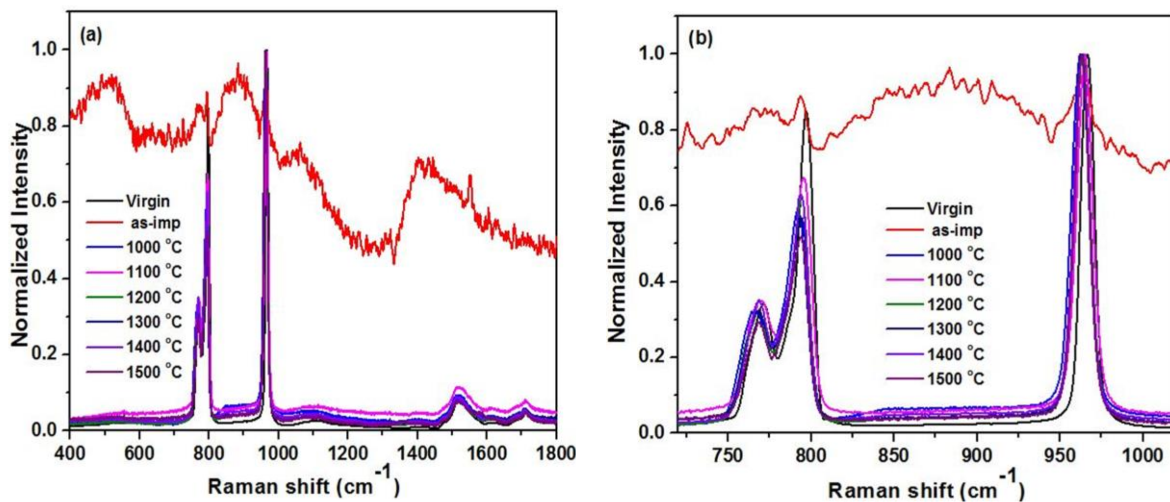

Fig. 6.1: Raman spectra of the pristine SiC after implantation and sequential annealing from 1000 to 1500 °C for 10 h.

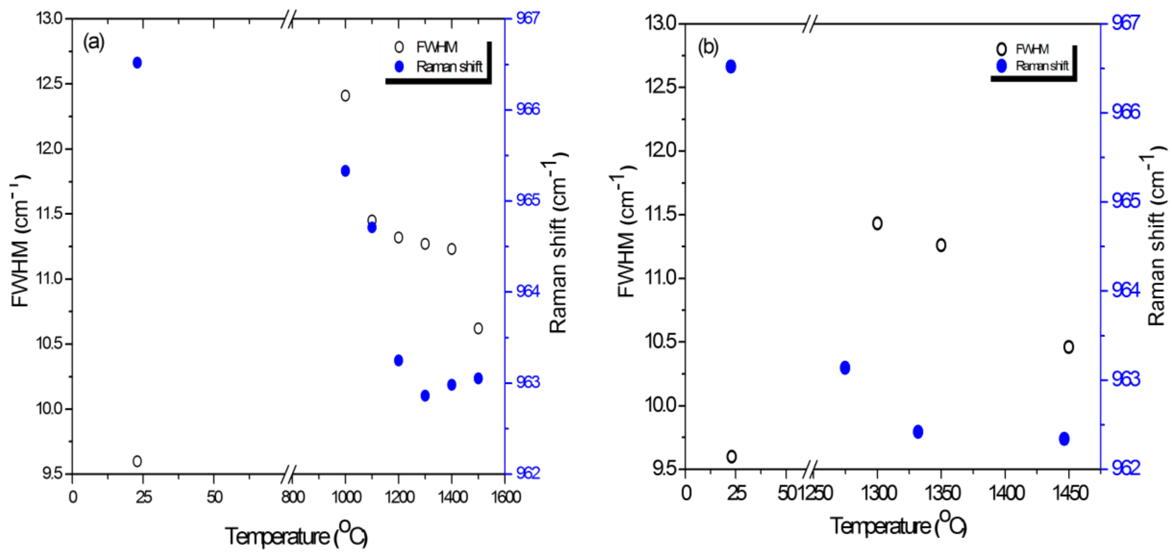

Fig. 6.2: The FWHM and Raman shift of the LO mode as function of temperature (a) after sequential annealing from 1000 to 1500 °C for 10 h, (b) after annealing at 1300 °C, 1350 °C and 1450 °C for 20 h.

Fig. 6.3 and shows the effect of isothermal treatment of the LO mode of SiC at 1300 ° C, at 1350 °C and at 1400 °C. As was pointed out earlier, this was done by annealing the implanted samples for 10 h cycles up to 80 h (80 hours for 1350 °C is not shown). The Raman spectrum of a pristine sample is included for comparison. The observations are presented in Fig. 6.4 and Fig. 6.5. Fig. 6.4 shows the relationship of LO peak intensity vs time. As the annealing cycles increased, the LO mode became more intense, indicating a decrease in crystal defects or damage concentration inside the SiC substrates [Zon18] [Sor06]. This also indicates an increase in the number of scattering molecules irradiated by the incident light, which means that the crystals have grown in size. [Zon18] [San14].

The structural evolution of SiC was quantified by the full width at half maximum (FWHM) of the LO mode. Fig. 6.5 presents the full width at half maximum (FWHM) of the LO mode. What can be clearly seen in Fig. 6.5 is a general decrease in the FWHM with increasing annealing cycles up 80 h, especially for the sample annealed at 1400 °C. The decrease in FWHM is an indication of the crystallinity, i.e. the presence of defects of any kind will shorten the phonon lifetime and thus broaden the linewidth [Zon18] [Bee08]. Therefore, the crystalline material gives sharper Raman line than the amorphous material.

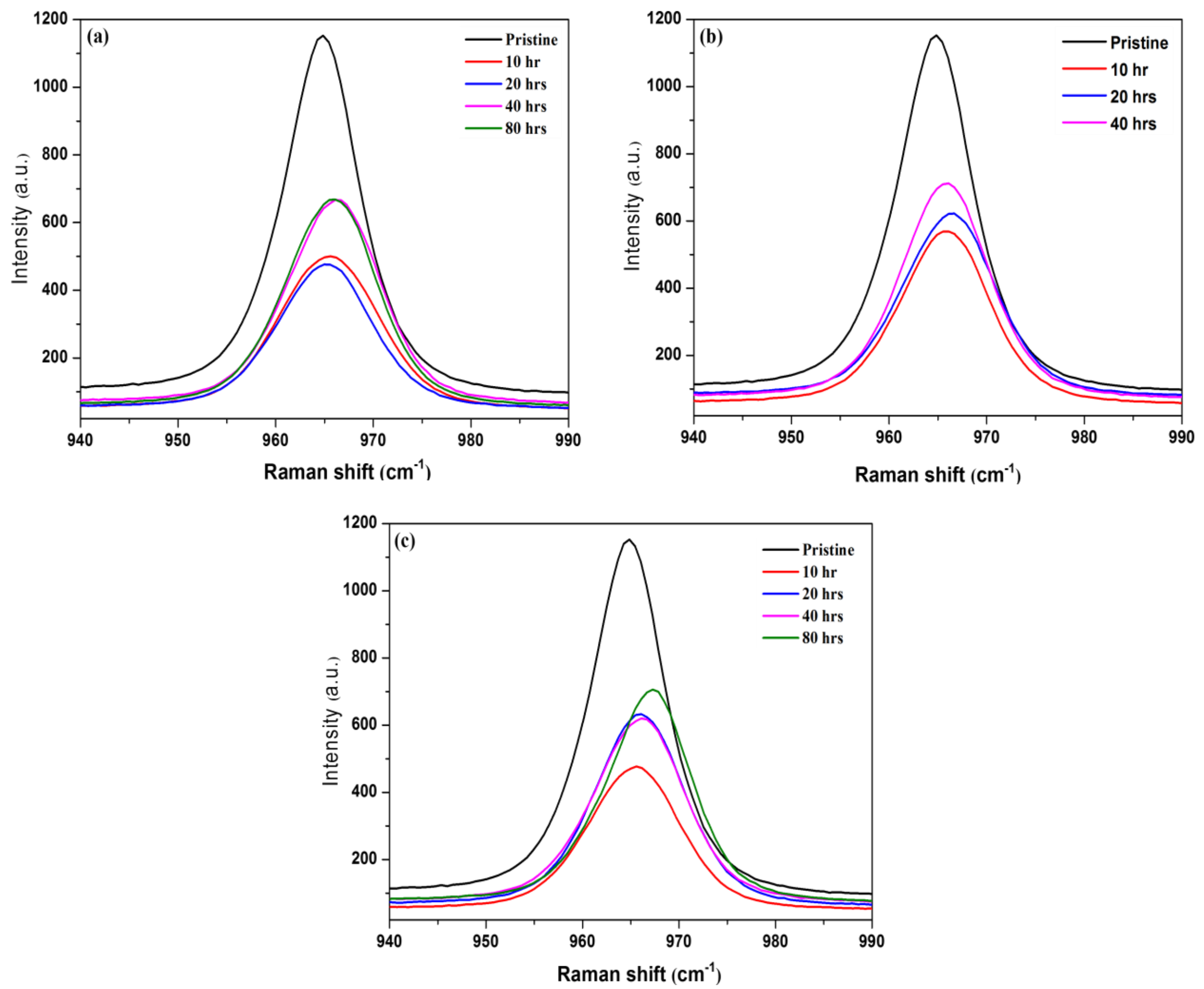

Fig. 6.3: LO modes of SiC Raman spectra of samples implanted with Se at room temperature as a function of time during isothermal annealing at temperatures of (a) 1300 °C, (b) 1350 °C and (c) 1400 °C.

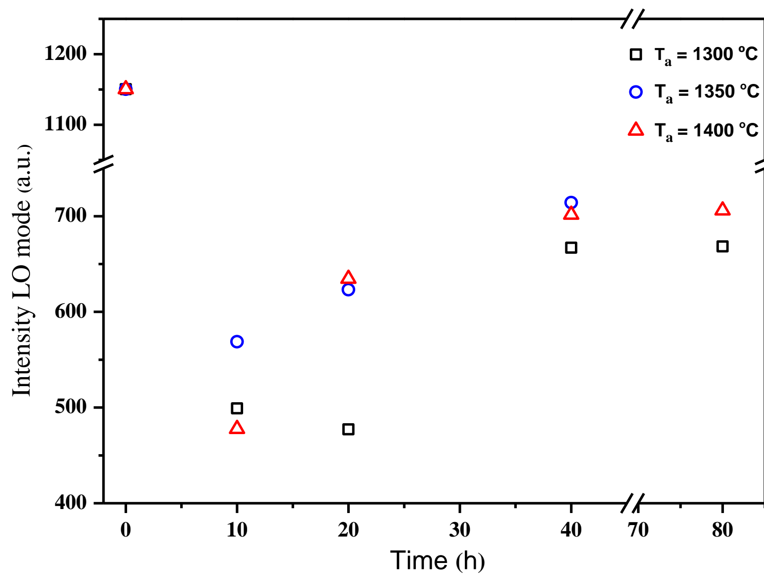

Fig. 6.4: The intensity of LO mode of SiC implanted with Se at room temperature as a function of time during isothermal annealing at different temperatures.

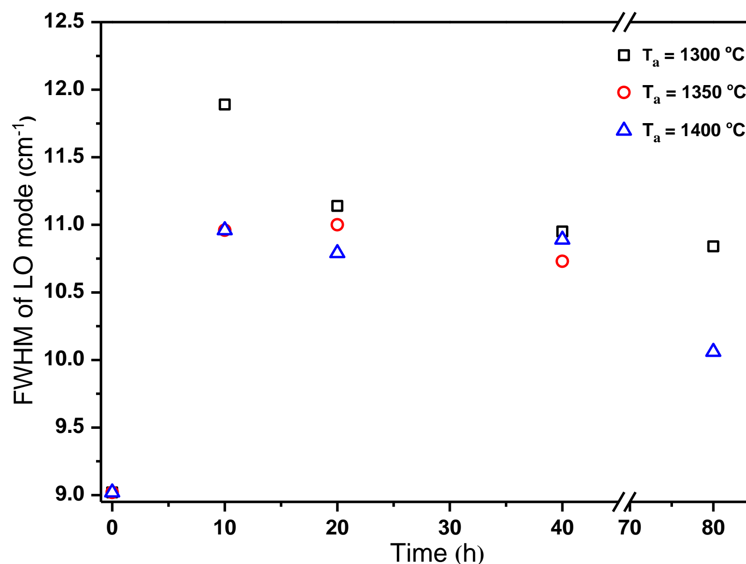

Fig. 6.5: The FWHM of LO mode of SiC implanted with Se at room temperature as a function of time during isothermal annealing at different temperatures.

The plot of the LO mode position as a function of time during isothermal annealing at different temperatures is shown in Fig. 6.6. In all samples (annealed at 1300 °C, 1350 °C and 1400 °C), the first annealing cycle resulted in the appearance of the LO mode at about 965.4 cm^{-1}, which is at higher wavenumber than in the pristine sample. This indicates the presence of the compressive stress in bonds between atoms due to a change in atomic distances. Shifting to

higher wavenumber is usually an indication of decreased length of chemical bonds, relative to their length in the unstressed crystals [Wol03]. There was no considerable change in the LO position during the second annealing cycle (20 h) in the annealed sample at 1300 °C, whereas in the other two samples (annealed at 1350 °C and 1400 °C), the LO mode shifted by 0.5 cm^{-1} to higher wavenumbers, indicating greater compressive stress. At all temperatures, the LO mode shifted to approximately 966 cm^{-1} during the third annealing cycles (40 h). No further shift was observed in the annealed sample at 1300 °C during the final annealing cycle (80 h), while Isothermal annealing at 1350 °C and 1400 °C caused further shift to higher wavenumbers at the same cycle. One important fact to note is that the resolution of the Raman spectrometer (2 cm^{-1}) [Hla17][Pri08], which is larger than most of the measurements of the shift of LO mode in SiC spectra as a function of time during isothermal annealing.

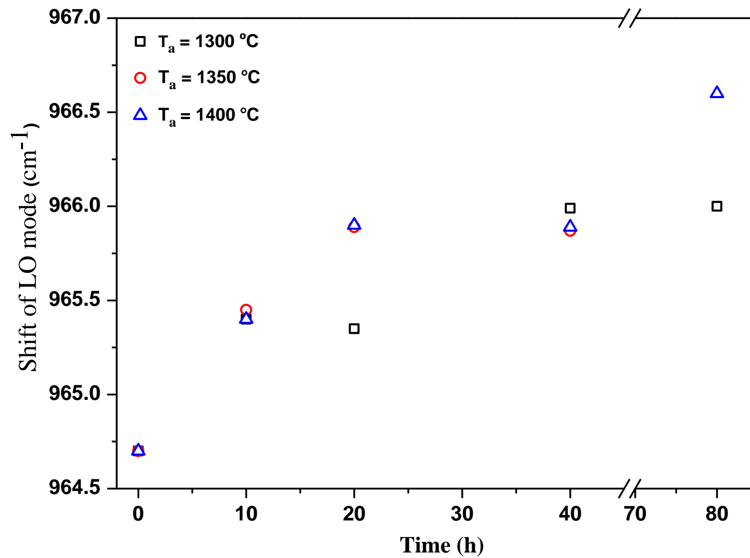

Fig. 6.6: The Raman shift of LO mode of SiC implanted with Se at room temperature as a function of time during isothermal annealing at different temperatures.

6.1.2 SEM Results

Ihe effects of implantation and annealing temperature on the surface morphology were characterized using a Scanning Electron Microscopy (SEM). The SEM micrographs of pristine, as-implanted (RT) and annealed samples at temperatures ranging from 1000 to 1500 °C in steps of 100 ° C for 10 h cycle are shown in Fig. 6.7. The surface of the pristine sample contains some polishing marks as can be seen in Fig. 6.7(a), while (b) shows that the polishing marks

became less pronounced after implantation due to the sputtering of the SiC surface by the bombarding Se ions, and the swelling of the amorphous implanted layer [Mal15]. After annealing at 1000 °C (Fig. 6.7(c)), the surface remained flat and featureless. The higher magnification inserts indicated some recrystallization. After annealing at 1300°C (Fig. 6.7(d)), the crystals became more apparent and distinct than in the sample annealed at 1000 °C. Some cavities can also be seen. The higher magnification clearly shows that some large crystals are on top of the smaller crystals, with the latter forming a kind of a substrate. The variation in the height indicates an increasing surface roughness, which is more apparent in the low magnification image. The smaller crystals increased in size after annealing at 1400°C (Fig. 6.7(e). Consequently, the distinction between large and smaller crystals became less obvious with fewer but larger pores. The uniformity of distribution in crystal size is seen after annealing at 1500°C (Fig. 6.7(f)). The pores became more prominent. These pores may explain the loss of significant amounts of the implanted Se ions at this temperature as discussed under RBS section (Fig. 6.13 and Fig. 6.14).

The SEM micrographs of samples annealed at 1300 ° C, 1350 ° C and 1450 ° C for 20 h cycle are shown in Fig. 6.8. Fig. 6.8 (a) shows that the annealing of an as-implanted sample at 1300 ℃ for 20 h led to the appearance of large crystals with a few pores. After annealing at higher temperatures (1350 and 1450 ℃), the crystals became more prominent (Fig. 6.8 (b) and (c)). The 1450 ℃ samples (Fig. 6.8 (c)) had slightly more and longer dendritic crystals.

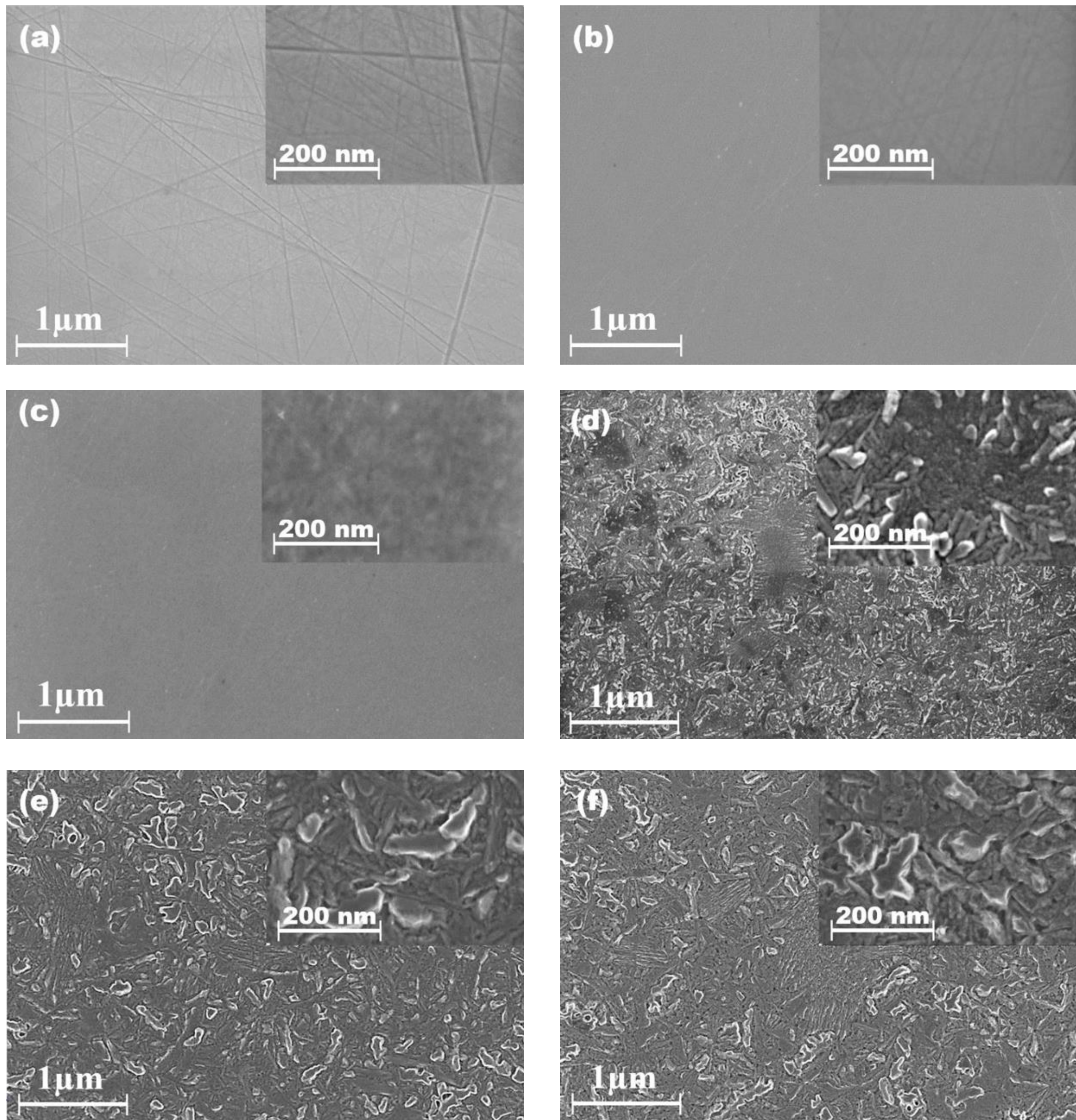

Fig. 6.7: Surface SEM micrographs of (a) Pristine poly-SiC; (b) after implantation with Se at RT; compared with surfaces after vacuum annealing at (c)1000 °C, (d) 1300 °C, (e) 1400 °C and (f) 1500°C for 10 h.

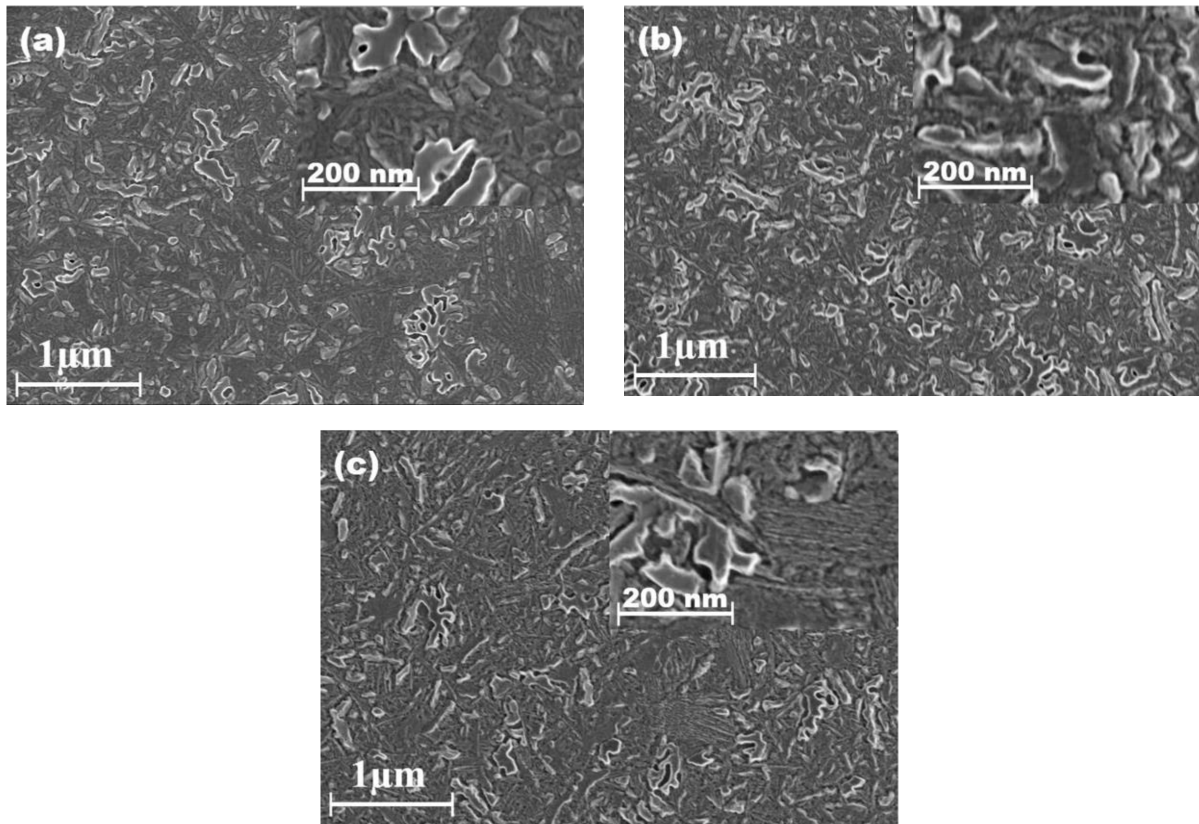

Fig. 6.8: Surface SEM micrographs of as-implanted SiC after vacuum annealing at (a) 1300 °C, (b) 1350 °C and (c) 1450 °C for 20 h.

The SEM results of the room temperature implanted samples before and after isothermal vacuum annealing at temperatures of 1300,1350 and 1400 ºC are shown if Fig 6.9,6.10 and 6.11. By comparing the surfaces of annealed samples for the same period of time, but at different temperatures, as expected, it was found that the development of surface topography increases significantly with the annealing temperature. In Fig. 6.9 (a), a SEM image of the RT implanted sample annealed at 1300 °C for 10 h showing a surface consisting of small crystals and regions devoid of features. This indicates recrystallization according to the appearance of the crystals. However, the featureless regions suggest the presence of defects. No significant morphological changes were observed during subsequent annealing cycles up to 80 h (Fig. 6.9 (b)). The annealing of as- implanted sample at 1350 °C for 10 h resulted in a distinguishable features surface with visible crystals as can be seen in Fig. 6.10 (a). The crystals increased in size with a few pores with subsequent annealing cycles (Fig. 6.10 (b)). The SEM image showed that the crystals are more prominent, as well as presence of pores and cavities after annealing at 1400 °C for 10 h (Fig. 6.11 (a)) compared to Fig. 6.10 (a). Further subsequent annealing

cycles resulted in a slight growth of the surface crystals (see Fig. 6.11 (b)). These SEM observations confirm the fact that surface development and the crystals growth are greatly affected by temperature.

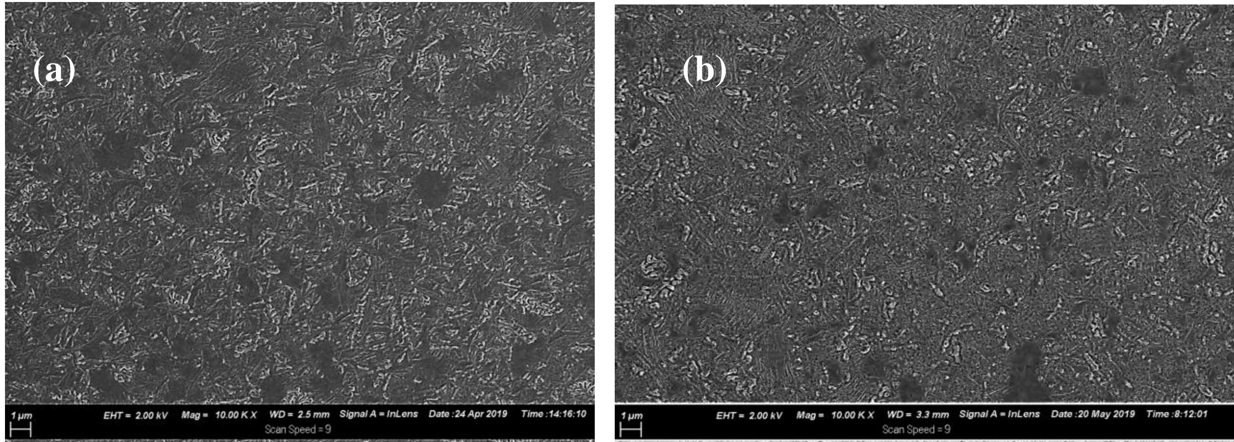

Fig. 6.9: SEM micrographs of room temperature selenium implanted SiC surfaces after vacuum annealing at 1300 °C for (a) 10 h and (b) 80 h.

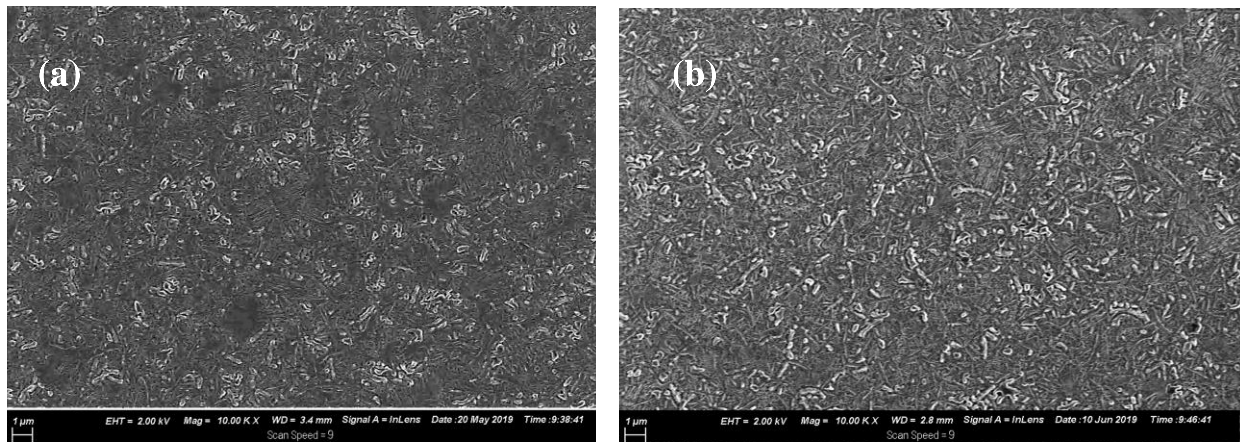

Fig. 6.10: SEM micrographs of room temperature selenium implanted SiC surfaces after vacuum annealing at 1350 °C for (a) 10 h and (b) 80 h.

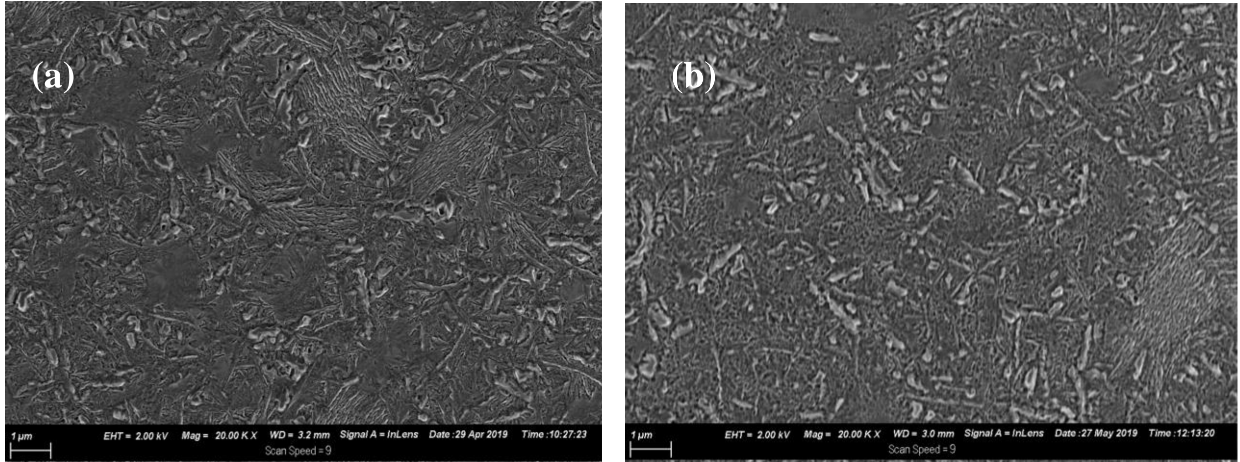

Fig. 6.11: SEM micrographs of room temperature selenium implanted SiC surfaces after vacuum annealing at 1400 °C for (a) 10 h and (b) 80 h.

6.1.3 RBS Results

In this work, the effects of annealing temperature on the migration behaviour of implanted Se was monitored by RBS. In Fig. 6.12, the measured as-implanted Se depth profile, the simulated Se profile and simulated damage in displacement per atom (dpa) are shown. The simulations were performed using SRIM 2013 [Zie12], assuming a displacement energy (E_d) of 20 eV and 35 eV for C and Si respectively [Dev01]. The radiation damage from SRIM 2013 was converted into displacements per atom (dpa) using equation (6.1) [Hla17]:

$$dpa = \frac{(\nu_{ca}/ion\text{Å}) \times 10^{8} \times \varphi\,(ions\ cm^{-2})}{\rho_{SiC}\,(atoms\ \ cm^{-3})} \tag{6.1}$$

where, ($\nu_{ca}/ion\text{Å}$) is the vacancy per ion from SRIM 2012, φ is the ion fluence (1×10^{16} cm^{-2}), ρ_{SiC} is the density of silicon carbide (9.641×10^{22} atoms.cm^{-3}).

The experimental projected range (Rp) of 87.7 nm was slightly lower than the theoretical value of 89.6 nm. The value obtained is within the experimental error of the RBS measurements about 5% and the uncertainties of the SRIM simulations. The experimental straggling (ΔRp) value is about 11% larger than that obtained by theoretical simulation viz. 29.9 and 26.5 nm, respectively. This discrepancy in the ΔR_P may be attributed to the fact that re-distribution of Se is already taking place during the implantation process. The implanted selenium profile is almost a Gaussian distribution with the kurtosis (β = 2.9) and skewness (γ = 0.28). These values

are very close to those of the true Gaussian distribution ($\beta = 3$) and ($\gamma = 0$). What is also evident in Fig. 6.12 is that the maximum damage of about 1.3 dpa is at about 70 nm below the surface as compared to the experimental Rp of 87.7 nm. If one assumes that 0.3 dpa amorphizes SiC [Gao02], it is quite clear that a 125 nm layer of SiC below the surface is amorphized. From these results it is quite clear that the majority of implanted Se is embedded in the amorphous SiC.

The relative atomic concentrations were quantified as a ratio of the density of selenium within SiC to the density of the SiC substrate. For this study, the density of SiC, $\boldsymbol{\rho_{SiC}}$, was taken to be 3.21 g cm^{-3}, which is equal to 9.641×10^{22} atoms.cm^{-3}. While the density of selenium, ρ_{Se} was calculated by converting the counts obtained from RBS as:.

$$\rho_{Se} = \frac{\emptyset dn}{ND} \quad (6.2)$$

where $\emptyset$ is the implanted fluence in cm^{-2} unit, N is the total selenium counts in counts unit, dn is the count per channel in counts unit and D is the depth resolution, represented in cm/channel unit.

Therefore, the relative atomic concentration (RAD (%)) is given by taking the ratio:

$$RAD(\%) = \frac{\rho_{Se}}{\rho_{SiC}} \times 100 \quad (6.3)$$

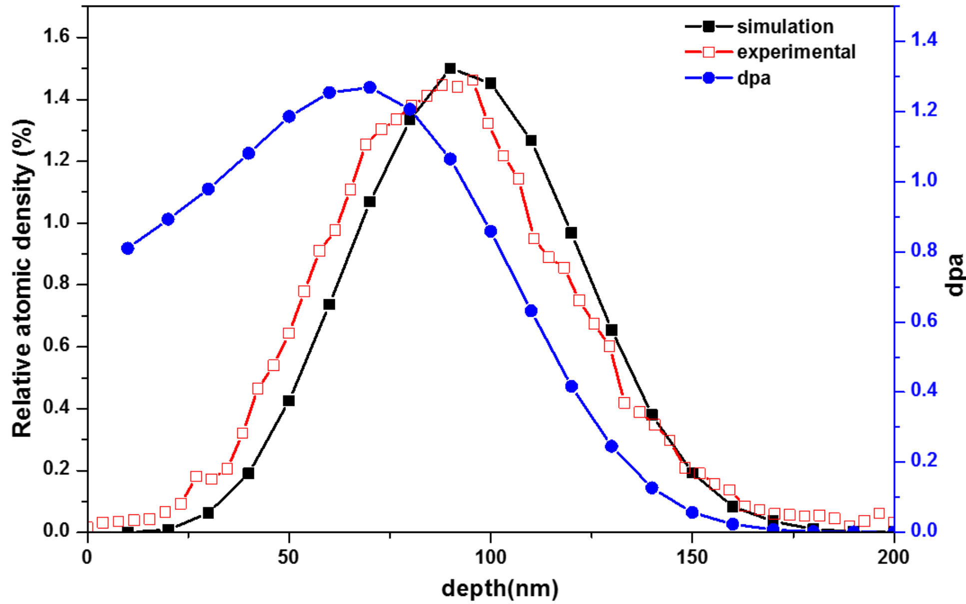

Fig. 6.12: The depth profile of Se implanted into SiC from RBS, SRIM 2012 simulated Se depth profile and damage in displacement per atom (dpa).

To investigate the migration behaviour of Se in polycrystalline SiC, the implanted samples were subjected to sequential annealing at temperatures ranging from 1000 to 1500 °C in steps of 100 °C for 10 h. The Se depth profiles obtained from RBS before and after annealing are shown in Fig. 6.13. The FWHM values (Fig. 6.14) were obtained from the range straggling (ΔRp) by: $\mathrm{FWHM} = 2\,\Delta\,\mathrm{Rp}\sqrt{2\ln 2}$ after fitting the profiles to a Gaussian function. Neither a change in the implanted Se profile nor broadening was observed after annealing at 1000 up to 1200 °C. These observations indicate the lack of detectable diffusion after annealing at these temperatures. A slight broadening of the implanted Se profile was observed after annealing at 1300 °C as can be seen in Figs. 6.13 and 6.14. However, both were within the experimental error of the depth scale of our RBS measurements. The broadening became more significant after annealing at 1400 °C and 1500°C. The broadening of the profile is an indication of diffusion of the implanted Se [Mal17]. It is also clear that annealing at 1300 °C and 1400 °C led to the thermal etching of the SiC layer, which moved the selenium profile towards the surface, resulting in the loss of some of the implanted Se (see Fig. 6.14). The annealing at a temperature of 1500 °C led to the decomposition of silicon carbide, as is evident in the formation of the carbon layer on top of the carbon surface (see Fig. 6.15). What was also noticeable was a general decrease in the heights of the Se profiles. To quantify this, the total integrated counts of the RBS Se signal (counts) were taken. The results are shown in Fig. 6.14. There was also a very slight asymmetry near the surface (i.e. x = 0) in the Se profiles at 1400

°C and 1500 °C. There are two possible reasons for this, namely segregation towards the surface and evaporation into the vacuum of the Se atoms which diffused to the surface. The boiling point of Se is 685°C is significantly less than the annealing temperatures.

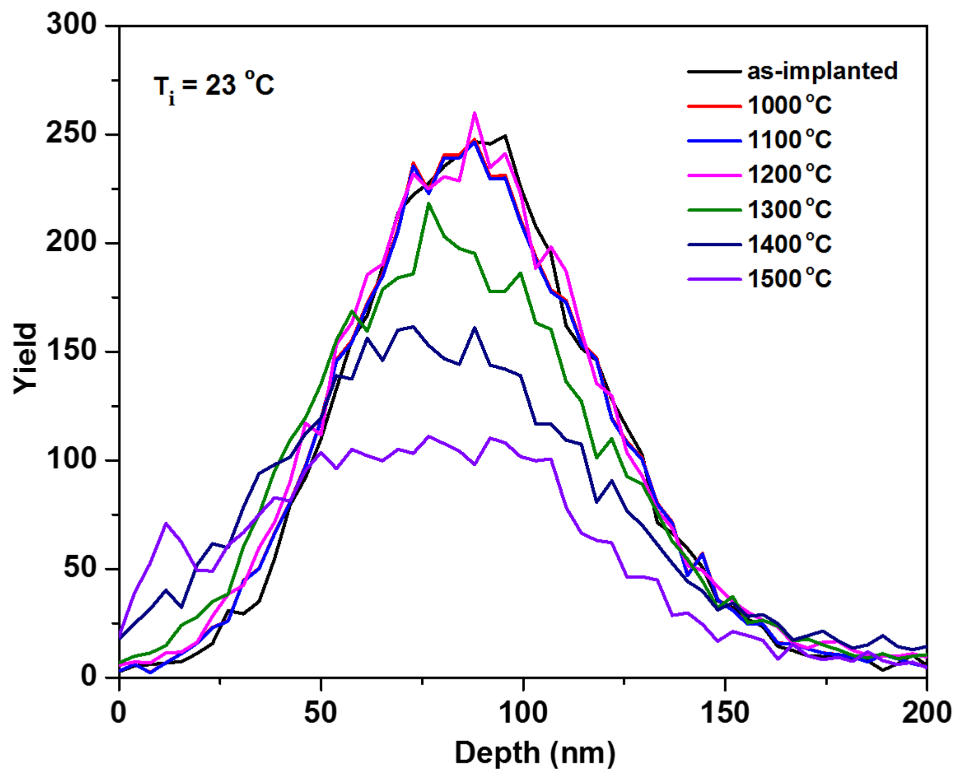

Fig. 6.13: Depth profiles of selenium implanted in SiC at room temperature and after sequential annealing from 1000 to 1500 °C for 10 h.

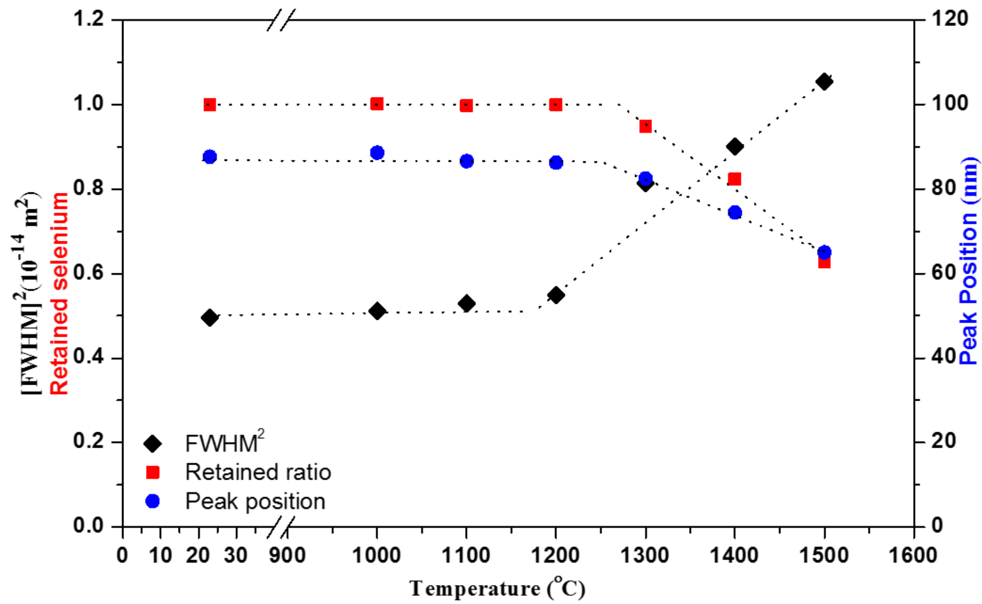

Fig. 6.14: The full width at half maximum, the peak position of implanted Se, and retained ratio (calculated as the ratio of the total integrated counts of Se after annealing to that of as-implanted) of the Se profile as a function of annealing temperature.

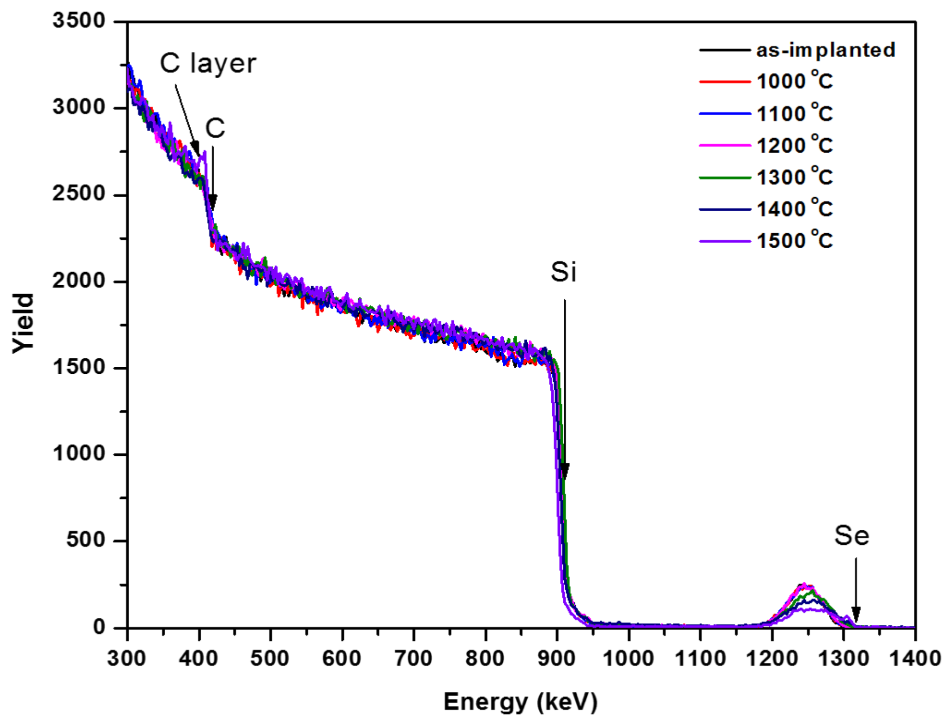

Fig. 6.15: RBS spectra of selenium implanted in SiC at room temperature and after sequential annealing from 1000 to 1500 °C for 10 h. Arrows indicate the surface positions of elements.

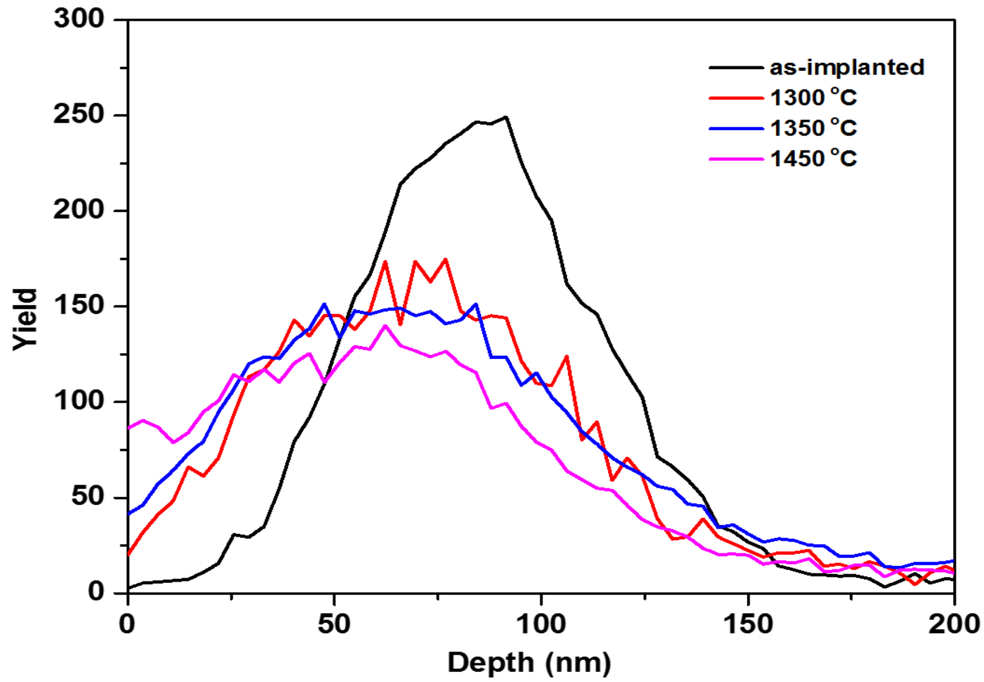

Fig. 6.16: Depth profiles of selenium implanted in SiC at room temperature and after sequential annealing at1300, 1350 and 1450 °C for 20 h.

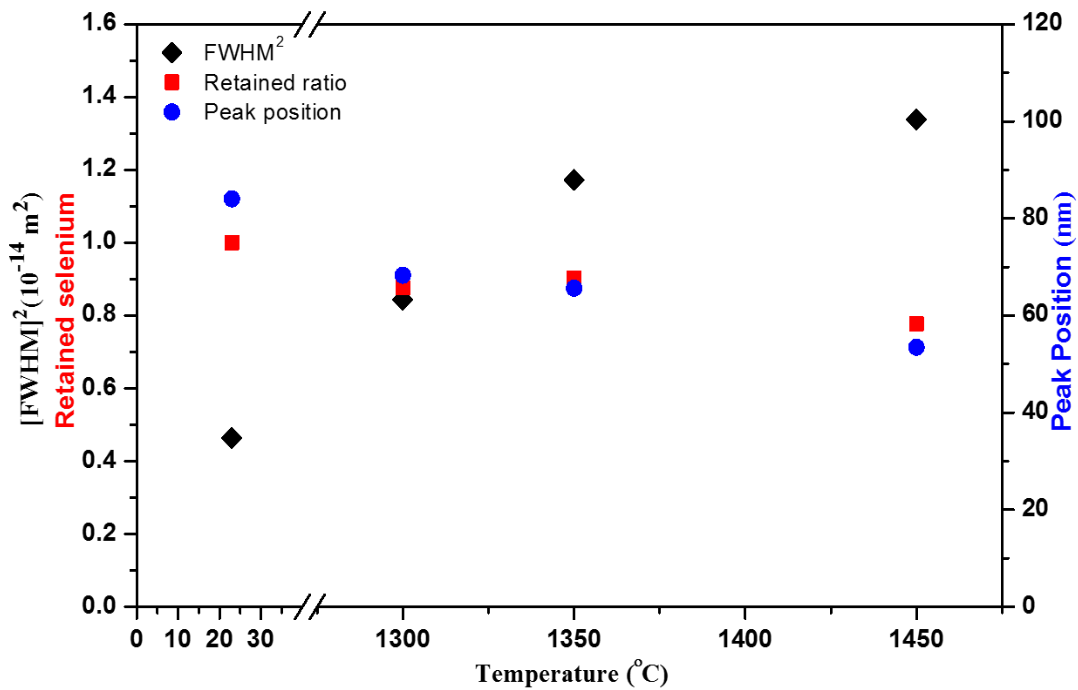

Fig. 6.17: The full width at half maximum, the peak position of implanted Se, and retained ratio (calculated as the ratio of the total integrated counts of Se after annealing to that of as-implanted) of the Se profile as a function of annealing temperature

A new as-implanted sample was subjected to sequential annealing at three different temperatures for 20 h as shown in Fig. 6.16, and it was found that the profile broadens and shifts toward the surface (see Fig. 6.17). There was also a significant loss of implanted Se (see Fig. 6.17). To extract the diffusion coefficient of Se implanted into polycrystalline SiC, the Se depth profiles obtained from RBS were fitted to the solution of Fick's diffusion equation for Gaussian as-implanted profile and with a perfect sink at the surface (see Fig. 6.18) [Mal17]. The diffusion coefficients of 6.3×10^{-21} and 2.0×10^{-20} m^2s^{-1} were extracted at 1300 and 1350 °C respectively. The diffusion coefficient at 1450 °C could not be determined because the Se profile deviated from the diffused profile derived in [Mal17]. This deviation was due to a segregation towards the surface.

There have been no reports on Se diffusion in SiC. Hence the obtained diffusion coefficients were not compared with any other literature values.

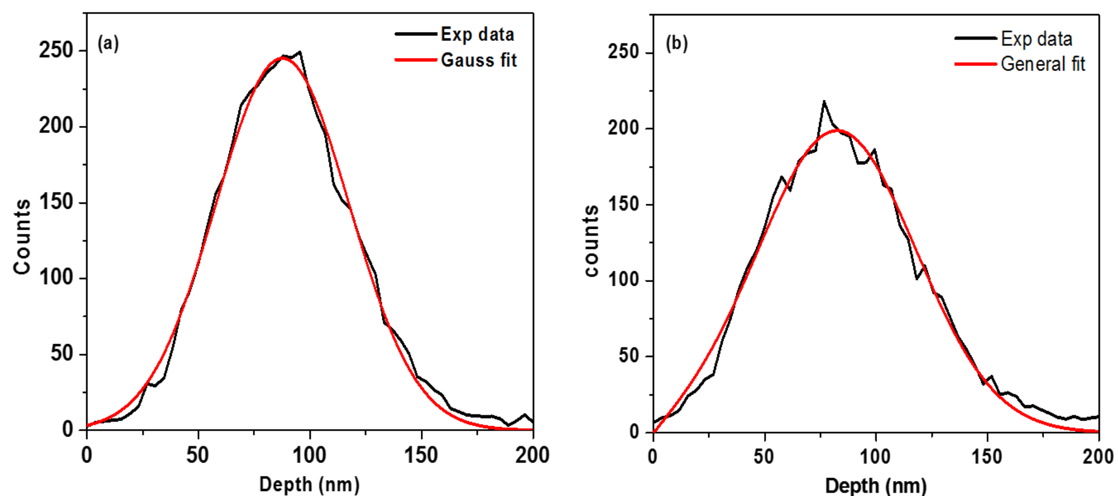

Fig. 6.18: Example of the fitting of the diffusion equation solution to the depth profiles of the sample (a) as-implanted, (b) annealed at 1300 °C for 10 h.

For the isothermal study, new samples implanted at room temperature were annealed at 1300 °C, 1350 and 1400 °C for 10 h cycles of up to 80 h. Fig. 6.19 depicts FWHM of the isothermally annealed samples. At 1300 °C, a strong broadening was observed during the first annealing cycle of 10 h. This confirms the presence of Fickian diffusion at this temperature. Further peak broadening was occurred during the second annealing cycle. No considerable broadening was observed after subsequent annealing cycles. This indicates that the diffusion of selenium

occurred only during the initial stages of annealing. Annealing at 1350 °C for 10 h led to a significant increase in peak broadening, compared to that obtained at 1300 °C. A further width broadening occurred up to the third annealing cycle. Whereas, no noticeable broadening occurred during the final annealing cycle (80 h). A similar curve to 1350 °C was obtained during isothermal annealing at 1400 °C. The fact that the measured width remain constant after the third annealing cycle indicates that the amorphous state resulting from implantation, which allows for selenium diffusion, is no longer available. This is in agreement with the results of Raman and SEM, as discussed in previous sections.

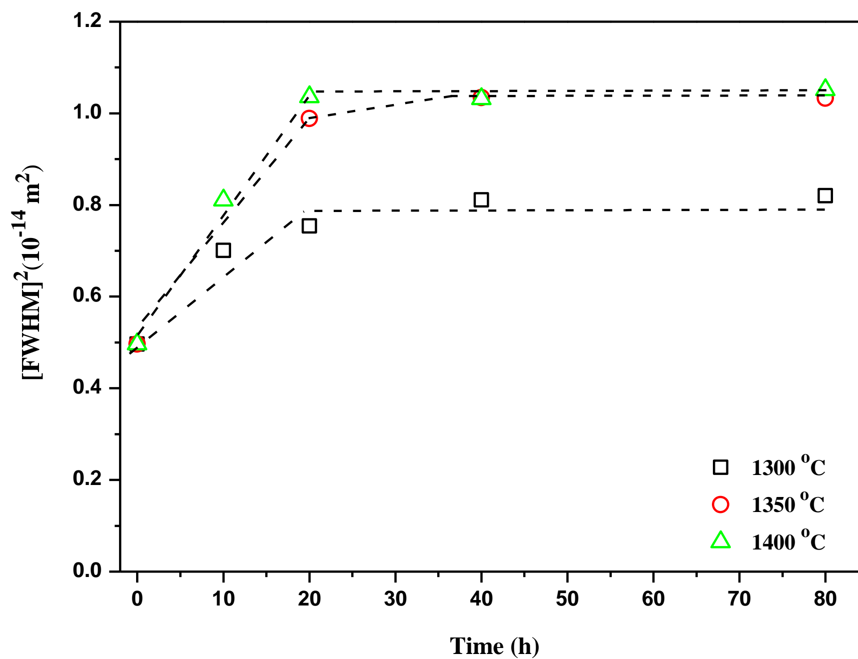

Fig. 6.19: Isothermal annealing curves of room temperature implanted samples at 1300 °C, 1350 °C and 1400 °C.

Fig. 6.20 depicts the retained selenium during isothermal annealing. The first annealing cycle (10 h) resulted in a loss of approximately 10 % in the sample annealed at 1300 °C, whereas the loss in both samples annealed at 1350 °C and 1400 °C are similar, about 15 %. This is due to the profile shift towards the surface caused by thermal etching during this cycle, allowing the implanted Se atoms to escape into the vacuum upon arrival to the surface. The loss became more significant during the subsequent annealing cycles. This loss was greater in samples

annealed at a higher temperature. In the final cycle (80 h), losses were approximately 20%, 25% and 40% at 1300 °C, 1350 °C and 1400 °C respectively. This explains the effect of temperature and time on the sublimation of silicon carbide, and thus the increased thermal etching, as will be discussed later.

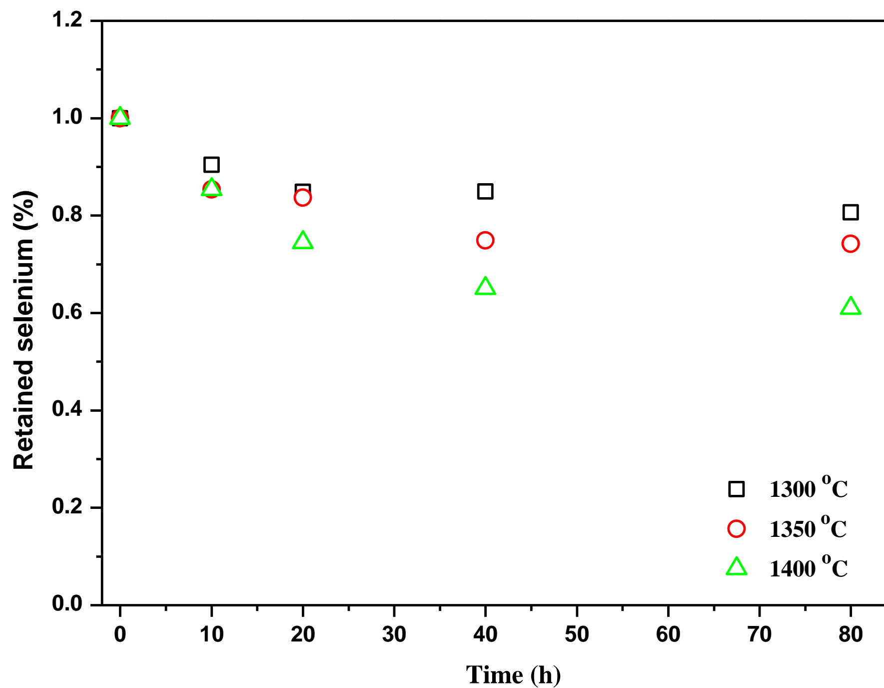

Fig. 6.20: The retained ratio of Se implanted into polycrystalline SiC at room temperature after isothermal annealing.

For isothermal annealing, diffusion coefficients D were extracted by comparing squares of FWHM of selenium profiles after annealing with that of the as-implanted sample. This was done using the following equation [Mye74]:

$$[W(t)]^2 = 4Dt\ln(2) + [W(0)]^2 \qquad (6.4)$$

Where $W(0)$ and $W(t)$ are the FWHM of the as-implanted sample and its FWHM after annealing for time t, respectively. Thus, the diffusion coefficient D was directly obtained from the initial slope of a plot of $[W(t)]^2$ vs annealing time t at a constant temperature as shown in Fig. 6.19. The diffusion coefficients at 1300, 1350 and 1400 °C were found to be 1.4×10^{-20} m^2s^{-1}, 2×10^{-20} m^2s^{-1} and 2.5×10^{-20} m^2s^{-1}, respectively.

Since diffusion obeys the Arrhenius equation in the following form:

$$\ln D = -\frac{E_a}{k_B}\frac{1}{T} + \ln D_o \qquad (6.5)$$

The activation energy, E_a and pre-exponential factor, D_o of selenium diffusion in amorphous silicon carbide can be determined from the slope of the line graph of ln D versus the inverse of the temperature. From the Arrhenius plot as shown in Fig. 6.21, the values for E_a and D_o were found to be 2 $\times 10^{-22}$ J and 1.7 $\times 10^{-16}$ m^2s^{-1}, respectively.

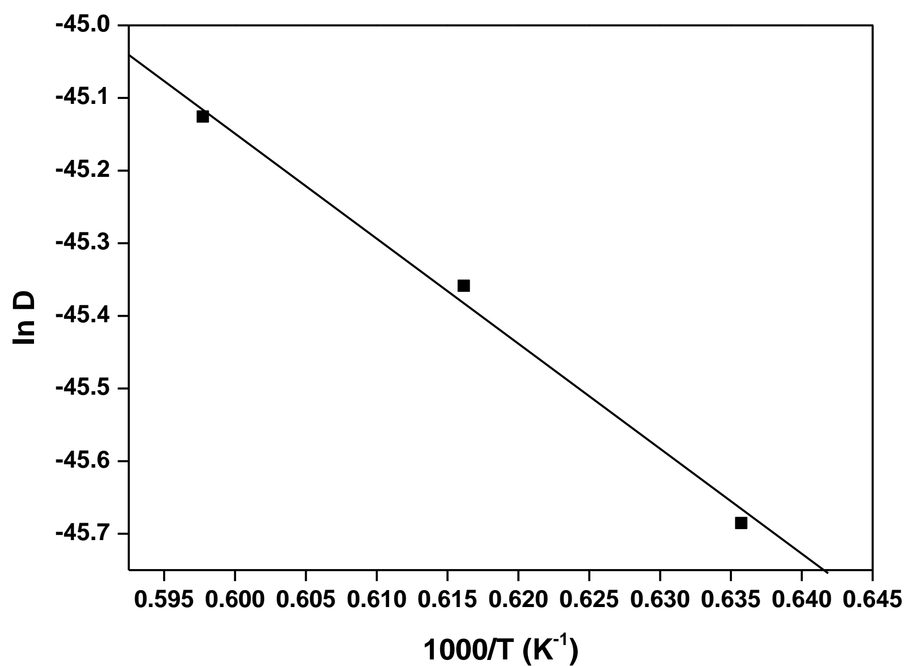

Fig. 6.21: The plot of $\ln D$ *versus 1/T for annealing temperatures of 1300, 1350 and 1400 °C for Se implanted into polycrystalline SiC at RT.*

6.2 Hot implantation

6.2.1 Raman Results

The Raman spectra of the pristine sample and as-implanted at RT, 350 ºC and 600 ºC samples are shown in Fig. 6.22. The spectrum of the pristine sample displays three features in the 700-1100 cm^{-1} region, indicating the characteristic Raman modes of silicon carbide [Des16] [Nak97] [Sor06]. The two peaks at 771 and 797 cm^{-1} correspond to the transverse optic (TO) mode, and peak at 966.5 cm^{-1} correspond to longitudinal optic (LO) mode. As can be seen from the Fig. 6.22, implantation at room temperature resulted in the disappearance the characteristic SiC Raman peaks, indicating that the SiC layer is amorphized. The three dominant features of Raman spectra of SiC between 700 and 1100 cm^{-1} were retained in the samples implanted at 350 °C and 600 °C. Fig. 6.22 also shows that the Raman intensity of samples implanted at 600 °C is higher than those implanted at 350 °C, suggesting a lower concentration of defects in the former [Sor06].

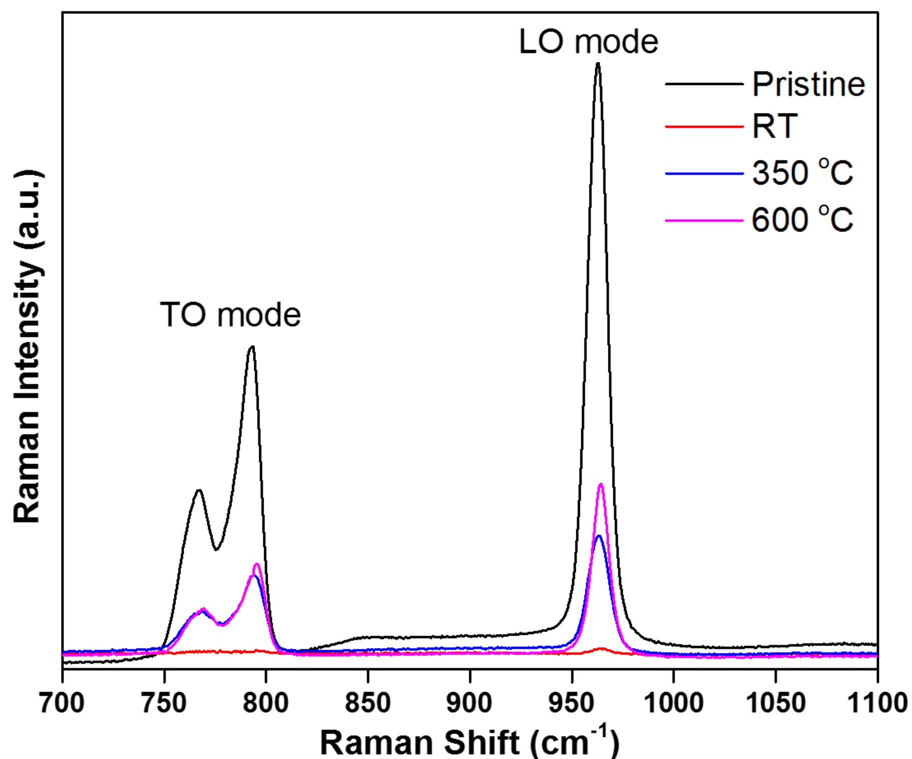

Fig. 6.22: The Raman spectra of the pristine poly-SiC and SiC implanted with Se at RT, 350 °C and 600 °C.

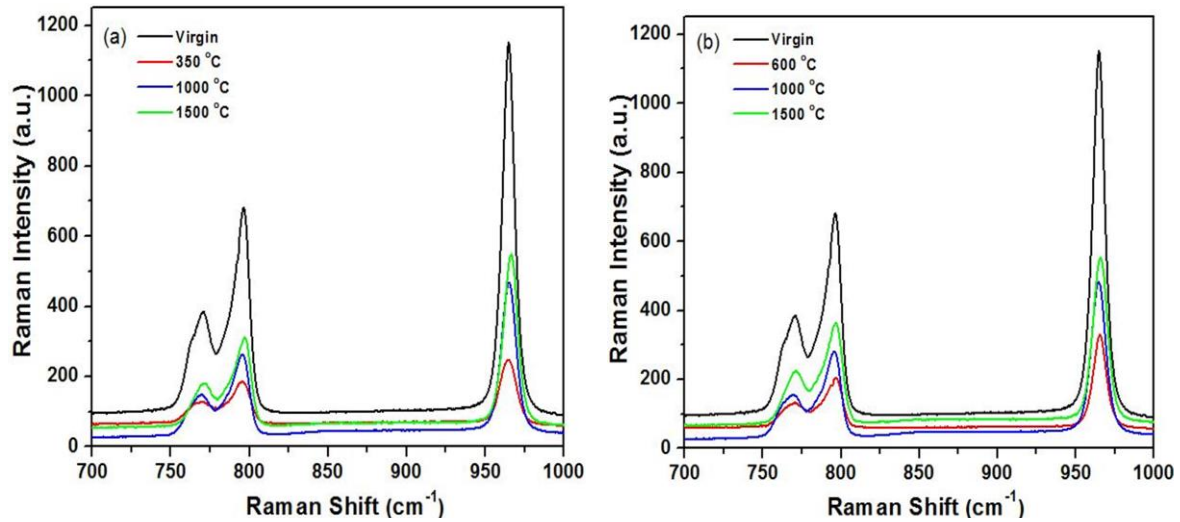

Fig. 6.23: Comparative Raman spectra from selenium implanted into poly-SiC at (a) 350 °C and (b) 600 after sequential annealing at 1000 and 1500 °C for 10 h.

Fig. 6.23 (a) and (b) show the Raman spectra of poly-SiC after sequential annealing at 1000 and 1500 °C for 10 h for samples implanted at 350 °C and 600 °C, respectively. In both high temperature implanted samples, a comparison of the Raman intensity shows that annealing at 1000 °C caused an increase in the peak intensity. The higher relative Raman intensity means fewer defects in SiC. Intensity increased with the annealing temperature, but it did not reach to the one of virgin sample, even after annealing at 1500 ° C, indicating the presence of defects.

The average stress in the samples was calculated using the change in LO Raman mode as discussed in [Zon18]. Fig. 6.24 shows the evolution of residual stress with annealing temperature. Implantation at 350 ºC caused a modification in the mechanical properties of the sample with a residual tensile stress of 0.86 GPa. This is due to the increase of the chemical bond length, relative to their length in the unstressed crystals [Tus19] [Wen12]. Annealing at 1000 °C showed the similar stress level. Slight increase in the residual stress was observed after annealing at 1100 °C. Annealing at 1200 °C and 1300 °C reduced the amount of residual tensile stresses to the same level. Further annealing at 1400 ° C resulted in a decrease in tensile stress. The stress reached a minimum value of 0.75 GPa at 1500 °C. For the sample implanted at 600 °C, the implantation induced tensile stress of 0.95 GPa. After annealing in the range between 1000 °C and 1500 °C, approximately the same scenario occurred as in the sample implanted at 350 °C. This indicates that the internal stress distributions are almost the same. In this study, the residual stress of the RT as-implanted sample cannot be calculated because of the disappearance of Raman modes due to the amorphization. Comparing these results with the

Se migration results in SiC, as will be discussed later, the difference in residual stress level has no role in migration of implanted Se.

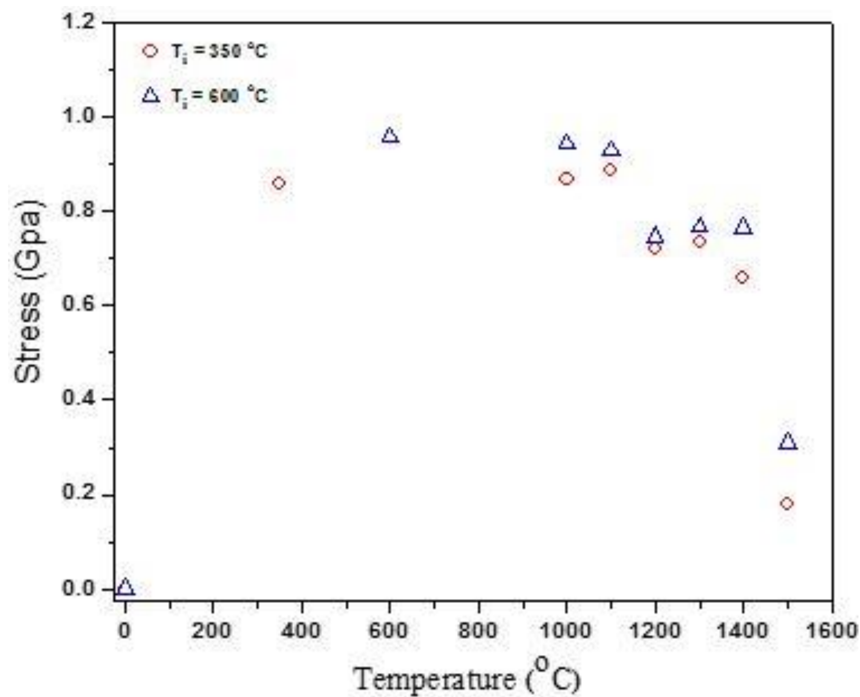

Fig. 6.24: The residual stress in the poly-SiC samples implanted with Se at 350 °C and 600 °C as a function of annealing temperature.

For the isothermal study, new samples implanted at 350 °C and 600 °C were annealed at temperatures of 1300 °C, 1350 °C and 1400 °C for 10 h cycles up to 80 h. The LO modes are shown in Fig. 6.25 and Fig. 6.26. In both samples, annealing at 1300 °C caused the intensity of LO mode to increase. Fig. 6.27 shows a general increase in the intensity of LO mode with increasing annealing cycles up 80 h in both implanted samples (350 °C and 600 °C implanted samples) at this temperature. Fig. 6.27 (a) shows that annealing of the sample implanted at 350 °at 1300 °C for 10 h resulted in the appearance of the LO peak at 350.1 a. u, which is 101.9 a.u higher than the one of the implanted sample. This indicates an increase in the size of the SiC grains.

Annealing the 600 ºC implanted sample at 1300 °C for 10 h increased the intensity from 329.5 a.u to 393.5 a.u .as can be seen in Fig. 6.27 (b). Annealing the 350 ºC implanted samples at 1350 °C caused an increase in intensity by 296.5 a.u., while the increase was 309.5 a. u. in case of the sample implanted at 600 °C. Fig. 6.27 also shows that the LO mode of 600 °C is more intense as compared to 350 °C during the first annealing cycle. For the samples implanted at 350 °C, a slight increase in intensity was observed during the second annealing cycle and no

change was observed for any further annealing cycles up 80 h. Annealing the 350 °C and 600 °C implanted samples at 1400 °C for 10 h increased the LO mode intensity for the same positions as those at 1350 ° C. The intensity increased slightly during subsequent annealing cycles up to 80 h in both samples. The overall results demonstrate the intensity increases with time up to a value that depends on temperature.

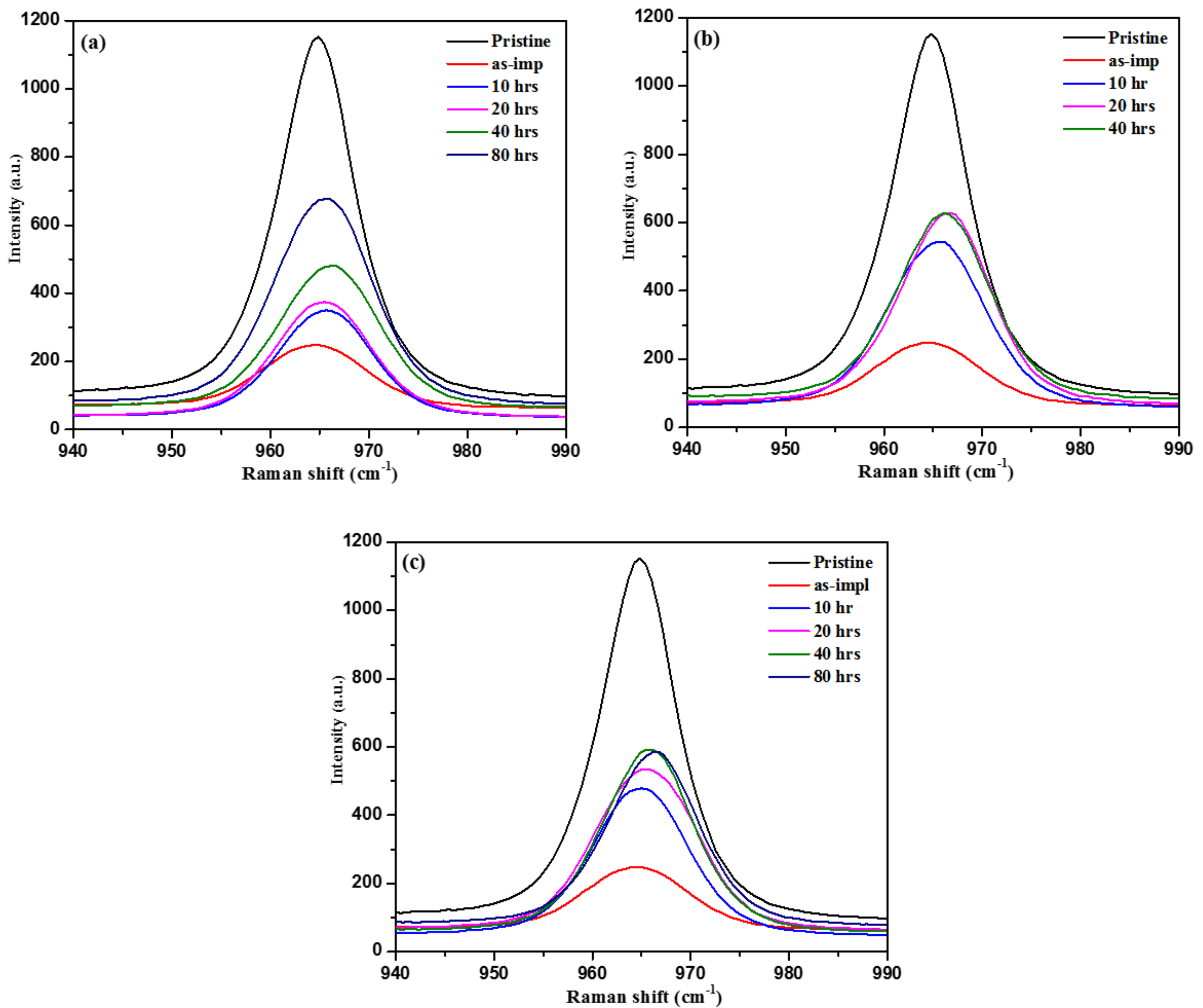

Fig. 6.25: LO modes of SiC Raman spectra of samples implanted with Se at 350 °C as a function of time during isothermal annealing at temperatures of (a) 1300 °C, (b) 1350 °C and (c) 1400 °C.

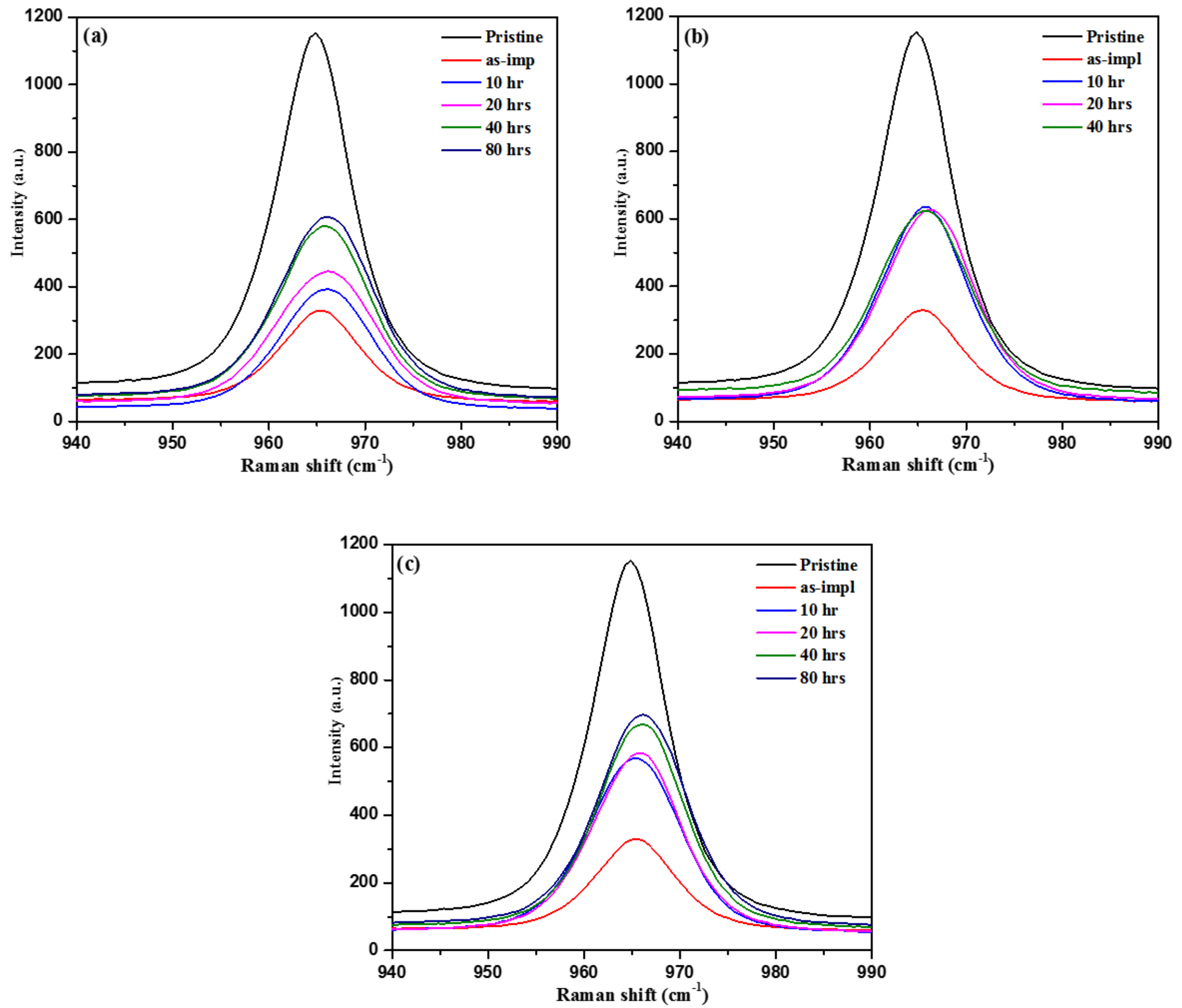

Fig. 6.26: LO modes of SiC Raman spectra of samples implanted with Se at 600 °C as a function of time during isothermal annealing at temperatures of (a) 1300 °C, (b) 1350 °C and (c) 1400 °C.

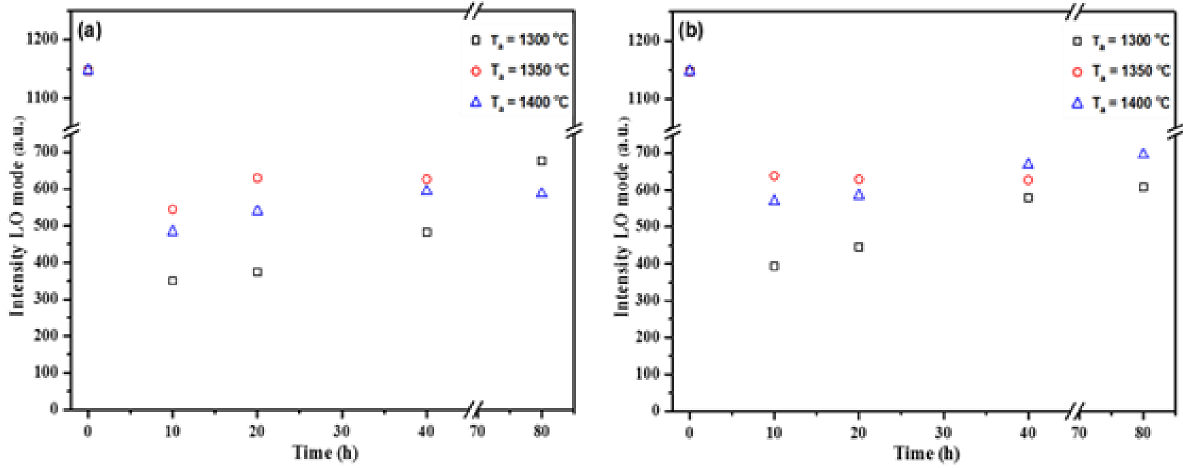

Fig. 6.27: The intensity of LO mode of SiC implanted with Se at (a) 350 °C and (b) 600 °C as a function of time during isothermal annealing at different temperatures.

The FWHM of LO mode obtained from 350 °C and 600 °C implanted samples are 12.1 cm^{-1} and 11.96 cm^{-1}, respectively. These values are broader in comparison with the virgin sample (9.6 cm^{-1}). In both implanted samples, at all temperatures (1300 °C, 1350 °C and 1400 °C), the intensity decreased to approximately 11.5 cm^{-1} during the first annealing cycle as can be seen in Fig. 6.28(a) and (b). This indicates an increase in the degree of crystallinity. No considerable changes were observed during the subsequent annealing cycles up to 80 h. This indicates that defects are still present in the samples.

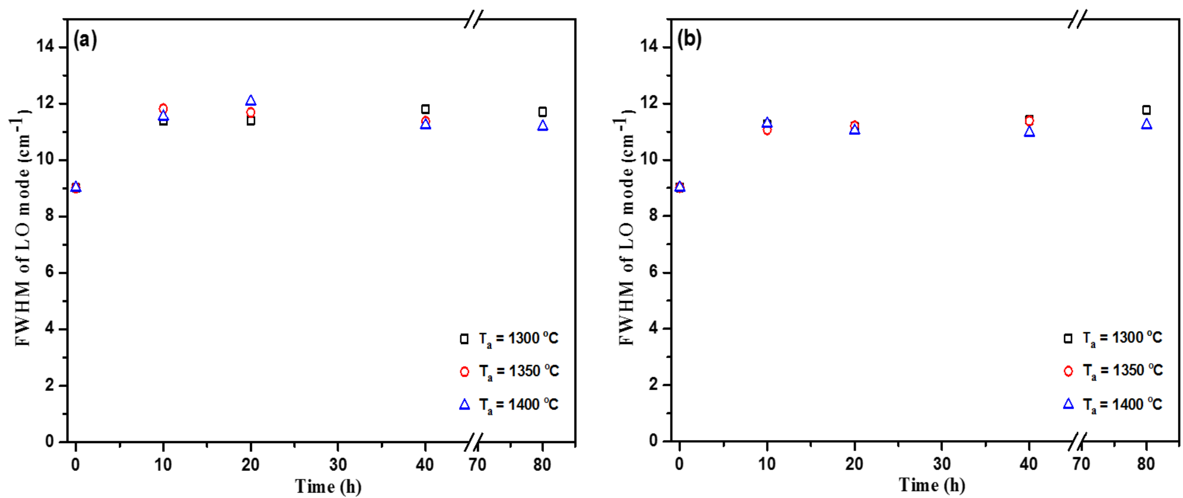

Fig. 6.28: The FWHM of LO mode of SiC implanted with Se at (a) 350 °C and (b) 600 °C as a function of time during isothermal annealing at different temperatures.

In Fig. 6.29 (a) it is quite evident that isothermal annealing of 350 °C implanted samples at 1300 °C and 1350 °C resulted in the appearance of the LO mode at approximately 965.5 cm^{-1} during the first annealing cycle, which is 0.8 cm^{-1} higher than that one of the pristine sample (964.7 $cm^{-1)}$. This indicates the presence of the compressive stress in bonds between atoms as a result of a change in atomic distances. No changes in the LO mode position was observed during the subsequent annealing cycles up to 80 h at these temperatures. Whereas in the 350 °C sample annealed at 1400 °C, the LO mode appeared at 965.5 cm^{-1}, suggesting less compressive stress compared to those of 1300 °C and 1350 °C . The intensity increased slightly, becoming 966.3 cm $^{-1}$ during the final 80-h cycle. In the case of the 600 °C implanted samples, Fig. 6.29 (b), isothermal annealing at 1300 °C, 1350 °C and 1400 °C resulted in the appearance of the LO mode at approximately 965.7 cm^{-1} during the first annealing cycle. No change in LO position was observed during the subsequent annealing cycles up to 80 h at all temperatures.

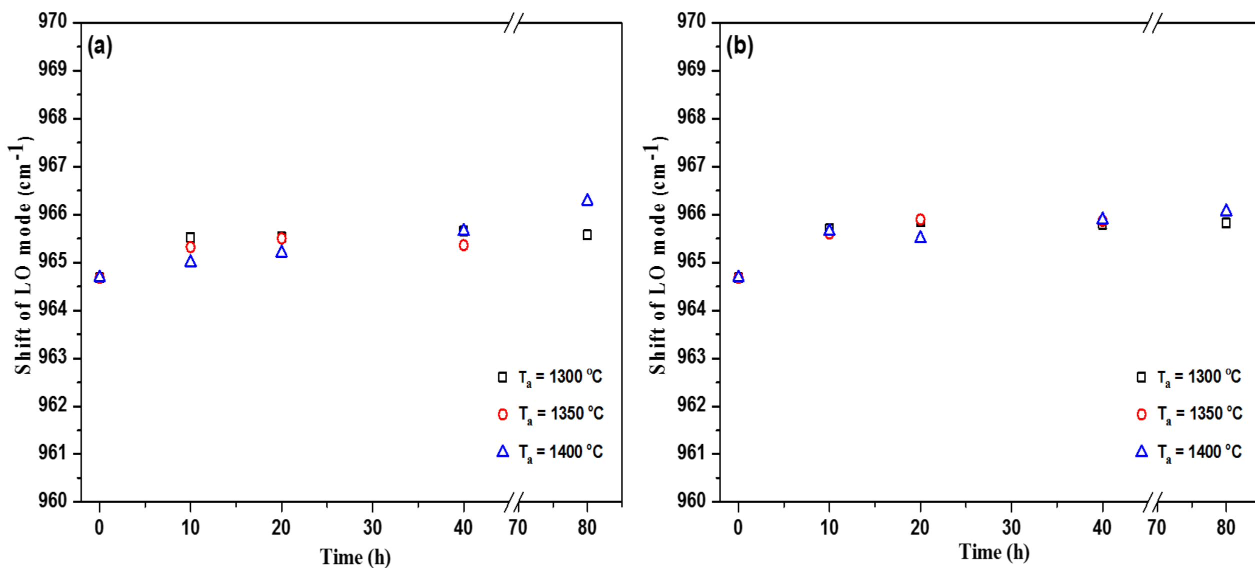

Fig. 6.29: The Raman shift of LO mode of SiC implanted with Se at (a) 350 °C and (b) 600 °C as a function of time during isothermal annealing at different temperatures.

6.2.2 SEM Results

SEM micrographs of the 350 °C and 600 °C implanted samples are shown in Fig. 6.30. Implantation at 350 °C (near to the critical temperature for amorphization) reduced the polishing marks with grains still visible (Fig. 6.30 (a)) compared to Fig. 6.7 (b), indicating the presence of the crystalline structure. No significant change was observed on the surface of the sample implanted at 600 °C compared to of the pristine (Fig. 6.7 (a)), because the implantation was performed at a temperature well above the critical temperature for amorphization.

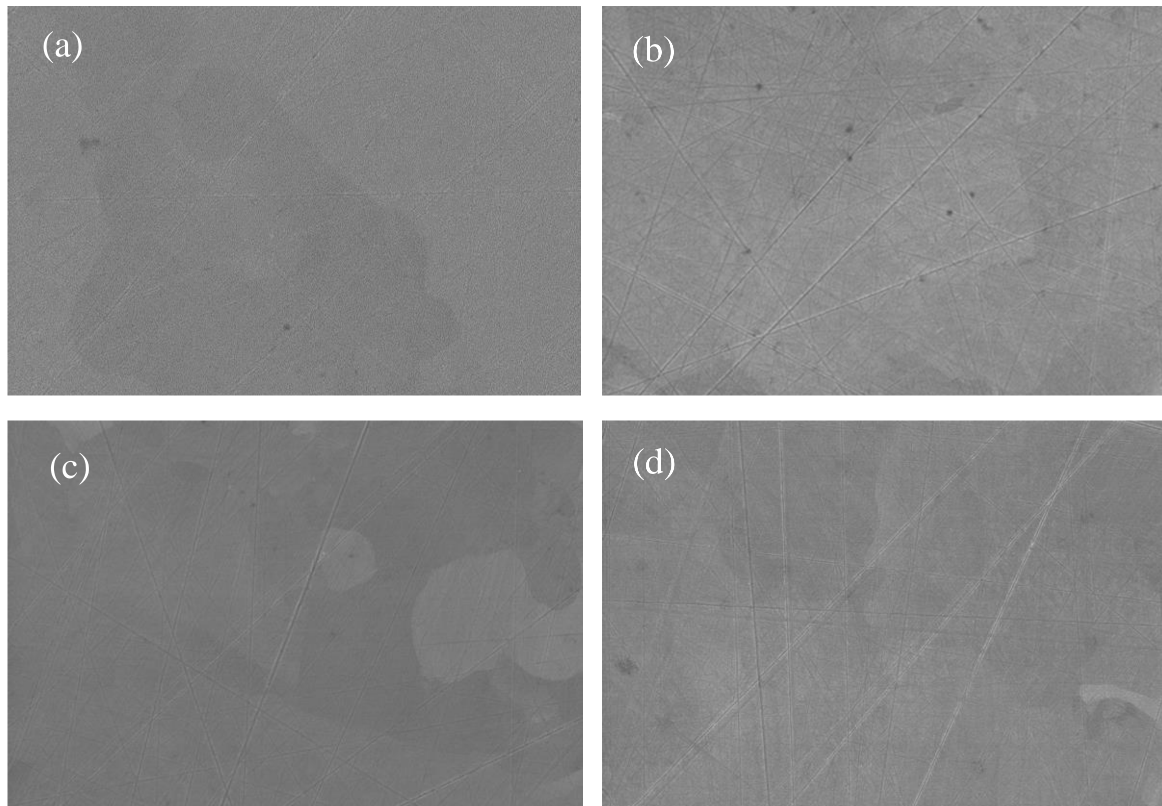

Fig. 6.30: SEM micrographs of poly-SiC after implantation with Se at (a) 350 °C and (b) 600 °C; compared with surfaces after vacuum annealing at 1000 °C for samples implanted at (c) 350 °C and (d) 600°C for 10 h.

SEM micrographs showed that no morphological changes occurred after annealing the samples implanted at high temperatures at 1000 °C (Fig. 6.30 (c) and (d)). Annealing at 1100 ºC (Fig. 6.31 (a) and (b)) resulted in the clear visibility of grains and their boundaries with polishing marks still present. Similar results were observed after annealing at 1200 ºC (not shown). In the case of the 350 °C implanted sample, annealing at 1300 °C and above caused the grain

boundaries to become more apparent, as well as the presence of pore openings on these boundaries as shown in Fig. 6.32 (a) and (b). These observations are due to thermal etching and uneven grain growth, which occurred during annealing. The low surface bonding energies at and near grain boundaries have made the SiC molecules to sublimate faster than those in the middle of crystal surfaces [Van12].

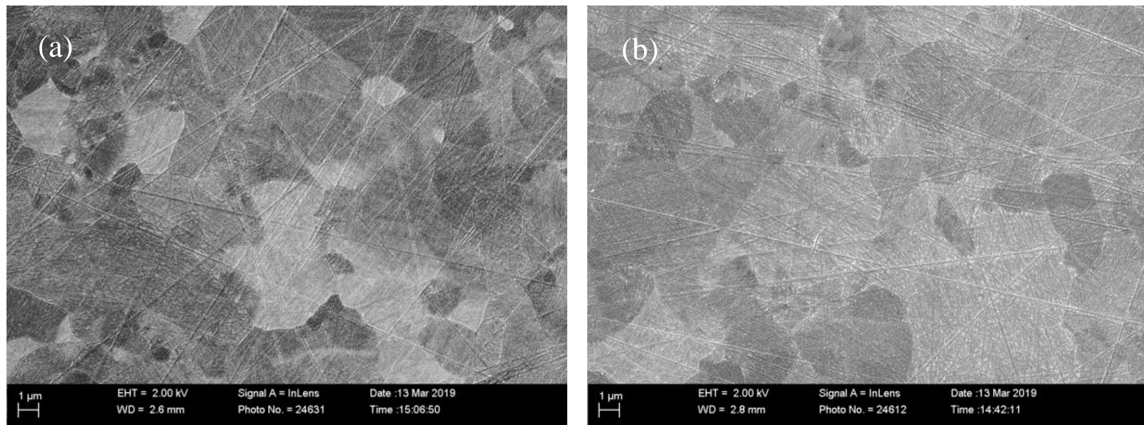

Fig. 6.311: SEM micrographs after vacuum annealing at 1100 °C for samples implanted at (a) 350 °C and (b) 600°C for 10 h.

An inspection of the SEM images shows a decrease in the grain sizes of the implanted samples after annealing and with increasing temperature. The Se ion bombardment introduced many defects in the crystalline SiC. Some of these defects are line and plane defects. Stacking faults introduce either new SiC poly-types or smaller 6H-SiC crystallites. The implanted Se impurities also inhibit crystal growth leading to smaller crystallites with increasing annealing temperature.

Furthermore, the appearance of pore openings on surfaces of the hot implanted samples at higher annealing temperatures as can be seen in Fig. 6.32. In contrast, these openings cannot be observed in the case of the RT implanted sample (see Fig. 6.7 and Fig. 6.8). This might be due to the significant change in stress/strain in the hot implanted samples at these temperatures as discussed in the Raman analysis.

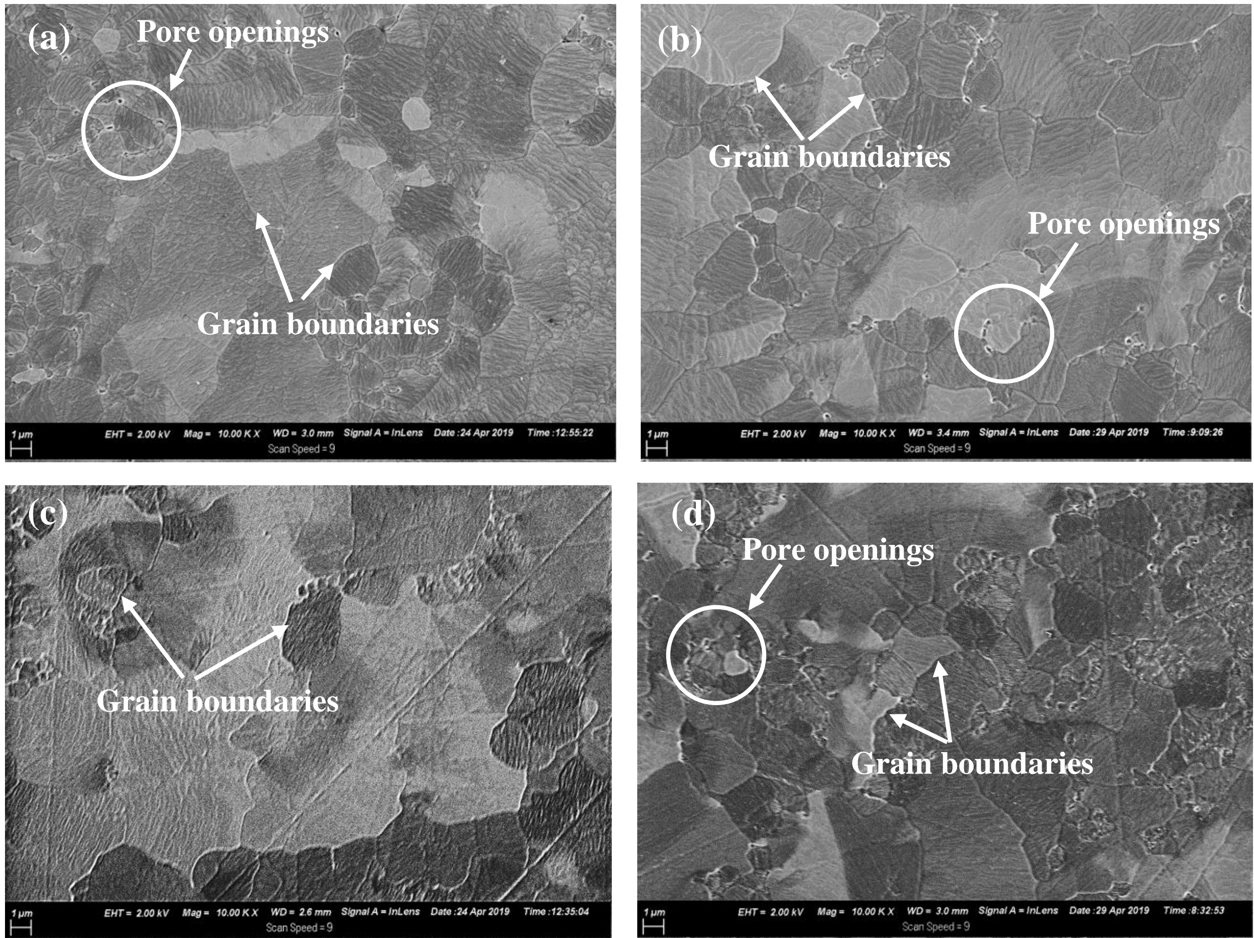

Fig. 6.32: SEM micrographs of the 350 °C implanted sample after vacuum annealing at (a) 1300 °C, (b) 1400 °C, the 600 °C implanted sample after vacuum annealing at (c) 1300 °C and (d) 1400 °C for 10 h.

Fig. 6.33 shows the surfaces of the 350 °C implanted samples after the first 10 h annealing cycle at 1300 °C, 1350 and 1400 °C. Annealing at 1300 °C resulted in grains of different size, indicating the recrystallization of the surface layer. The grains and their boundaries were clearly observed on the surface of the implanted and annealed sample at 1350 °C. The grains were most pronounced after annealing at 1400 °C, suggesting higher recrystallization at this temperature.

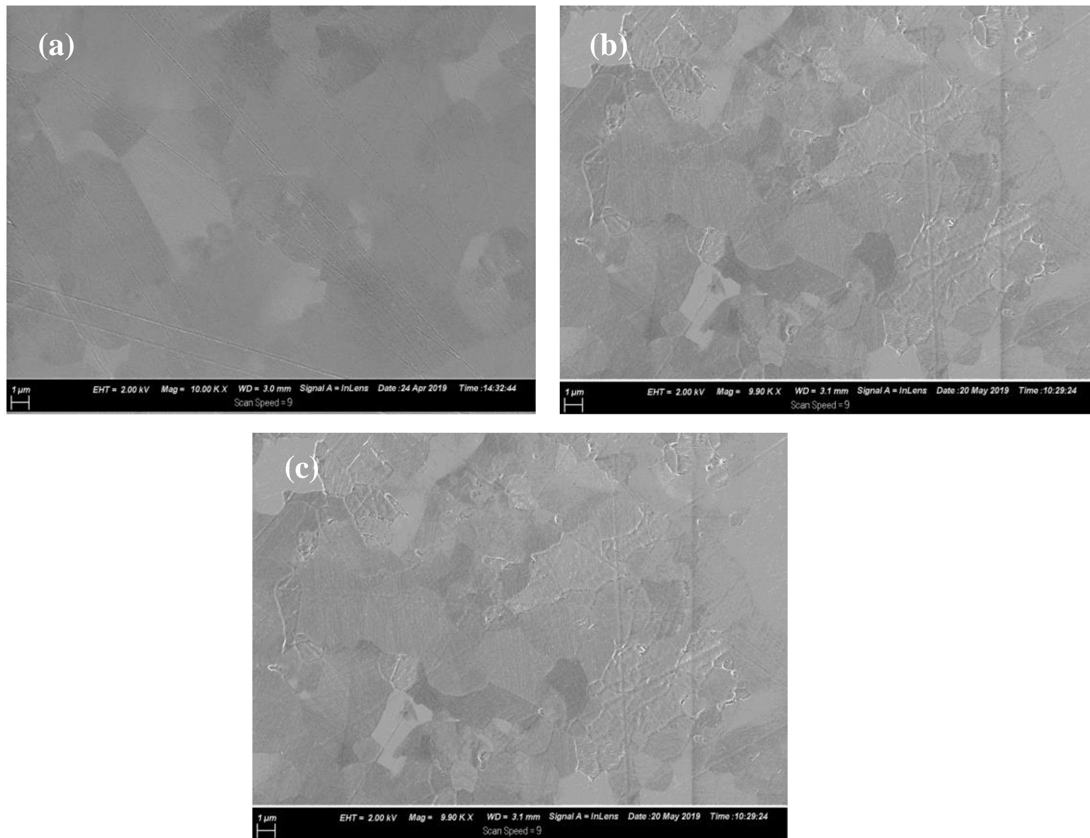

Fig. 6.33: SEM micrographs of the 350 °C implanted samples in the first annealing cycle (10 h) at (a) 1300 °C, (b) 1350 °C and (c) 1400 °C.

Fig. 6.34 shows SEM micrographs of the 600 ºC implanted sample annealed at 1300 °C, 1350 and 1400 °C for 10 h (first annealing cycle). Annealing at 1300 °C reduced mechanical polishing marks compared to the as implanted sample - see Fig. 30 (b) and Fig. 34 (a). This is due to thermal etching occurring at this temperature. SEM micrographs indicated no difference in surface morphology between samples annealed at 1300 °C and 1350 °C- see Fig. 6.34 (a) and (b), suggesting that both samples were thermally etched to the same depth at these temperatures. These observations are in agreement with the RBS analysis of the peak positions that will be discussed later. In a SEM micrograph of the 600 °C implanted then annealed at 1400 °C, the grains boundaries of the crystallites are clearly visible as can be seen from Fig. 6.34 (c), also pore openings on these boundaries as shown in Fig. 6.34(c). This is also due to thermal etching and uneven grain growth, which occurred during annealing, as discussed earlier in the sequential annealing results. No major morphological changes were observed in the hot implanted samples during the subsequent annealing cycles at different temperatures.

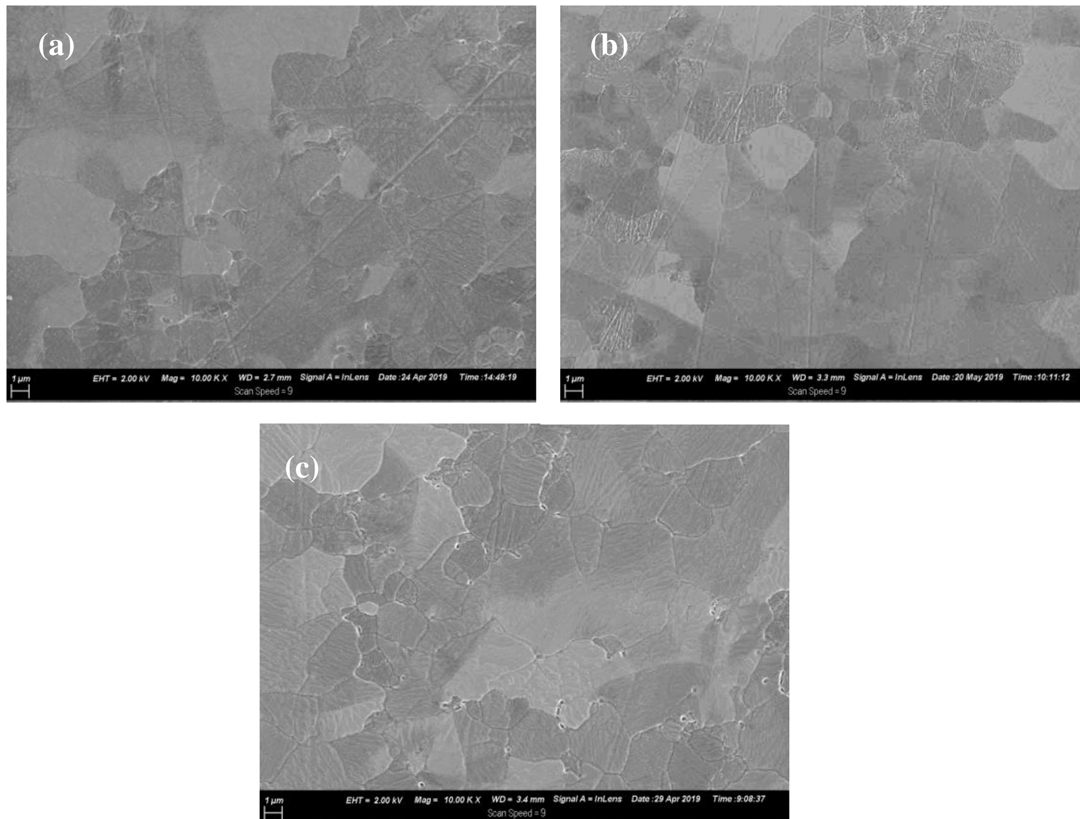

Fig. 6.34: SEM micrographs of the 600 °C implanted samples in the first annealing cycle (10 h) at (a) 1300 °C, (b) 1350 °C and (c) 1400 °C.

In both hot implanted samples, isothermal annealing at 1350 °C and 1400 °C for 10 h cycles up to 80 h caused slight changes during the third cycle (40 h). These changes were accompanied by an increase in the number of pore openings on the grain boundaries at 1400 °C. In the case of isothermal annealing at 1300 °C, the grain boundaries became more pronounced and the appearance of pore openings on these boundaries during the second (not shown) and third cycles. No significant morphological changes were observed for any further annealing longer than the third cycle at the same temperatures (see Fig. 6. 35 and Fig. 6. 36).

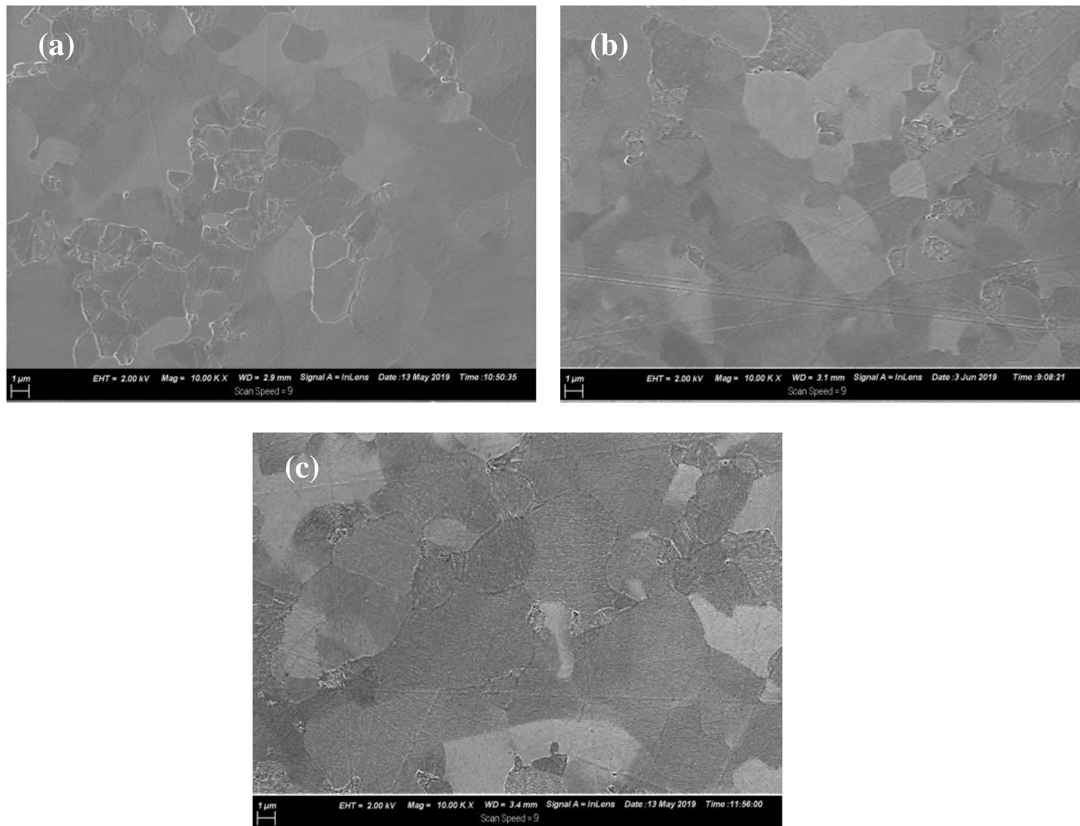

Fig. 6.35: SEM micrographs of the 350 °C implanted samples after annealing at (a) 1300 °C, (b) 1350 °C and (c) 1400 °C for 40 h.

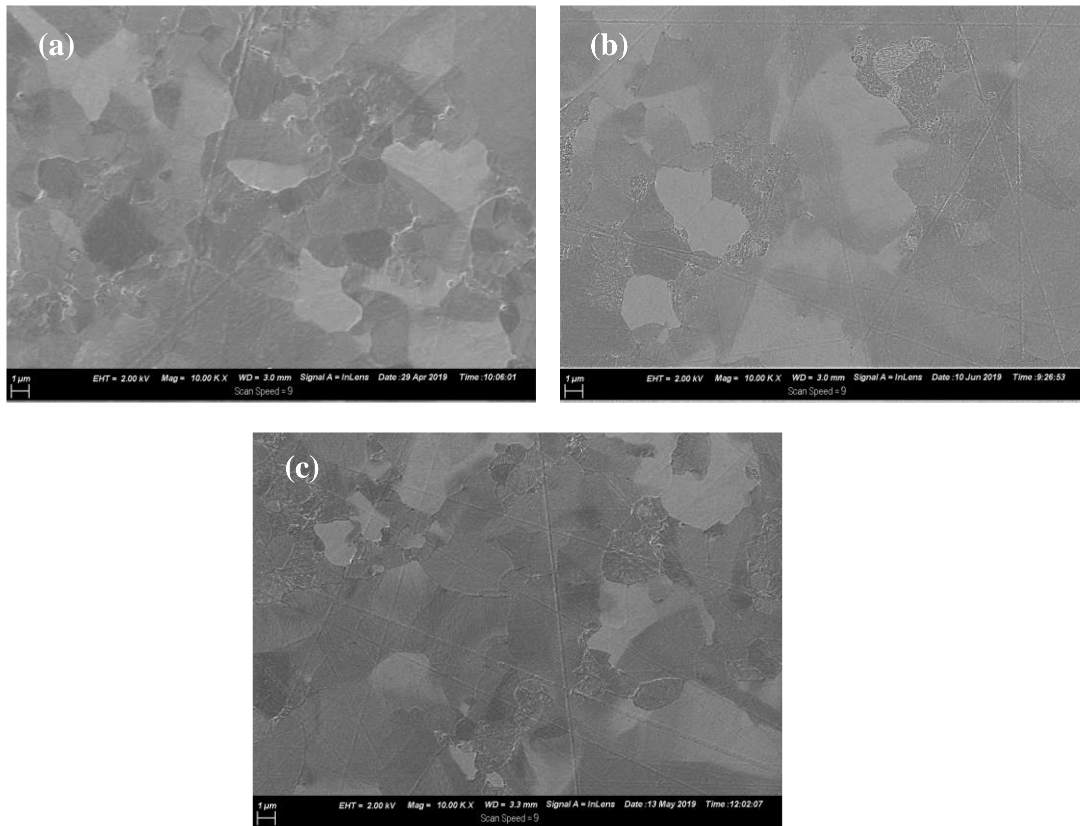

Fig. 6.36: SEM micrographs s of the 600 °C implanted samples after in annealing at (a) 1300 °C, (b) 1350 °C and (c) 1400 °C for 40 h.

6.2.3 RBS Results

In Fig. 6. 37, the RBS Se depth profiles of samples implanted at room temperature 350 ºC, and 600 ºC are shown. The Se depth profile obtained from the room temperature implanted sample and the simulated depth profile are included for comparison. The depth profiles of as-implanted samples obtained from RBS were fitted to Edgeworth distribution equation to extract the first four moments. The agreement between the projected ranges, together with their ranges straggling is within the profile fitting errors for Gaussian distribution and experimental error of the RBS measurements – see Table 6.1. The average of the projected range of 90 ± 2.9 nm is very comparable to the theoretical value of 89.6 nm. The results showed that the difference of the range straggling between the average of experimental measurements (34.6 ± 2.9 nm) and theoretical value (26.5 nm) is higher than that of the projected range. This discrepancy in the straggling can be attributed to the fact that the radiation enhanced diffusion in implantation process and the gurgitation of state density of charge as ions penetrate target are not considered

in SRIM calculations [Qin11]. Also shown in Table 6.1 are kurtosis (β) and skewness (γ) values obtained from the RBS as implanted profiles and SRIM calculation which indicate that the profiles are nearly Gaussian distribution.

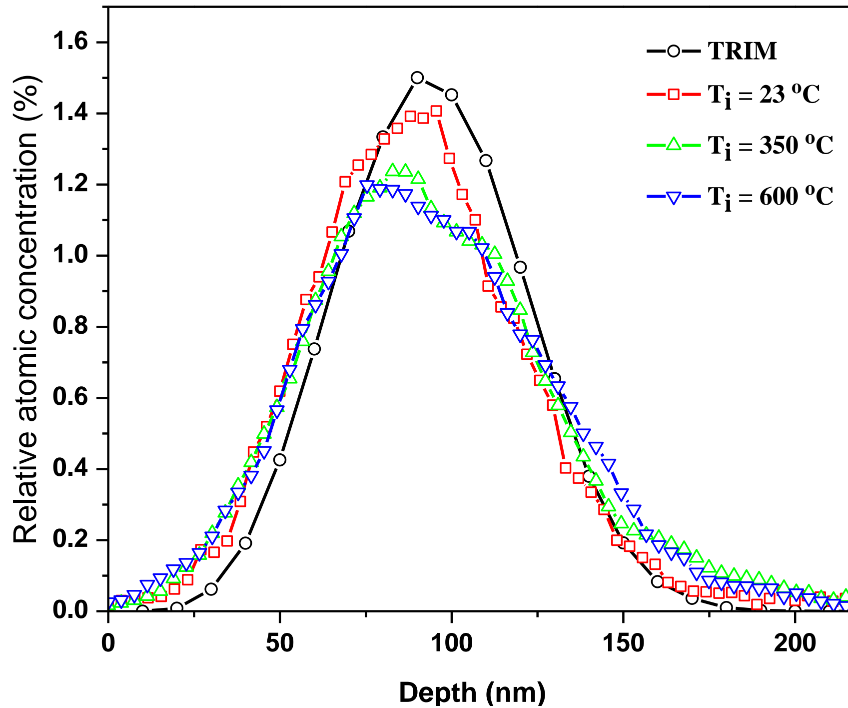

Fig. 6.37: The depth profiles of 200 keV Se implanted into SiC at room temperature, 350 °C and 600 °C from RBS, compared to SRIM 2012 simulated Se depth profile.

Table 6.1: A comparison of the first four moments of the experimental and SRIM simulated profiles. The selenium experimental profiles of RT, 350 °C and 600 °C were fitted to the Edgeworth function.

Parameter	SRIM	350 °C	600 °C
Projected ranges (Rp) (nm)	89.6	89.9 ± 2.93	90.8 ± 2.93
Straggling (ΔRp) (nm)	26.5	33.96 ± 2.93	35.27 ± 2.93
Kurtosis (β)	2.78	2.95 ± 0.1	2.9 ± 0.2
Skewness (γ)	0.13	0.05 ± 01	0.3 ± 0.05

The RBS depth profiles before and after sequential annealing at temperatures ranging from 1000 to 1500 °C in steps of 100 °C for 10 h are shown in Fig. 6.38. For both implanted samples

(350 °C and 600 °C) shown in Fig. 6.38, no change was observed in the peak position of the Se profile after annealing from 1000 up to 1200 °C. This indicates the lack of measurable shift at these temperatures. A peak shift towards the surface began after the annealing at 1300 ° C and progressed with annealing at higher annealing temperatures as can be seen in Fig. 6.39, suggesting that SiC had been removed by thermal etching. The molecules on high-energy surfaces sublimated into the vacuum, resulting in a reduction in the total energy of the system, thereby leading to roughening the sample surface [Van12]. Evidence of the thermal etching was confirmed by SEM measurements, as previously discussed.

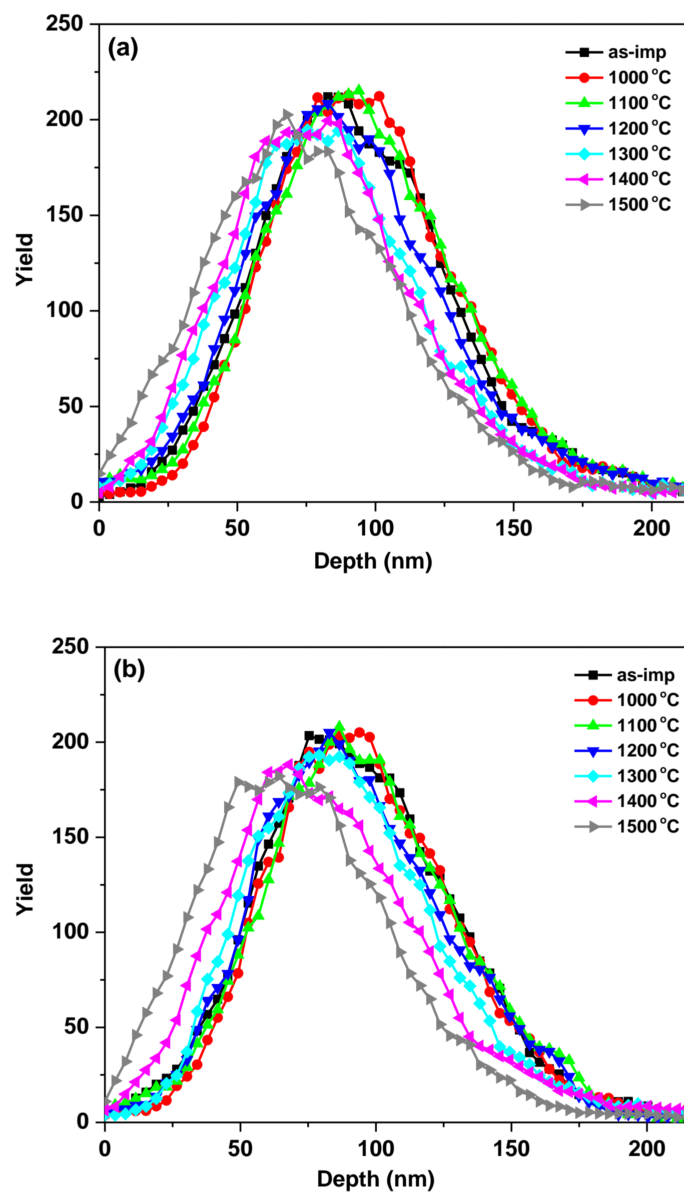

Fig. 6.38: Depth profiles of selenium implanted in SiC at (a) 350 °C and (b) 600 °C after sequential annealing from 1000 to 1500 °C for 10 h.

The retained ratio of implanted selenium during heat treatment is depicted in Fig. 6.40. A loss of some of the Se from both the implanted samples was observed after annealing at 1300 ºC (about 10 %). This behaviour is correlated with pores on the sample surface at high annealing temperature (as seen in SEM micrographs), which acts as pathways for the release of the implanted Se atoms into the vacuum upon arrival to the surface, since its boiling point (685°C) is significantly less than the annealing temperatures. It is also due to the profile shift toward the surface at these temperatures. No further loss was observed after annealing at 1400 ° C and 1500 ° C.

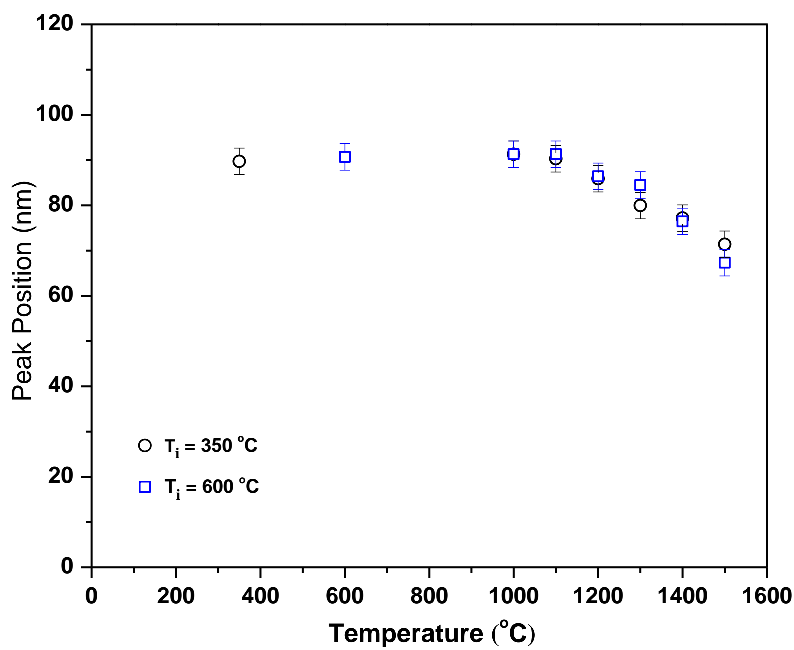

Fig. 6.39: The peak position of implanted Se profile as a function of annealing temperature.

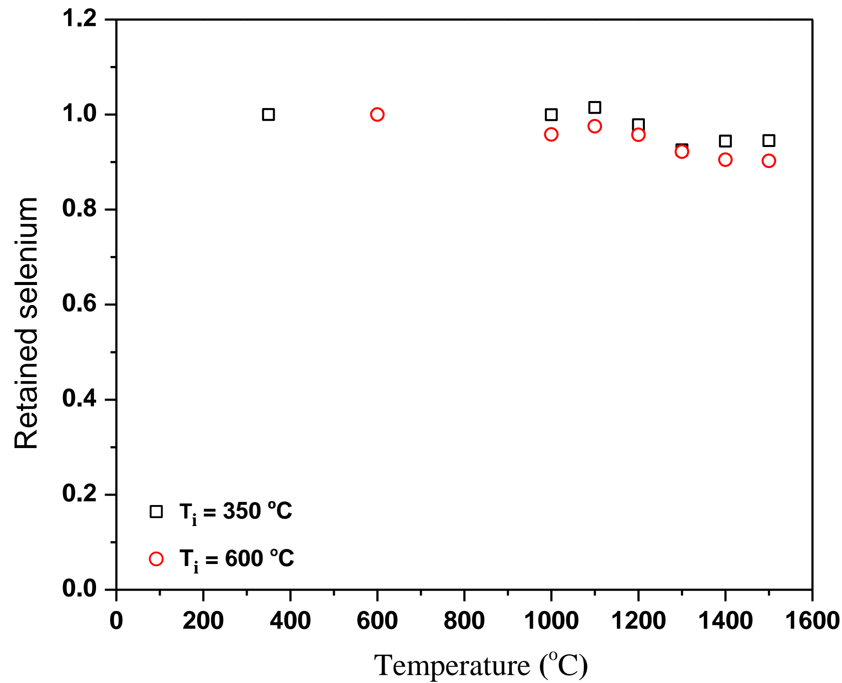

Fig. 6.40: The retained ratio of Se implanted into polycrystalline SiC profiles as a function of annealing temperature.

The broadening of the implanted Se profile in SiC was quantified by the full width at half maximum (FWHM) of the peaks. Fig. 6.41 shows the square of FWHM values as a function of annealing temperature. No broadening occurred in the samples implanted at 600 °C after heat treatment in the temperature range 1000 to 1500 °C. In the case of the 350 °C implanted sample, the broadening became noticeable after annealing at 1500 °C. However, the increase in the FWHM is within the experimental error of the RBS depth scale. There are two possible reasons for this broadening, namely the diffusion of Selenium and the effects due to the increase of surface roughness, as previously discussed in the SEM results.

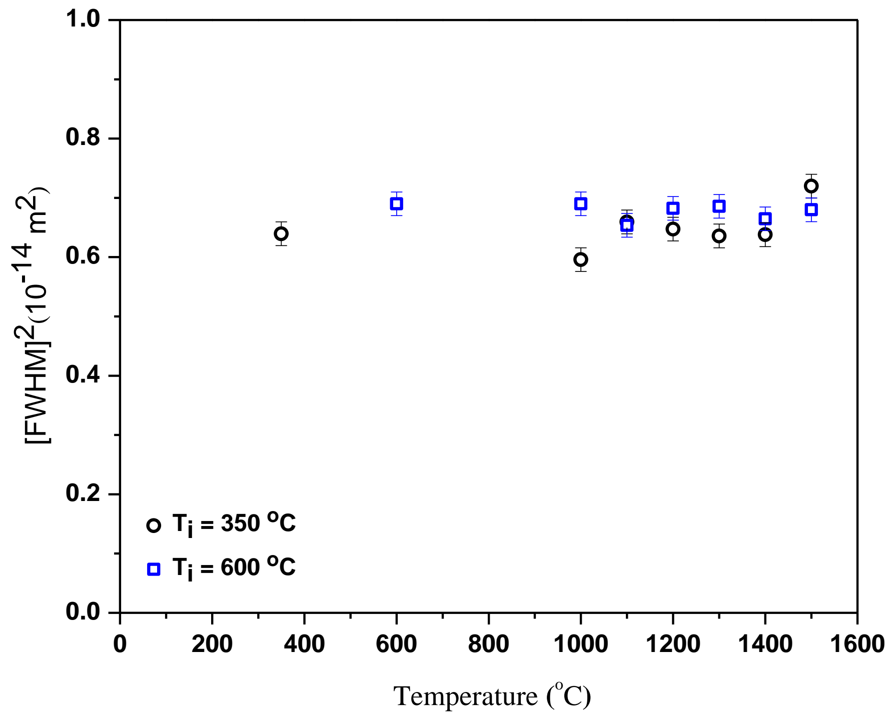

Fig. 6.41: The square of the full width at half maximum of implanted Se profiles as a function of annealing temperature.

For the isothermal study, new samples implanted at 350 °C and 600 °C were used. The implanted samples were also isothermally annealed at 1300 °C, 1350 and 1400 °C for 10 h cycles of up to 80 h. Fig. 6.42 (a) depicts the peak broadening curves of the 350 °C implanted samples. Isothermal annealing at 1350 °C and 1400 °C caused slight broadening in selenium profiles during the first and second cycle, while at 1300 °C the slight broadening occurred during the third cycle. This indicates a lack of diffusion at these temperatures. Further annealing increased the broadening at the same temperature up to 80 h. However, the broadening remained within the experimental error of the depth scale of our RBS measurements. In the case of the 600 °C implanted samples, broadening was observed only during the final cycle (80 h) - Fig. 6.42 (b). Observations and lack of diffusion in hot implants might be associated with the observed strong diffusion during implantation [Fri12]. Slight losses occurred in both implanted samples (350 °C and 600 °C) during the first annealing cycle as shown in Fig. 6.43 (a) and (b). No further loss was observed during the subsequent annealing cycles up to 80 h, as there was no significant change in the peak position of the selenium profiles.

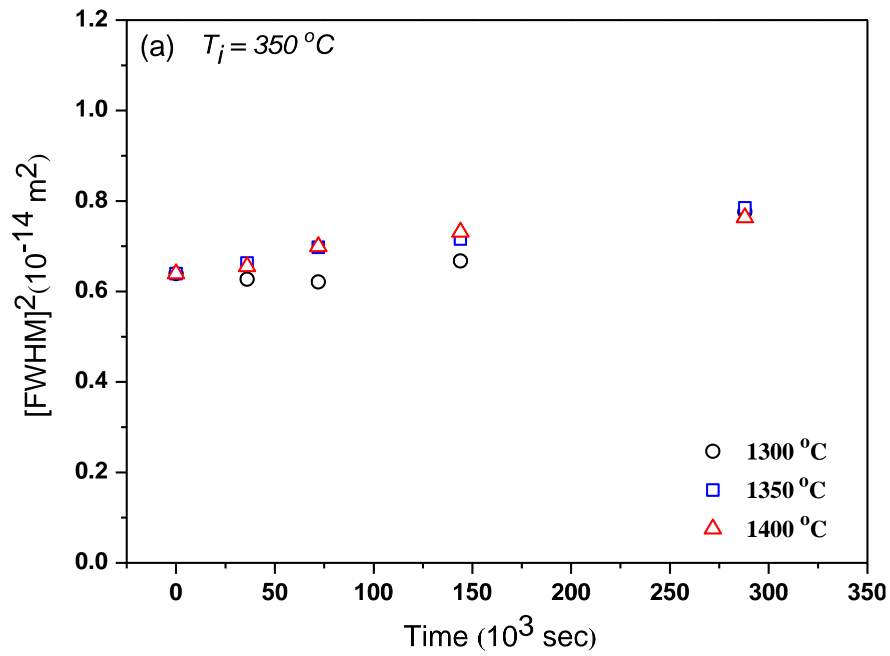

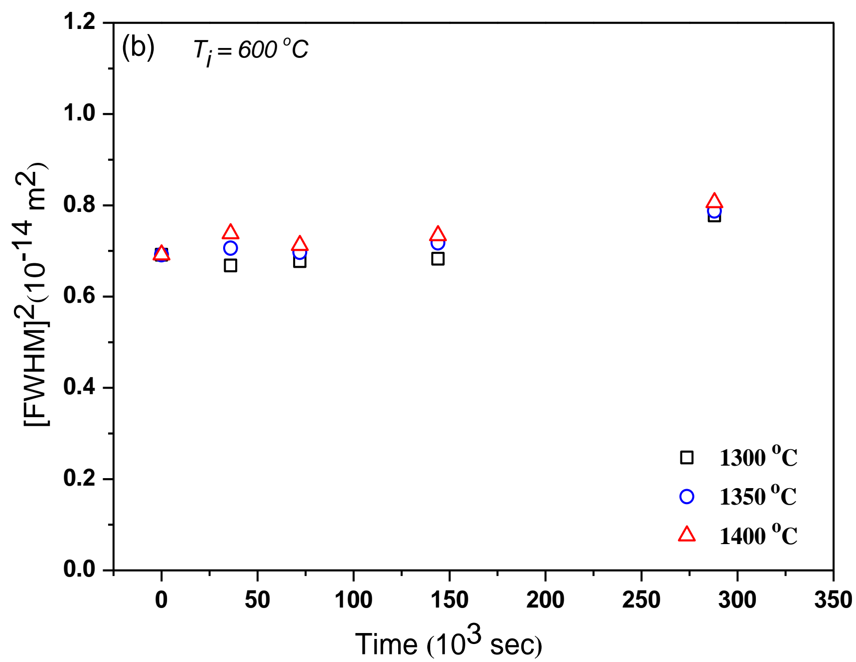

Fig. 6.42: Isothermal annealing curves of (a) 350 °C and (b) 600 °C implanted samples at 1300 °C, 1350 °C and 1400 °C.

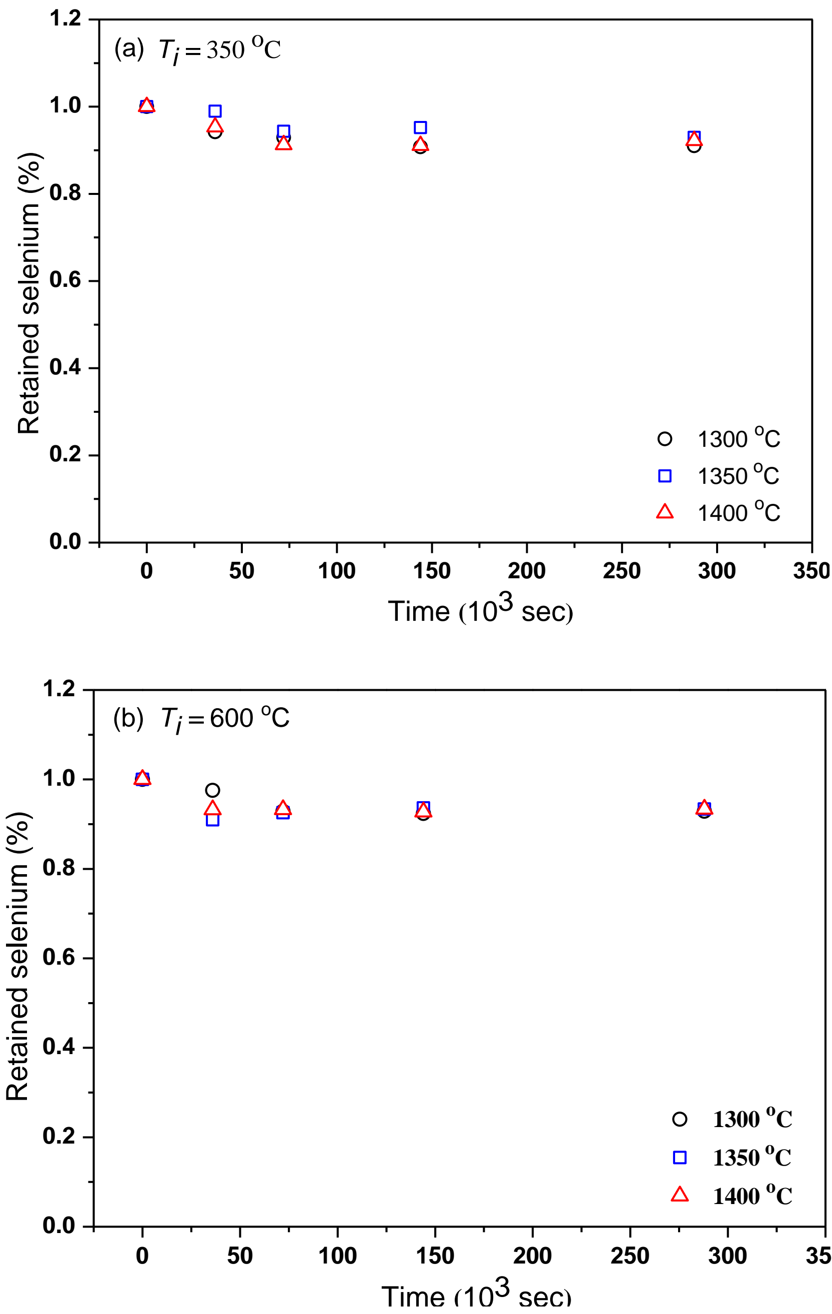

Fig. 6.43: The retained ratio of Se implanted into polycrystalline SiC at (b) 350 °C and (b) 600 °C after isothermal annealing.

Nuclear fuel particles / rods in the reactor core are removed and replaced with fresh fuel every 18 to 24 months to maintain chain reaction. The time taken by selenium to migrate through the silicon carbide thickness can be calculated by:

$$t = \frac{x^2}{D}$$

where x the thickness of SiC layer in the TRISO coated particle is$(x = 35\ \mu m)$, D is the diffusion coefficient.

For the RT implanted samples, diffusion coefficients indicate that migration of selenium through thickness of silicon carbide would take about 2.8×10^3 years, 1.9×10^3 years and 1.6×10^3 years, respectively.

In case of samples implanted at 350 °C and 600 °C, above the critical amorphization temperature, the heat treatment resulted in no measurable diffusion of implanted Se further pointing to radiation enhanced migration of Se.

The results of this study indicate the suitability of polycrystalline SiC as a diffusion barrier for selenium.

References

[Bee08] T. Beechem and S. Graham. Temperature and doping dependence of phonon lifetimes

[Cha02] W. Chang, Z. C. Feng, J. Lin, R. Liu, A. T. S. Wee, K. Tone, and J. H. Zhao."Infraredreflection investigation of ion-implanted and post implantationannealed epitaxially grown 6H-SiC," Surf.Interface Anal. 33, no. 6, (2002) 500-505.

[Des16] A. Deslandes, M. C. Guenette, L. Thomsen, M. Ionescu, I. Karatchevtseva, and G. R. and decay pathways in GaN, J. Appl. Phy. **103** (2008) 093Lumpkin, Retention and damage in 3C- b SiC irradiated with He and H ions, J. Nucl. Mater. **469** (2016) 187-193.

[Dev01] R. Devanathan, W. J. Weber, and F. Gao, Atomic scale simulation of defect production in irradiated SiC, J. Appl. Phys. **90** (2001) 2303-2309.

[Fel68] D. W. Feldman, J. H. Parker, W. J. Choyke and L. Patrick, "Phonon dispersion curvesby raman scattering in SiC, Polytypes 3 C, 4 H, 6 H, 15 R, and 21 R," Physical Review, vol. 173(3), (1968) 787.

[Fen16] X. Feng, Y. Zang. "Raman scattering properties of structural defects in SiC," In 2016 3rd International Conference on Mechatronics and Information Technology. Atlantis Press, (2016).

[Fri12] E. Friedland, N. G Van Der Berg, T. T. Hlatshwayo, R. J. Kuhudzai, J. B. Malherbe, E. Wendler and W. Wesch, Diffusion behavior of cesium in silicon carbide at T> 1000° C, Nucl. Instrum. Meth. Phy. Res. B: Beam Interactions with Materials and Atoms **286** (2012) 102-107.

[Gao02] F. Gao and W. J. Weber, Cascade overlap and amorphization in SiC: Defect accumulation, topological features, and disordering, Phys. Rev. B Condens. Matter Mater. Phys. **66** (2002) 1-10.

[Hla17] T. T. Hlatshwayo, L. D. Sebitla, E. G. Njoroge, M. Mlambo, and J. B. Malherbe, Annealing effects on the migration of ion-implanted cadmium in glassy carbon, Nucl. Instruments Methods Phys. Res. Sect. B Beam Interact. with Mater. Atoms 395 (2017) 34-38.

[Lit17] G. Litrico, N. Piluso, and F. La Via. "Detection of crystallographic defects in SiC by micro-Raman and micro-PL analysis," InMaterials Science Forum, Trans Tech Publications, Vol. 897, (2017) 303-306.

[Mal15] J. B. Malherbe, N. G. Van Der Berg, R. J. Kuhudzai, T. T. Hlatshwayo, I.Festkörperphysik, and F. Jena, Scanning Electron Microscopy of the Surfaces of IonImplanted SiC,Nucl. Inst. Methods Phys. Res. **B 354** (2015) 23-27.

[Mal17] J. B. Malherbe, P. A. Selyshchev, O. S. Odutemowo, C. C. Theron, E. G. Njoroge, D. F. Langa and T. T. Hlatshwayo, “Diffusion of a mono-energetic implanted species with a Gaussian profile, Nucl. Instruments Methods Phys. Res. Sect. B Beam Interact. With Mater. Atoms **406** (2017) 708-713.

[Mye74] S. M. Myers, S. T. Picraux, and T. S. Prevender. Study of Cu diffusion in Be using ion backscattering. Phy. Rev. **B 9** (1974) 3953.

[Nak97] S. Nakashima and H. Harima, Raman Investigation of SiC Polytypes, phys. stat. sol.,**162** (1997) 39-64.

[Pri08] L. C. Prinsloo and P. Colomban. "A Raman spectroscopic study of the Mapungubwe oblates: glass trade beads excavated at an Iron Age archaeological site in South Africa. Journal of Raman Spectroscopy: An International Journal for Original Work in all Aspects of Raman Spectroscopy, Including Higher Order Processes, and also Brillouin and Rayleigh Scattering **39** (2008) 79-90.

[Qin11] X. F. Qin, S. Li, F.X. Wang, and Y. Liang. The mean projected range and range straggling of Nd ions implanted in silicon carbide, In Key Engineering Materials **474** Trans Tech Publications Ltd, (2011) 565-569.

[San14] S. Sanchita, and S. Umapathy, Raman spectroscopy explores molecular structural signatures of hidden materials in depth: Universal Multiple Angle RamanSpectroscopy, Scientific reports 4 (2014) 5308.

[Sor06] S. Sorieul, J. M Costantini, L. Gosmain, L. Thomé, J. J. Grob, Raman spectroscopy study of heavy-ion-irradiated α-SiC, Journal of Physics: Condensed Matter **18** (2006) 5235.

[Tus19] D. Tuschel, “Stress, Strain, and Raman Spectroscopy,” Spectroscopy, vol. 34 (2019) 10-22.

[Van12] N.G. van der Berg, J.B. Malherbe, A.J. Botha and E. Friedland, Thermal etching of SiC, Appl. Surf. Sci, vol. 258 (2012) 5561-5566.

[Wen12] E. Wendler, T. Bierschenk, F Felgenträger, J. Sommerfeld, W. Wesch, D. Alber, G. Bukalis, L. C. Prinsloo, N. Van der Berg, E. Friedland and J. B. Malherbe, Damage formation and optical absorption in neutron irradiated SiC, Nucl. Inst. Methods Phys. Res. **B 286** (2012) 97-101.

[Wol03] I. De. Wolf. Raman spectroscopy: Chips and stress. Spectroscopy Europe 15 (2003) 6-13.

[Zie12] J. F. Ziegler, “SRIM 2012 computer code (2012), www.srim.org, accessed Nov. 16, 2018.

[Zon18] Xu. Zongwei, Z. He, Y. Song, X. Fu, M. Rommel, X. Luo, A. Hartmaier, J. Zhang and F. Fang, Topic review: application of Raman spectroscopy characterization in micro/nano-machining. Micromachines **9** (2018) 361.

CHAPTER 7

CONCLUSIONS AND FUTURE STUDIES

In this study the effect of selenium (Se) ions implanted into polycrystalline (SiC) was investigated. Se ions with an energy of 200 keV were implanted into SiC to a fluence of 1×10^{16} cm^{-2}. The flux was kept below 10^{13} cm^{-2} s^{-1} to minimize radiation induced heating. Implantations were performed at room temperature (RT), 350 °C and 600 °C under vacuum. Some of the RT implanted samples were sequential annealed in vacuum at temperatures ranging from 1000 to 1500 °C in steps of 100 °C for 10 h and others at temperatures of 1300 °C, 1350 °C and 1450 °C for 20 hours. Hot implanted samples (350 °C and 600 °C) were only sequential annealed in vacuum at temperatures ranging from 1000 ºC to 1500 °C in steps of 100 °C for 10 h. Other sets of cold (RT) and hot implanted samples were subjected to isothermal annealing at 1300 ºC,1350 ºC, and1400 ºC for 10 h cycle up to 80 h.

The migration of implanted Se was monitored by Rutherford backscattering spectrometry (RBS) while structural and morphological changes were monitored by Raman spectroscopy and scanning electron microscopy (SEM).

7.1 Room temperature implantation

Raman results showed that implantation at RT led to an amorphization of the near-surface of the SiC layer. Recrystallization already occurred after annealing at 1000 ºC. The RBS depth profile obtained from the RT as-implanted samples showed that the majority of implanted Se was embedded in the bombardment-induced amorphous layer. Broadening of the implanted Se profile began after annealing at 1300 °C during sequential annealing. This broadening became more significant after annealing at 1400 °C and 1500 °C indicating the diffusion of implanted Se. However, the broadening at these temperatures were within the experimental error of the depth scale of our RBS measurements. Thermal etching occurred after annealing at 1300 °C resulting in a shift of the Se profiles towards the surface accompanied by a loss of about 10 % of Se. This loss became more significant with increasing thermal etching. The molecules on high-energy surfaces sublimated into the vacuum, resulting in a reduction in the total energy of the system, the annealing at 1500 °C caused the decomposition of silicon carbide for the

sample implanted at room temperature. This was clearly shown by the formation of the carbon layer at the top of the carbon surface.

Sequential annealing the RT implanted samples at 1300 °C, 1350 °C and 1450 °C for 20 hours resulted in broadening of the Se profile accompanied by shift towards surface and loss. Diffusion coefficients of 6.3×10^{-21} and 2.0×10^{-20} m^2s^{-1} were determined at 1300 ºC and 1350 °C respectively. The diffusion coefficient at 1450 °C could not be determined due to segregation towards the surface.

The SEM images showed that the polishing marks became less pronounced after ion bombardment compared to those of the pristine. This is due to the sputtering of the SiC surface by the bombarding Se ions, and the swelling of the amorphous implanted layer. The SEM image at higher magnification after annealing at 1000 °C showed evidence of recrystallization. The crystallites became larger and more visible as the annealing temperature increased. The higher magnification also showed that some large crystals are on top of the smaller crystals, with the latter forming a kind of a substrate. Annealing at 1400 °C resulted in large pores appearing on the sample surface. The distribution in crystal size became uniform with more prominent pores after annealing at 1500 °C. Loss of significant amounts of the implanted selenium ions at these temperatures may be attributed to the presence of these pores.

The results of SEM analysis showed that annealing of an as-implanted sample at 1300 ºC for 20 hours resulted in large crystals with few pores. Moreover, the 1450 ºC samples had slightly more and longer dendritic crystals.

Isothermal annealing at 1300 ºC, 1350 ºC, and 1400 ºC for 10 h cycle up to 80 h caused broadening of selenium profiles after the first and second annealing cycles and no further a broadening was observed after subsequent annealing cycles up to 80 h. These indicate that selenium transport in the SiC damaged region is governed by the number of defects. The first annealing cycle resulted in a loss of approximately 10 % in the sample annealed at 1300 °C, whereas the loss in both samples annealed at 1350 °C and 1400 °C are similar, about 15 %. Moreover, losses increased in the subsequent heat treatment cycles in all samples. This may be attributed to the profile shift towards the surface due to thermal etching during this cycle, causing the Se atoms to escape into the vacuum upon arrival to the surface.

Diffusion coefficients obtained by comparing profiles of selenium depth profiles before and after annealing were 1.4×10^{-20} m^2s^{-1}, 2×10^{-20} m^2s^{-1} and 2.5×10^{-20} m^2s^{-1} at 1300 ºC, 1350 ºC

and 1400 °C, respectively with an activation energy of 2×10^{-22} J and a pre-exponential factor of 1.7×10^{-16} m^2s^{-1}.

7.2 Hot implantation

The samples implanted at 350 °C and 600 °C, above the critical amorphization temperature and under the same bombardment conditions as RT implant, retained their crystallinity with some radiation damage. The damage was found to be greater at 350 °C compared to 600 °C. Moreover, Raman results showed that implantation at 350 ºC and 600 ºC caused a modification in the mechanical properties of the samples with a residual tensile stress of 0.86 GPa and 0.95 GPa, respectively. This was due to the increase of the chemical bond lengths, relative to their lengths in the unstressed crystals. The residual pressure decreased with the annealing temperature, but did not play a role in the migration of the implanted Se. The RBS results showed that there was no broadening of the Se profile in the samples implanted at these temperatures during annealing up to 1500 °C. This indicates a lack of diffusion, even at high annealing temperatures. In both samples, no changes were occurred in the peak position of the Se profile after annealing from 1000 up to 1200 °C. The peak shift towards was observed after annealing at 1300 °C and increased with annealing temperature indicating thermal etching.

Diffusion coefficients estimated from the RT implanted samples indicated that migration of selenium through thickness of silicon carbide in the TRISO particle would take about 2.8×10^3 years, 1.9×10^3 years and 1.6×10^3 years, respectively.

In comparison, heat treatment of samples implanted at 350 °C and 600 °C, above the critical amorphization temperature resulted in no measurable diffusion of implanted Se further pointing to radiation enhanced migration of Se.

These results indicate that selenium does not migrate via the diffusion mechanism investigated in this study. Therefore, polycrystalline silicon carbide is suitable as the main diffusion barrier in TRISO coated particles.

7.3 Future studies

To get more insight in the migration behaviour of Se implanted into SiC, the effect of ion implantation and heat treatment on the surface roughness of the silicon carbide substrate need to be understood. Hence, atomic force microscopy (AFM) will be used to measure the roughness in the as implanted and annealed samples to validate the obtained diffusion results. Similar migration study will be conducted at an atomic scale using transmission electron microscopy (TEM). Since in nuclear reactors, SiC will be will be subjected to different irradiations in the presence of helium (He), the effects of swift heavy ions irradiation and He bubbles in the migration behaviour of Se will be undertaken. TEM analysis will allow the study of the migration of Se at an atomic scale.

CHAPTER 8

APPENDIX

The research project presented in this thesis has contributed to several publications and conference presentations. Below is a summary of these research contributions:

8.1 Publications in peer-reviewed/refereed journals

1. **Z. A. Y. Abdalla**, T. T. Hlatshwayo, E. G. Njoroge, M. Mlambo, E. Wendler, J. B. Malherbe, Migration behaviour of selenium implanted into polycrystalline SiC, SAIP proceedings 2018. *ISBN: 978-0-620-85406-1.*

2. **Z. A. Y. Abdalla**, M. Y. A. Ismail, E. G. Njoroge, T. T. Hlatshwayo, E. Wendler, J. B. Malherbe, Migration behaviour of selenium implanted into polycrystalline SiC, *Vacuum* **175** (2020) 109235.

3. **Z. A. Y. Abdalla**, M. Y. A. Ismail, E. G. Njoroge, T. T. Hlatshwayo, E. Wendler, J. B. Malherbe, Effect of heat treatment on the migration behaviour of selenium implanted into polycrystalline SiC, Nucl. Inst. Methods Phys. Res. **B 487** (2021) 30-37.

8.2 Conference Presentations

8.2.1 National Conferences

1. The 63rd Annual Conference of the South African Institute of Physics (SAIP 2018). Department of Physics, University of Free State from 25-29 June 2018, Bloemfontein, South Africa. (Poster presentation)

8.2.2 International Conferences

1. The 24th International Conference on Ion-Surface Interactions (ISI-2019), August 2019, Moscow, Russia. (Poster presentation), where the presentation was awarded 'Best PhD poster presentation.

2. 21st International Conference on Surface Modification of Materials by Ion Beams (SMMIB-2019) August 2019, Tomsk, Russia. (Poster presentation)

3. 24th international conference on Ion Beam Analysis (IBA-2019), October 2019 in Antibes, France. (Poster presentation)